Pattern Recognition in the Inner Tracking System of HERA-B and Measurement of the V_0 Production Cross Section in pN Collisions

DISSERTATION

zur

Erlangung des Grades eines Doktors

der Naturwissenschaften

vorgelegt von

Dipl.-Phys. Iouri Gorbounov

geb. am 28.01.1976 in Protvino

eingereicht beim Fachbereich Physik

der Universität Siegen

Siegen 2003

Dissertation

1. Gutachter: Prof. Dr. Günter Zech
2. Gutachter: Prof. Dr. Peter Buchholz

Disputation
am 23.01.2004

Prüfer: Prof. Dr. Hans-Dieter Dahmen
Prof. Dr. Peter Buchholz
Prof. Dr. Günter Zech

urn:nbn:de:hbz:467-353

Dissertation
submitted to the
Siegen University
for the degree of
Doctor of Natural Sciences

Pattern Recognition in the Inner Tracking System of HERA-B and Measurement of the V_0 Production Cross Section in pN Collisions

presented by
Diplom-Physicist Iouri Gorbounov
Born in Protvino

Siegen, 2003

Zusammenfassung

Das HERA-B-Experiment befindet sich am HERA-Beschleuniger bei DESY, Ziel dieses Experimentes war die Messung der CP-Verletzung in dem System der neutralen B-Mesonen. Das inneren Spurkammersystem von HERA-B besteht aus GEM-MSGC-Detektoren.
Im ersten Teil der Arbeit wird die Entwicklung eines Spurrekonstruktions- Algorithmus (CATS) für das inneren Spurkammersystem vorgestellt. Der Algorithmus wurde erfolgreich während der Online-Datennahme und für die Offline-Aufbereitung der Daten der Jahre 2002/03 benutzt.
Die Betriebseigenschaften des inneren Spurkammersystems während der Inbetriebnahme wurden bestimmt. Die angewendete Methode basiert auf dem für das innere Spurkammersystem entwickelten Spurrekonstruktions-Algorithmus. Mit Hilfe der gemessenen Effizienzen der Einzeldetektoren wurden die individuellen GEM-Spannungen korrigiert, um die Gesamteffizienz des inneren Spurkammersystems zu verbessern.
Im zweiten Teil der Arbeit wird eine Messung des inklusiven Produktions-Wirkungsquerschnitts $\mathrm{d}\sigma_{pA}/\mathrm{d}x_F$ und $\mathrm{d}\sigma_{pA}/\mathrm{d}p_t^2$ für K_S^0, Λ und $\bar{\Lambda}$ Teilchenproduktion in pN-Kollisionen bei $\sqrt{s}$=41.6 GeV vorgestellt. Daten aus Proton-Kohlenstoff, Titan und Wolfram Wechselwirkungen wurden benutzt. Die Massenabhängikeit des Wirkungsquerschnitts σ_{pA} wurde gemessen.

Abstract

The HERA-B experiment located at the HERA collider at DESY, was designed and built to measure CP violation in the system of neutral B mesons. One of the HERA-B detector components is the Inner Tracker, which consists of Micro-Strip Gas Counters with a Gas-Electron Multiplier (GEM-MSGC).
This thesis describes the development of a pattern recognition algorithm (CATS) for the Inner Tracking system of HERA-B. The algorithm was successfully used during online data taking and offline reprocessing of the collected data in the years 2002 and 2003.
During the running period 2002/03 the performance of the Inner Tracking system was estimated. The applied procedure was based on the developed pattern recognition algorithm. With the help of the measured efficiencies, a tuning of the GEM voltages was performed in order to increase the efficiency of the Inner Tracking system.
The second part of this thesis describes a measurement of the inclusive differential cross sections $\mathrm{d}\sigma_{pA}/\mathrm{d}x_F$ and $\mathrm{d}\sigma_{pA}/\mathrm{d}p_t^2$ for the production of K_S^0, Λ and $\bar{\Lambda}$ particles produced in pN collisions at $\sqrt{s}$=41.6 GeV. As target materials C, Ti and W were used and the dependence of the total cross section σ_{pA} on the target atomic mass is measured.

Contents

Chapter 1

Introduction

This chapter presents a brief overview of the original physics goal of HERA-B - measuring CP violation in the decays of neutral B mesons. Finally the modified physics program is outlined.

The violation of CP symmetry was first observed in the system of neutral K mesons ($K^0 - \bar{K}^0$). The K_L^0 has a CP eigenstate of -1 but it was shown that it can also decay into two charged pions with a CP eigenstate of +1. The Standard Model offers a mechanism which can explain this violation. The system of neutral B mesons should also show CP violation mediated by the same mechanism and in addition the CP violation in the B-system should be large relative to the Kaon system.

HERA-B was approved in 1994 [1] but the start of the HERA-B experiment was delayed by several years due to problems during detector development and commissioning. The e^+e^- B factory approach was chosen by two experiments: BaBar [29] collaboration at SLAC and Belle [30] collaboration at KEK, they were able to present their first measurements of CP violation already in 2000. Since that moment the measurements have reached an accuracy level that can not be reached by HERA-B. HERA-B was commissioned in 1999 with a short data taking run. In 2000/01, during the HERA luminosity upgrade, HERA-B detector was partially upgraded and finalized. Since it became obvious that HERA-B is no longer competitive in B-physics a new physical program was proposed for the data taking in 2002/2003.

1.0.1 CP violation

CP is a symmetry that relates particles and antiparticles. If CP would be an exact symmetry than it would be hard to explain why our universe consist almost exclusively of matter and hardly any antimatter can be found.

Charge conjugation (C, particles are replaced by their antiparticles) and Parity (P, Space Inversion) are discrete operators. They are conserved symmetries in strong interactions but they are maximally violated in weak interactions. However, it was thought for some time that the combination of the two is conserved in weak interactions. But in 1964 a small CP violation was observed in the Kaon system.

The Standard Model offers the following explanation: the eigenstates of the weak interaction of quarks do not coincide with the mass eigenstates, the transition between the two bases is described by the Cabbibo-Kobayashi-Maskawa (CKM) matrix V_{CKM}:

$$\mathbf{V_{CKM}} = \begin{pmatrix} V_{ud} & V_{us} & V_{ub} \\ V_{cd} & V_{cs} & V_{cb} \\ V_{td} & V_{ts} & V_{tb} \end{pmatrix}$$

This matrix is unitary, so its parameters are bound by unitarity relations. Four parameters of the matrix remain free. In the Wolfenstein [31] parametrisation, the parameters are expanded in powers of the Cabbibo angle θ_C.

$$\mathbf{V_{CKM}} = \begin{pmatrix} 1-\frac{1}{2}\lambda^2 & \lambda & A\lambda^3(\rho - i\eta + \frac{i}{2}\eta\lambda^2) \\ -\lambda & 1-\frac{1}{2}\lambda^2 - i\eta A^2\lambda^4 & A\lambda^2(1+i\eta\lambda^2) \\ A\lambda^3(1-\rho-i\eta) & -A\lambda^2 & 1 \end{pmatrix}$$

where is $\lambda = \sin\theta_C$. One of these parameters is complex (η) and it is the one that is responsible for CP violation. The unitarity constraints can be displayed as triangles in the complex plane where the sides are products of the CKM matrix parameters. One of such triangles is shown below:

$$V_{ud} * V_{td}^* + V_{us} * V_{ts}^* + V_{ub} * V_{tb}^* = 0$$

, with angles α, β, γ. The area of the triangle indicates the strength of the *CP* violation.

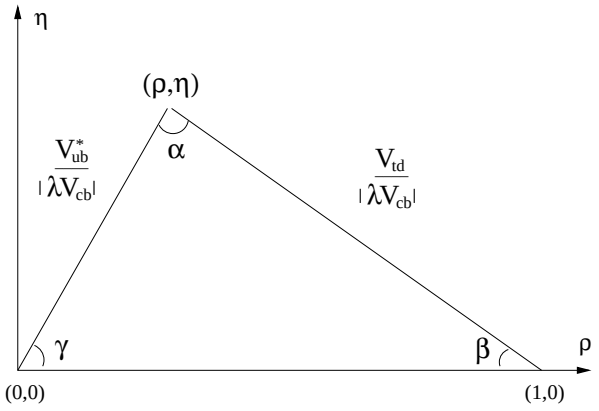

Figure 1.1: CKM unitarity triangle.

In order to measure *CP* violation in the B system, B^0 or $\bar{B}^0$ mesons have to be produced, their flavour tagged, and their decays reconstructed. The design of HERA-B was optimized for the measurement of the "Golden Decay":

$$B^0 or \bar{B}^0 \rightarrow J/\psi K_S^0$$

which through the asymmetry in the rates of the decays of B^0 and $\bar{B}^0$ mesons to the same final state will give $\sin 2\beta$, one of the angles of the unitarity triangle, with very little theoretical uncertainties:

$$sin2\beta \approx \frac{N_{\bar{B}^0} - N_{B^0}}{N_{\bar{B}^0} + N_{B^0}}$$

Other decays such as:

$$B^0 or \bar{B}^0 \rightarrow \pi^+\pi^-$$

$$B^0 or \bar{B}^0 \rightarrow \rho^0 K_S^0$$

provide access to the angles α and γ. However, these decays are theoretically not as clean as the "Golden Decay". Due to contributing "penguin" amplitudes which are not easy to calculate, this affects the correspondence between the asymmetries and the angles of the unitarity triangle.

1.0.2 Physics Programme for Data Taking 2002/03

The proposed physics program for the run 2002/03 concentrates on the physics feasible with the existing detector (The HERA-B detector is optimized for the detection of lepton pairs with high transverse momentum). The physics program includes the measurements of nuclear effects in charmonium production and the determination of the $b\bar{b}$ production cross section in proton-nucleon collisions by using the existing dilepton trigger. In addition by collecting Minimum Bias events , HERA-B offers the unique possibility to contribute to QCD physics. One of the topics is the production cross section of strange particles [18, 19].

The main interest in the measurement of strange particle production cross section in nuclei is driven by heavy ion physics. In heavy ion collisions carried out at RHIC[1] at BNL[2] or SPS[3] at CERN[4] a strangeness enhancement is one of the major interests. It is believed that a strangeness enhancement could be a signature for the phase transition from quark-gluon plasma to normal nuclear matter.

1.0.3 The Search for QGP

At sufficiently high temperature and density, the colour force between quarks becomes so small that they can behave as essentially non-interacting free particles. Therefore, if the conditions are extreme enough, the quarks should lose their confinement and a phase transition to a "new" form of matter should occur. This "new" form of matter is known as the Quark-Gluon Plasma (QGP) [20]. It is widely believed that with the help of heavy-ion colliders, it is possible to achieve this deconfined state. If so, a QGP system in a short time cools-down and re-hadronizes. The different stages are shown in Fig. 1.2.

The process is started when heavy-ion beams collide and a fireball is created. During an initial stage, many quarks and gluons are created in the collision volume in inelastic collisions. At the pre-equilibrium stage, these "secondary" partons interact with themselves. With the increase of parton density, $q\bar{q}$ pairs are created more easily due to the high temperature (Debye–screening process). When this partonic matter reaches equilibrium, it is called Quark-Gluon Plasma. At some point the fireball expands due to the internal pressure. It cools down and the system crosses the phase boundary, partons start to hadronize. At the end, the system expands until it is cool enough so that elastic collisions between particles can no longer occur and the particles' momenta are fixed.

As the deconfined phase is very short lived, it is impossible to detect it directly. Therefore, in order to conclude whether the phase transition occurred, the measurement of a quantity which is specific for the QGP phase is required.

[1]Relativistic Heavy Ion Collider
[2]Brookhaven National Laboratory
[3]Super Proton Synchrotron
[4]European Organization for Nuclear Research, Geneva

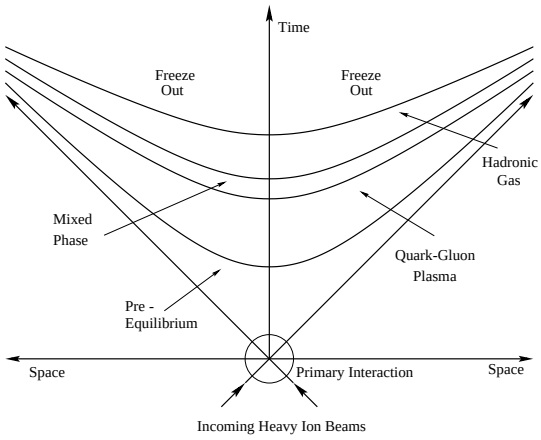

Figure 1.2: The space-time evolution of a heavy-ion collision, which undergoes a phase transition to a QGP [21].

The use of global observables, such as energy density as a function of temperature has a problem. A calculation of the energy density is model dependent and if the phase transition is continuous more than first order, the energy density will increase linearly with increasing temperature in the transition area. In order to avoid such a problem, other observables are used to search for a deconfined state of matter. It is predicted, that the phase transition can be seen experimentally in the following effects:

- Hard thermal dilepton/photon emission. Direct photons carry information about the thermodynamics of the QGP phase because their momentum distributions are determined by the temperature of the quarks, antiquarks and gluons in the plasma and because they are not affected by the hadronization. The momentum distributions of those photons should show an excess at higher transverse momenta, because the QGP should be formed at temperatures higher than those in the hadronic phase. Dileptons (lepton pairs: e^+, e^- and μ^+, μ^-) also carry information about the thermodynamic properties of the fireball.

- Charmonium suppression. In a QGP phase, the $c\bar{c}$ pairs may become unbound due to the process of Debye–screening, which leads to a suppression in the measured yield of J/ψ. The process of Debye–screening occurs at high hadronic densities. A quark can interact with quarks of other hadrons, then the quark is not connected to a hadron and can propagate freely through a volume of deconfined quark and gluon matter.

- Strangeness enhancement. The production of strange and anti-strange quarks was proposed by Rafelski in 1982, as a probe to study the QGP phase transition. There are more available production channels for $s\bar{s}$ pairs in the QGP, due to the high gluon density and gluon fusion and annihilation of light $q\bar{q}$ pairs, then in ordinary pp interaction. The gluonic channels contribute more than 80% to the total production rate for strange quarks.

1.0.4 Strangeness production in a Quark Gluon Plasma

The threshold energy required to produce a pair of $s\bar{s}$ quarks is just the mass of two strange quarks. Due to the high temperature involved in the QGP phase, the thermal production of $s\bar{s}$ pairs becomes possible. Another source of enhancement of $s\bar{s}$ pairs comes from the process of Pauli blocking of the light quarks. As all quarks are fermions, they obey the Pauli Exclusion Principle. Therefore, as more and more light quarks are produced in the collision, they fill up the available low energy levels and it becomes favourable to create $s\bar{s}$ pairs. The production of anti-strange and multi-strange baryons will be enhanced as well.

Even if an enhancement of strangeness occurs in the QGP, there are some difficulties in quantifying the magnitude of this enhancement. The lifetime of the QGP phase is unknown, it is impossible to compute the actual values of particle production. An enhancement is expected to occur in A+A collisions compared to scaled p+p collisions (secondary collisions). Therefore, the unanswered theoretical question is what is the normal enhancement expected in A+A collisions. This can only be extracted from experimental results.

In order to summarize, before one can apply strangeness enhancement as a probe in nuclear collisions, it is important to fulfill a sequence of steps:

- study the elementary production process in p-p to determine its behaviour in the absence of any nuclear effects,
- determine its behaviour in the confined nuclear matter,
- check if in A-B collisions there are deviations from the "normal" behaviour observed in the confined nuclear matter.

Therefore pA experiments are a very important intermediate step, which can help to understand the behaviour of strange matter before to make any conclusions about the signature of QGP.

Chapter 2

The HERA-B experiment

2.1 The HERA Storage ring

HERA-B is one of the four high energy experiments which are located at the HERA[1] collider at DESY[2] in the North-West of Hamburg. It accelerates positrons or electrons to 27.5 GeV and protons to 920 GeV and has a circumference of 6.3 km.

The two beams are colliding at two interactions zones (Hall North and Hall South), where the experiments H1 and Zeus are placed (see Fig. 2.1). The physical programs of these experiments include: measuring of the proton structure, studies of the hadronic final state including jet physics, diffractive scattering in deep inelastic scattering and photo production of jets.

In the east hall of HERA a fixed target experiment HERMES is situated. The experiment uses longitudinally polarized positrons and has an internal polarized gas target. HERMES investigates the spin structure of the nucleon.

The fourth experiment is HERA-B and it is located in the experimental hall West. HERA-B uses only the proton beam, by introducing thin target wires in the halo of the proton beam interactions of the protons with the target wires are produced. This setup allows an operation at high interaction rates without disturbing the operation of the other experiments. The physical program of the HERA-B experiment is described in chapter 1.

2.2 Detector overview

Fig. 2.5 shows a schematic view of the HERA-B experiment. The experiment has the typical setup of a forward magnet spectrometer with a fixed multi-wire target [28]. It consists of a Vertex Detector followed by a warm dipole magnet, series of tracking stations in front, inside and behind the magnet. Particle identification is provided by a Ring Imaging Čerenkov Counter (RICH), Electromagnetic Calorimeter (ECAL) and Muon Detector System. These sub-systems are briefly described below.

The HERA-B coordinate system originates at the target system with the z axis directed along the proton beam, the y axis pointing upward and the x axis pointing to the center of the HERA ring.

[1] Hadron-Elektron-Ring-Anlage

[2] Deutsches Elektronen-Synchrotron

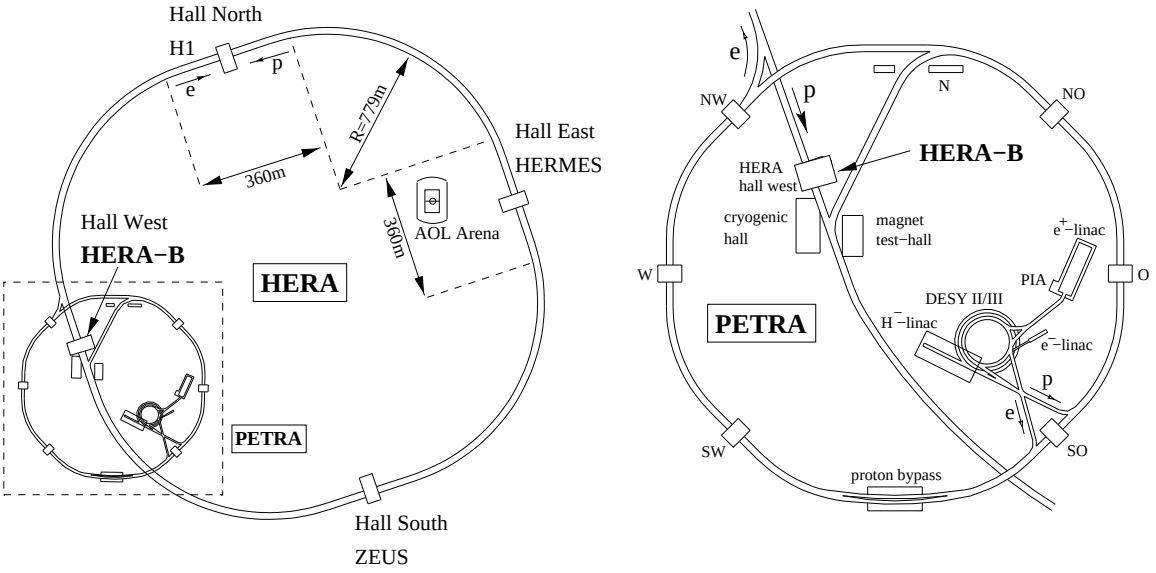

Figure 2.1: The layout of the accelerators and experiments situated at DESY in Hamburg. Left: Overview over the complete facility. Right:The pre-accelerators DESY-II and PETRA and the Hall West where the HERA-B is placed.

Target. The target consists of two stations with four wires each [2]. They can be steered individually which allow to select specific wire configurations. Wires inserted into the proton beam halo follow movements of the beam, keeping the interaction rate approximately constant.

The interaction rate is measured by a set of scintillator hodoscopes placed at the exit window of the RICH vessel. In case of a multi-wire configuration the individual contribution of each wire to the overall rate can be measured with the help of charge integrators.

During running in 2000, the first target station was equipped with titanium wires and the second station contained wires made out of aluminium, carbon and tungsten. During data taking in 2002 - 2003 aluminium, carbon, tungsten and titanium wires were used with slightly different setup. The use of different wires allows to measure nuclear effects in particle production. These measurements can be performed using two wires at the same time, reducing possible impact of the detector or beam changes with time on the systematic error.

The target mechanics and the Vertex Detector System are build into one vacuum vessel which is a part of the primary vacuum of the proton beam (Roman Pot system).

The original reason for the target setup of 8 wires subdivided to 2 stations was chosen to achieve efficient primary vertex reconstruction at an operation rate of about 40 MHz leading to multiple interactions in one bunch crossing.

Vertex Detector System. The Vertex Detector System [3] has eight superlayers build of 64 double-sided silicon micro-strip counters. The first eight superlayers of the VDS are placed inside the vacuum vessel. In order to retract the counters during the beam injection the system of manipulators and Roman pots to reduce multiple scattering

is foreseen. In the operation phase (the beam reached stable conditions) the counters are moved into their nominal positions, about 10 mm away from the beam core.

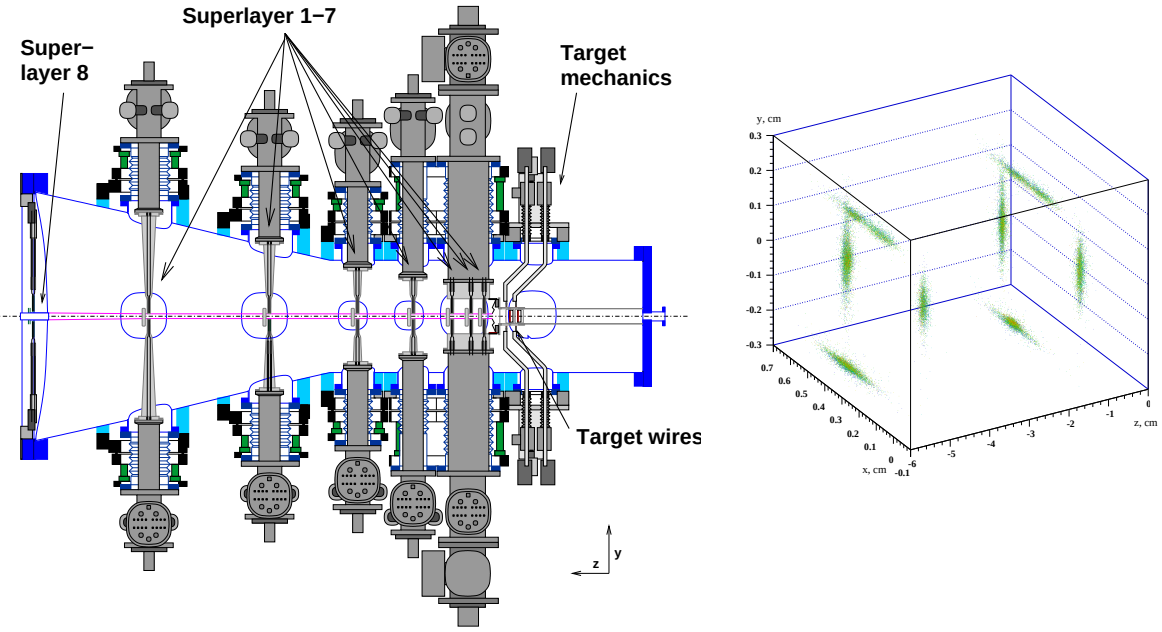

Figure 2.2: *Left:* Schematic view of vertex detector vessel. The target mechanics are seen. *Right:* Positions of reconstructed primary vertices during a multi-wire run.

The detector has a readout pitch of 50 μm and can measure tracks with polar angles from 10 till 250 mrad. The track information provided by the VDS is used to reconstruct primary and secondary vertices from direct decays like $J/\psi \to \mu^+\mu^-$ or $K^0_s \to \pi^+\pi^-$. A resolution for secondary vertices of about 70 μm in the x plane perpendicular to the beam direction and 500 - 700 μm along the beam direction were obtained with real data.

Spectrometer Magnet. A warm dipole magnet, with a magnetic field integral of 2.2 Tm is used for momentum analysis. The magnetic field is orientated along the y axis.

The deflection of the proton beam by the spectrometer magnet is compensated by three additional magnets placed upstream of the experiment. The electron beam passes through the spectrometer magnet as well, it is protected by a specifically shaped pole face of the spectrometer magnet and by a set of cylinders around the electron beam pipe.

Main Tracking System. The stations of the tracking system are situated along the beam pipe. In order to be able to achieve the required spatial resolution and to cope with the partical fluxes, the system is divided into two parts: the Inner and Outer Tracker. The Inner Tracker (ITR) uses the GEM-MSGC technology and has to withstand a high particle flux of up to $10^7 s^{-1} cm^{-2}$. It covers the region from 5 to 30 cm from the beam-pipe and provides a spatial resolution of about 100 μm. The ITR is described in detail in Chapter 3.

The Outer Tracker (OTR) [4] covers an area starting at 20 cm to 300 cm around the beam-pipe with a small overlap to the ITR. It is built of honeycomb drift chambers with a cell size of 5mm in the inner region and 10mm in the outer region. In both tracking

systems, chambers are arranged into layers covering a full plane in the xy plane and several layers are grouped into one superlayer. The layers of one superlayer are arranged in three different wire orientations of: $0^0, +5^0, -5^0$ with respect to y axis. The stereo chambers are needed in order to resolve the y coordinate. The hit resolution of the OTR is about 350 μm.

Ring Imaging Čerenkov Counter. The Ring Imaging Čerenkov Counter [5] is used to distinguish between different particle types. The detection is based on the principle that charged particles passing with a speed exceeding that of light through a medium emit photons.

The HERA-B RICH is filled with perfluoro-butane (C_4F_{10}) at ambient pressure. To register emitted Čerenkov light an array of photomultiplier tubes is used. With such a kind of gas the Čerenkov momentum threshold is 2.6 GeV for pions, 9.0 GeV for kaons and 17.2 GeV for protons.

The Čerenkov light emitted by one particle forms a ring at the plane of photomultipliers.

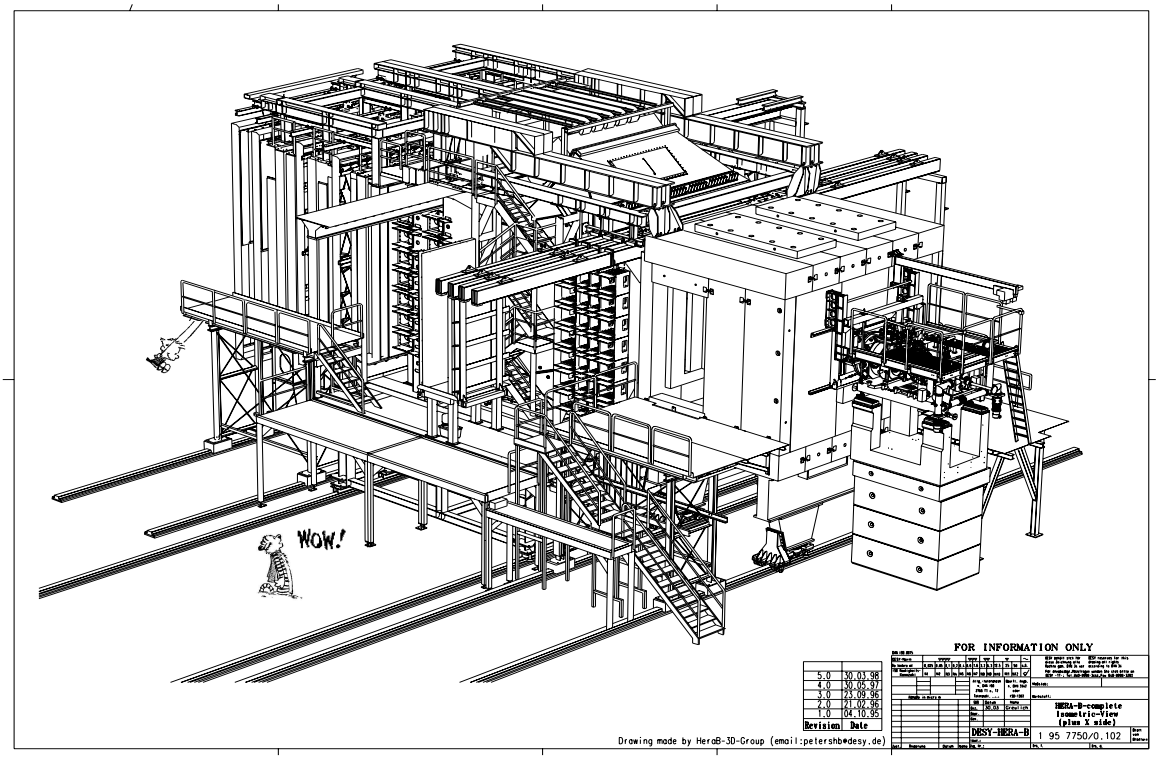

Figure 2.3: Three-dimensional view of the HERA-B detector.

If a ring is found and matched with a track, the particle identification program can assign a likelihood to each particle type according to the track momentum and the ring radius.

Electromagnetic Calorimeter. The Electromagnetic Calorimeter (ECAL) [6] is a sampling calorimeter of "shashlik" type: each cell consists of a combination of scintilliator plastic planes and absorbers. Wave-length shifting fibers are inserted in the absorbing

and scintillating material. The light output of the optical fibres is collected by photomultipliers. The ECAL is subdivided into inner, middle and outer parts with cell sizes of 2.23x2.23 cm^2, 5.58x5.58 cm^2 and 11.15x11.5 cm^2 respectively. In the inner part of the ECAL a tungsten alloy as absorber is used while outer and middle parts use lead. The radiation length of the calorimeter is about 20 - 22 radiation length X_0.

The calorimeter is designed to measure the energy of the electrons and photons and to distinguish them from hadrons. In addition the ECAL is used in the trigger scheme to provide a pretrigger.

Muon system. [7] To identify muons, a system of tracking chambers is placed behind the ECAL. In order to suppress background from hadrons, steel and concrete absorbers are placed in front of these stations. In total the absorber has a thickness of about 20 interaction lengths. The inner part of the Muon system is made of Gas Pixel Chambers with a cell size of 9x9 mm^2. They cover an area from 14 cm to 40 cm around the beampipe.

The first two stations of the Muon System in the outer part consist of proportional wire chambers arranged in three stereo views ($0^0, +20^0, -20^0$). The last two stations are build of tube chambers with an additional pad readout. The readout pads have a size of 12x10 cm^2. Pad signal coincidences, in the last two superlayers, found by the pretrigger are used by the trigger system as track seeds.

High-pt and TRD. In addition to the described detectors two more sub-detectors are installed: The high-pt pretrigger system and a transition radiation detector. The high-pt detector was in parts routinely operated during the data taking in 2002/03 but the obtained data has not been used in the reconstruction chain. The transition radiation detector is only partly installed and did not deliver any data.

2.3 Trigger

The experiment was foreseen to collect B-decays in the channel $B \to J/\psi K^0_S$ ($J/\psi \to l^+l^-$ and $K^0_S \to \pi^+\pi^-$) which are just a tiny fraction of the overall number of events. The cross section for $b\bar{b}$ is in the range of 7-70 nb/nucleon while the total inelastic cross section for proton-nucleon scattering is of the order of 13 mb/nucleon. The branching ratio of $J/\psi \to l^+l^-$ is $\approx 12\%$ and for $K^0_S \to \pi^+\pi^-$ is approximately 68%. One $B \to J/\psi K^0_S$ is expected to be produced per 10^{13} inelastic events. Therefore, it is not possible to read out and record each event, with in total 600.000 readout channels and an interaction rate of about 10 MHz this would mean 6 Tbit/s. This is why a highly selective trigger is needed.

HERA-B uses a multi stage trigger with a rejection factor of about 10^5 [8].

Pretriggers. The information about possible track candidates are provided by pretriggers implemented in three sub-detectors: ECAL, muon and high-pt.

- The muon pretrigger looks for coincident hits which form a track segment pointing to the target position. The information from the cathode pads in the last two superlayers (MU3, MU4) is used.

- The ECAL pretrigger searches for clusters consisting of 3 x 3 cells with an energy above a threshold. The threshold can be adjusted and the ratio of the energies deposited in the center cell and its neighbours can be applied as an additional selection criteria. The center of gravity of the selected clusters are used as starting points for the first level trigger lepton track search.

First Level Trigger. The first level trigger (FLT) is a hardware trigger which uses a discrete track following algorithm for track tracing. The algorithm starts from the seeds provided by the pretriggers (Muon and ECAL) and extrapolates backwards so called Regions of Interest (RoI) to the tracking superlayers, using as an assumption that the tracks originate from the target. If the algorithm finds a hit in a layer of the tracking station, the track information is updated and the search for coincident hits in the next layer in a smaller region of interest is performed. Fig. 2.4 shows the FLT algorithm schematically.

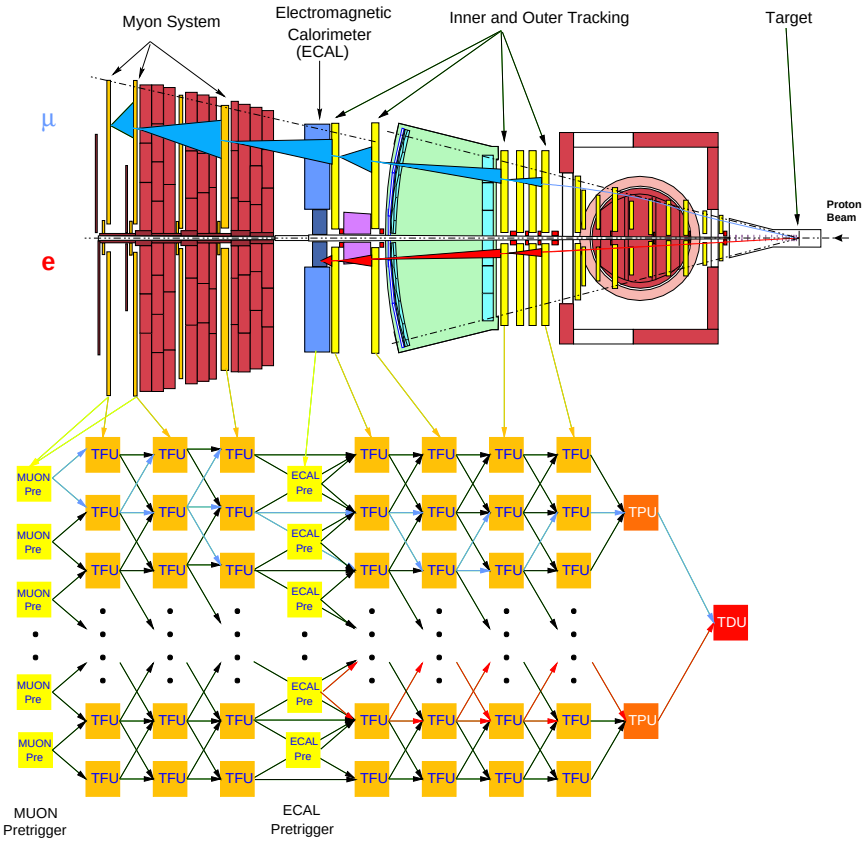

Figure 2.4: Schematic illustration of the first level trigger track tracing algorithm.

If the FLT succeeds to trace both tracks to the exit of the magnet spectrometer, the Track Parameter Unit (TPU) estimates the momenta of the tracks. For each pair of tracks an invariant mass is calculated, if the obtained mass exceeds a threshold the event is kept and otherwise rejected. In order to suppress the amount of data which has to be transfered from the readout electronics to the FLT, only four superlayers of the tracking

system are used. The maximum possible FLT output rate of the triggering setup is about 50 kHz.

Second Level Trigger. Next trigger step is the Second Level Trigger (SLT), implemented as a software trigger and based on a farm of 240 standard PCs. If an event is accepted by the FLT, all event information which is stored in the front-end electronics is transfered to the Second Level Buffer (SLB). Each triggered event is taken by one node of the SLT farm for processing. The algorithm starts from RoIs defined by the FLT and refines the track parameters using additional information about drift time of OTR and full resolution of the Inner Tracker. Finally, tracks which are reconstructed in the Main Tracker are propogated through the spectrometer magnet and track segments are reconstructed in the Vertex Detector. The event is accepted, if the trigger tracks can be matched with a VDS track segment and both tracks form a vertex. Complete information about the accepted event is than transmitted to the SLT node which forms the complete event record and transfers the record to the Fourth Level Trigger.

Fourth Level Trigger. The Fourth Level Trigger farm consists of 200 CPUs. At this stage a complete reconstruction of an event is performed with best knowledge about calibration and alignment constants. In parallel the search for interesting physical processes is performed, events with candidates are marked for fast offline access during the analysis.

At the end, raw detector information and output of the reconstruction program are stored in one record and archived on tape in the DESY computing center. The output rate at the end of the Fourth Level Trigger is limited to about 30 events per second.

Trigger Performance in 2002/2003. The above described trigger scenario suffered from the low efficiencies of the tracking stations and dead regions. Therefore a special trigger mode was used for data taking 2002/03, called the FLT/SLT "Star Mode".

Instead of two lepton track requirement in the FLT, only a single track is required. The SLT algorithm is started from the two pretrigger candidates. With this scenario a rate of more than 1000 J/Ψ per hour has been achieved and approximately 250.000 J/Ψs decaying in electron and muon channels have been collected.

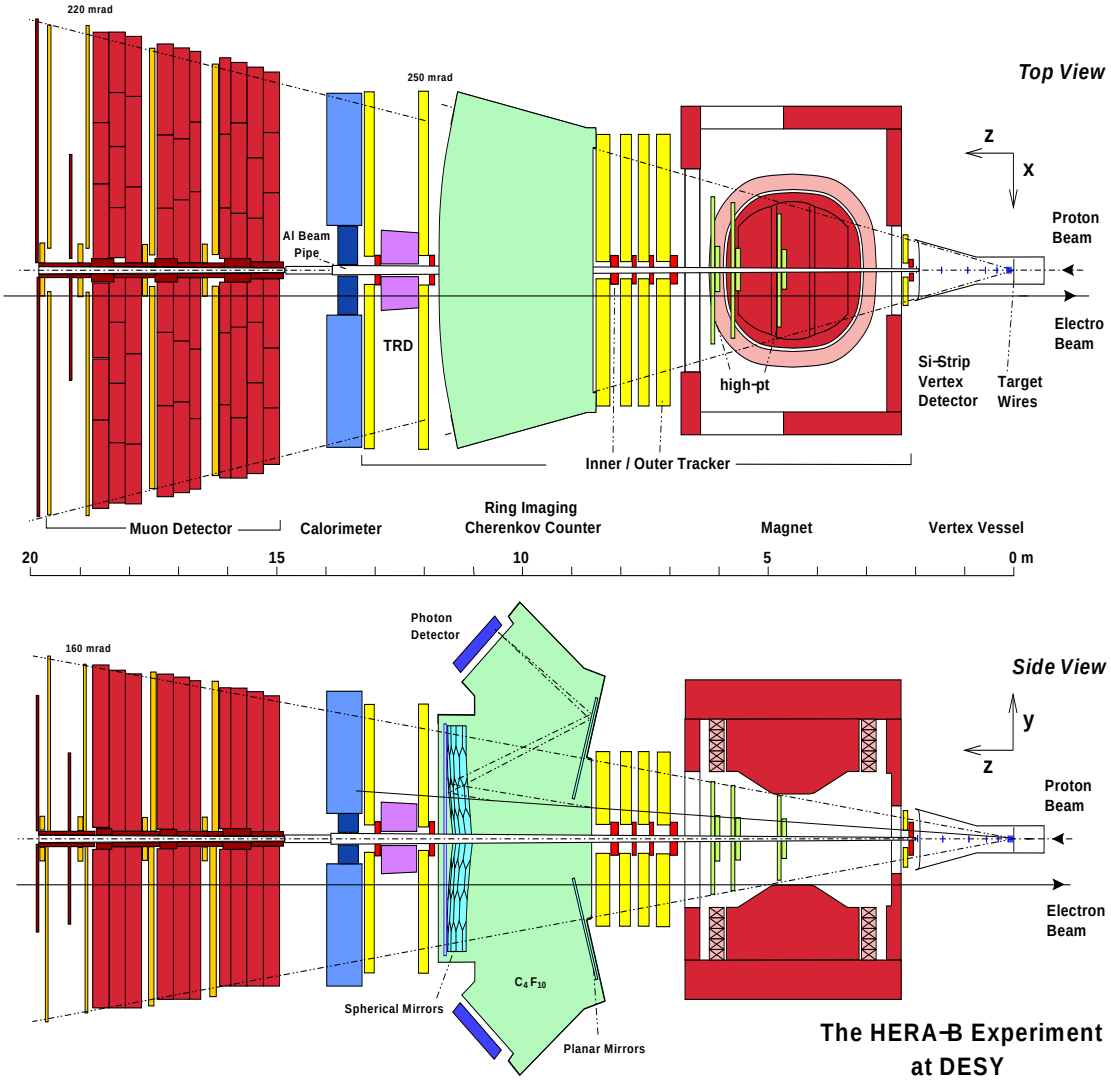

Figure 2.5: Schematic top and side view of the HERA-B experiment. From right to left can be seen vertex vessel with target wires, magnet, tracking stations, RICH vessel, electromagnetic calorimiter and muon system (2002-2003 setup).

Chapter 3

The Inner Tracker System

In order to deal with the high multiplicities at HERA-B, the main tracking system is divided into two parts. These parts use different technologies and different geometries.

Tracks in a range from 10-100 mrad are in the acceptance of the Inner Tracker. The Inner Tracker covers the region from the inner border of the Outer Tracker up to a distance of 6 cm around the beam axis. The detector was designed and built by the Universities Heidelberg, Siegen and Zuerich. In this chapter the used technologies and the final setup of the detector will be presented.

The Outer Tracker covers tracks which are in the range up to 250 mrad. The size of the outer tracker is from 20 cm till 290 cm in the plane perpendicular to the Z-axis of the experiment. It consists of honeycomb drift chambers. 5 and 10 mm cells are used in the inner and outer region respectively.

3.1 Requirements

The following requirements had to be fulfilled during the design of the Inner Tracker system:

Radiation and rate environment. The Inner Tracker covers the region from 6 cm till 27 cm, this is the region with the highest occupancy. Particle flux was assumed to be in the range from $2 \times 10^3 mm^{-2} sec^{-1}$ in the outer edge till $2 \times 10^4 mm^{-2} sec^{-1}$ near to the beam pipe. It was foreseen in the HERA-B proposal, that the detector has to deal with interaction rates up to 40 MHz. This could be translated to a radiation dose of ≈ 1 Mrad/year in the hottest area, the detector should work under such conditions for several years and should show stable performance and high efficiency during this time.

Granularity. The granularity was chosen based on the requirement that the number of hitted strips per event should not exceed 5-10%. The amount of *fake* tracks produced by the pattern recognition program can be sufficiently higher than the acceptable level, in case of higher multiplicity events. The high occupancy will also affect the efficiency of the first level trigger. In order to fulfill this requirement the pitch size was chosen to be $\approx 300\mu$m with the strip length up to 25 cm and about 350 μm pitch size for chambers with the strip length up to 27 cm.

Spatial resolution. The spatial resolution was required to be $\sigma_x \approx 100\mu$m in the bending plane of the spectrometer magnet, the resolution perpendicular to this plane should be $\sigma_y \approx 1$mm. The resolution along the proton direction should be $\sigma_z \approx 3$mm. All these requirements led to the decision to choose for the pitch size of the chambers inside the magnet and in front of the RICH vessel 300 μm and for the chambers situated between RICH and ECAL a pitch of 350 μm. The coordinate x is measured directly by the 0^0 wires the other coordinates are provided by chambers orientated in three stereo views (available $0^0, +5^0, -5^0$ views). The stereo angle was selected in such a way that the designed resolution in the y plane is reached and the amount of random coincidents is limited to an acceptable level.

Signal speed. The normal event (interaction of protons in a single bunch with the target) can occur every 96 ns. The electronics should be fast enough to be able to deal with this rate.

Trigger information. Some of the Inner Tracker superlayers have to provide informations for the FLT system. The FLT has to make a decision whether an event has to be kept or not in about 10 μsec. The front-end electronics of the Inner Tracker has to store the full hit information for the time period needed for the FLT to make its decision.

Magnetic field. A part of the Inner Tracker should operate in the magnetic field. The strength of the magnetic field is about 0.85 T. The resolution and efficiency of the chambers placed in the magnetic field have to fulfill the requirements mentioned above. No magnetic materials could be used during construction.

Radiation length. The critical point is the material used for the detector production. Therefore detectors and supports and also cables and gas pipes should be as thin as possible (measured in radiation length X_0), in order to suppress multiple scattering, bremsstrahlung and photon conversion. All these effects have a large influence on the momentum resolution and quality of the tracking.

3.2 Used technology

In order to fulfill all requirements the GEM-MSGC technology was chosen for the Inner Tracker system. The technology combines a Micro-Strip Gas Counter (MSGC) with a Gas-Electron Multiplier (GEM). A short description about operation principles of GEM-MSGC and the actual setup will be described in this chapter.

3.2.1 MSGC, GEM, GEM-MSGC

The idea behind a Micro Strip Gas Counter (MSGC) [9] is the same as that of a Multi-Wire Proportional Chamber (MWPC). Instead of wires in the MWPC an electrode structure

in the MSGC is used, it is produced on a solid substrate, in case of HERA-B specific glass is used. The solid support prevents different types of instability and allows to select a small readout pitch. As a result the intended granularity and spatial resolution could be achieved.

The electrode structure consists of anodes (typical width $\approx 10\mu m$) and cathodes (typical width $\approx 170\mu m$). The ground potential is applied to the anodes and negative voltage to the cathodes (≈ 500 V), they play the role of field wires in case of the MWPC. A drift field of several kV/cm is applied between the drift electrode and the MSGC structure which forces electrons deposited by an ionizing particle to drift toward the MSGC plane. The simulated distribution of the electrical field is shown in Fig. 3.1. The amplification occurs near the anodes, where the electrical field strength is maximum. The amplification factor can reach the order of several thousands. The advantage of the MSGC construction is that field cathodes are placed close to the anodes, the ions produced in the avalanche near the anodes are quickly removed, avoiding the build-up of space charges. A high field strength allows to speed up drift velocity and as a result provide fast chamber signals.

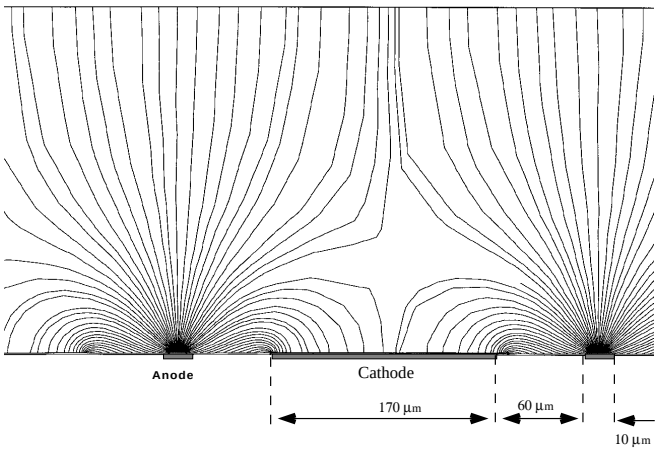

Figure 3.1: Simulated electrical field of the MSGC is shown. Gas amplification possible near the anodes which are located in the region with a maximum field strength. The typical sizes are indicated.

The robustness of the MSGC was tested with the help of an electron beam and photon sources (Fe 55) [10]. The device demonstrated stable behaviour and promised to survive during five years of operation in such environment. In the further tests, it turned out that the electrode structure of the detector in flux of pions and protons is destroyed nearly immediately. The reason for such a behaviour are discharges between anodes and cathodes, caused by heavy ionizing particles passing close to the surface of the MSGC and depositing a large amount of charge between cathode and anode. This phenomenon was observed for the first time during beam tests in PSI and later reproduced in the laboratory with the help of α-particle sources. These discharges ruled out the use of the pure MSGC solution in case of HERA-B.

The Gas Electron Multiplier (GEM) [11] is a thin insulating foil, copper-clad on both sides. The foil is perforated with a regular pattern of holes (for the perforating a chemical etching procedure is used). The GEM is placed in the homogeneous drift field between drift electrode and MSGC structure. The difference of potential between the two metal

sides is ≈ 400 V. The field lines are forced through the GEM holes and inside the holes gas amplification can occur. The amplification depends on the geometry of the holes, thickness of the metal-clad and field configuration above and below the GEM. With the voltages chosen for the Inner Tracker chambers the amplification at the GEM is in the range of 20-100.

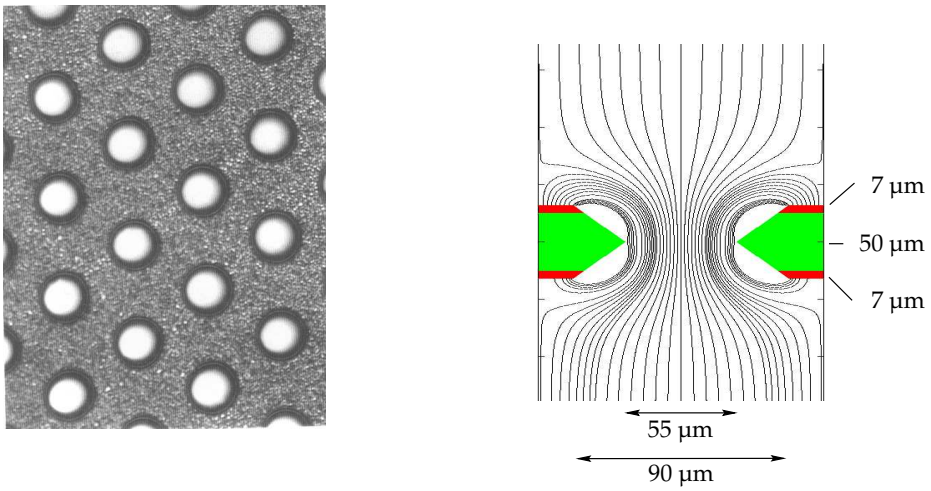

Figure 3.2: Left: a GEM foil used for the ITR system is shown. Right: The simulated electrical field inside the GEM hole is shown.

After a variety of tests in order to overcome the MSGC discharge problems, the solution was found by using MSGC with GEM as pre-amplification structure for the ITR system, this solution has proven to be resistant enough to be used. The main advantage of this setup is that the gas amplification occurs at two well separated stages and the gas gain at the MSGC structure can be reduced. With the help of the amplification separation, the discharge probability could be reduced by several orders of magnitude and a stable and efficient operation of the GEM-MSGC can be achieved also in hadronic beams.

3.2.2 GEM-MSGC at HERA-B

The GEM-MSGC chamber used in the Inner Tracker system of HERA-B is schematically shown in Fig. 3.3.

In case of HERA-B the GEM foil is a 50 μm thick Kapton foil claded with 7 μm copper layers on both sides. The GEM holes have a double conical shape with a diameter of about 55 μm at the narrowest point. The smallest distance between two holes is about 140 μm. All foils used for the construction of the ITR chambers were produced at the CERN workshop with the help of a photolithographic method. The GEM foil is stretched and mounted on a hollow frame.

The MSGC wafer is made out of 400 μm thin DESAG AF45 glass [13], coated with a 80 nm layer of amorphous carbon ("diamond like coating"). This coating has been produced by a CVD (chemical vapor deposition) process [12]. The coating is used to get a well-defined surface resistivity. The electrode structure is produced on top of this coating with a photo-lithographic process. The strips are made out of 500 nm gold, the

anode strips have a width of 10 μm the cathode strips of 170 μm, between anode and cathode is a 60 μm gap resulting in a pitch size of 300 μm. The number of strips per chamber is up to 756, depending on the type of the chamber.

The drift cathode is made of a compoud of 125 μm Kapton and 300 μm G10 copper cladded with 18 μm copper.

Three types of Inner Tracker chambers are used, they differ in the radius of the beam-pipe recess and outer dimensions. The chambers situated behind the RICH have a larger dimensions. In order to keep the number of readout channels per chamber constant the pitch size has been increased to 350 μm. The geometrical parameters of the chambers used in the different superlayers are summarized in Table 3.1.

As counting gas for the GEM-MSGC chambers a mixture of Ar/CO_2 has been chosen with a composition of 70 % $Argon$ and 30% CO_2.

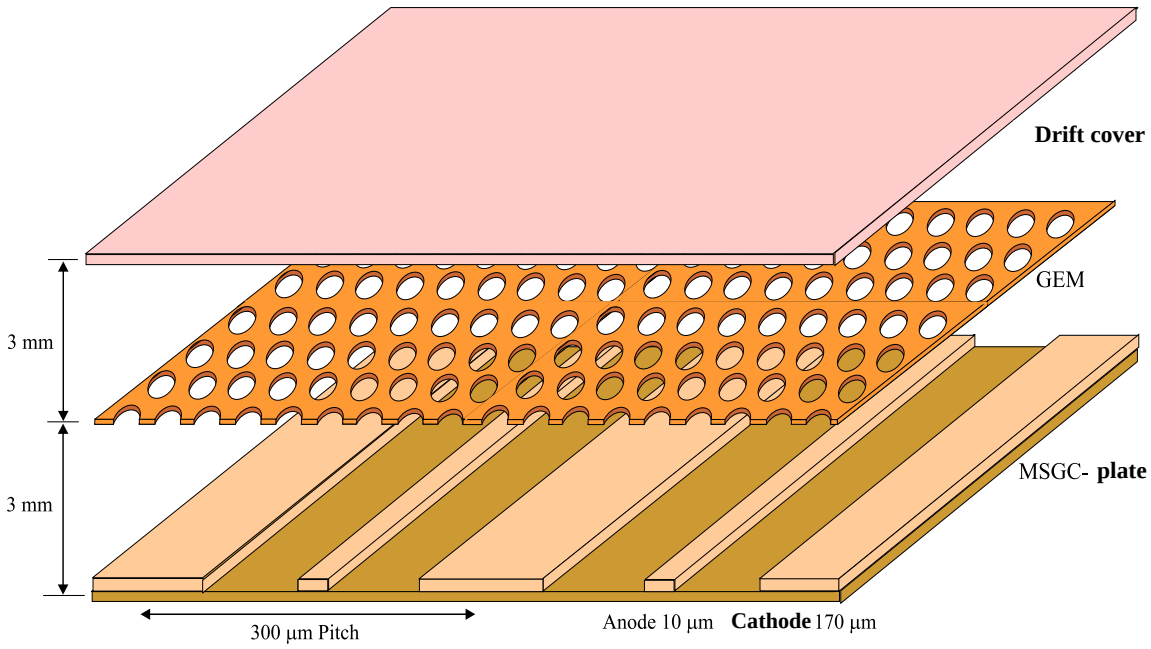

Figure 3.3: Sketch of the GEM-MSGC chamber used in the Inner Tracker system. The typical dimensions are indicated.

The use of the GEM in additional to the MSGC improved stability and solved the MSGC problems. However due to the introduction of the GEM foil the operation of the coupled GEM-MSGC device with 5 different electric potentials became more complicated [14].

3.3 The Inner Tracker system

One GEM-MSGC chamber allows to measure one coordinate of a track impact point. In order to perform track reconstruction several chambers have to be combined, to provide measurements of the track impact points in different stereo projections.

Type	Size	Superlayer	Pitch size	Beam-pipe recess	Number of anode strips
I	25 cm x 23 cm	MS01	300 μm	5.5 cm	752
II	25 cm x 23 cm	MS10 - MS13	300 μm	8 cm	752
III	27.5 cm x 27 cm	MS14,MS15	350 μm	12.5 cm	756

Table 3.1: The sizes of the Inner Tracker chambers corresponding to the different parts of the HERA-B detector.

With four L-shaped detectors one plane (*stereo layer*) around the beam-pipe can be covered. With the aim to avoid dead regions in the acceptance the chambers are arranged in such a way that their active volumes overlap. The detectors are mounted on support plates made of carbon fibre and Nomex honeycomb (see Fig. 3.6). Several layers with different stereo angles are combined into one tracking station (*superlayer*).

Each superlayer consists of two separate half-stations, they cover the area to the left and to the right of the beam-pipe ($-x$,$+x$). This allows to get access to the stations for maintenance and installation. The half-stations are mounted on the frames of the corresponding Outer Tracker stations (see Fig. 3.5).

The total number of Inner Tracker chambers is 184. They are grouped according to the tasks which they have to carry out (see Fig. 3.4): magnet tracking (MC, in the magnet spectrometer), pattern recognition (PC, between magnet and RICH) and triggering (TC, chambers between RICH and ECAL). The chambers placed in the TC area are mainly needed for trigger purposes, with the aim to prolongate seeds found by the calorimeter and muon pretrigger system into the main tracking system (PC, MC).

During the comissioning run in 1999/2000, 136 chambers were installed and routinely operated in the Inner Tracker system, missing were the TC chambers. During the shut-down in 2000-2001, the decision was made to remove the chambers inside the magnet region in order to improve the resolution of the ECAL. Therefore, in the running period 2002, 149 chambers were installed and operated, in the TC area only half (24 chambers) of the installed chambers were read-out.

In order to identify each chamber, the following naming convention was used. The first two numbers identify the superlayer (01, ... 15). The third and fourth character are a +- (x) and (y) indicating the position in the x and y direction respectively. The last digit indicates the position inside the superlayer. For example MS10+-3 is the third layer in station MS10, in the quadrant covering positive x and negative y.

The information summarizing the setup 2002 can be found in Tab. 3.2.

3.4 Infrastructure for Chamber Operation

For the GEM-MSGC chamber operation four different high voltages are needed: drift voltage U_{drift}, the voltage for the upper and lower side of the GEM foil, and the cathode voltage $U_{cathode}$. In order to save space and reduce the number of power supplies in the experimental hall, one power supply provides U_{drift} and $U_{cathode}$ for eight chambers. The two voltages needed for both sides of the GEM are derived from the drift voltage, the voltage difference U_{GEM} can be adjusted for each chamber individually.

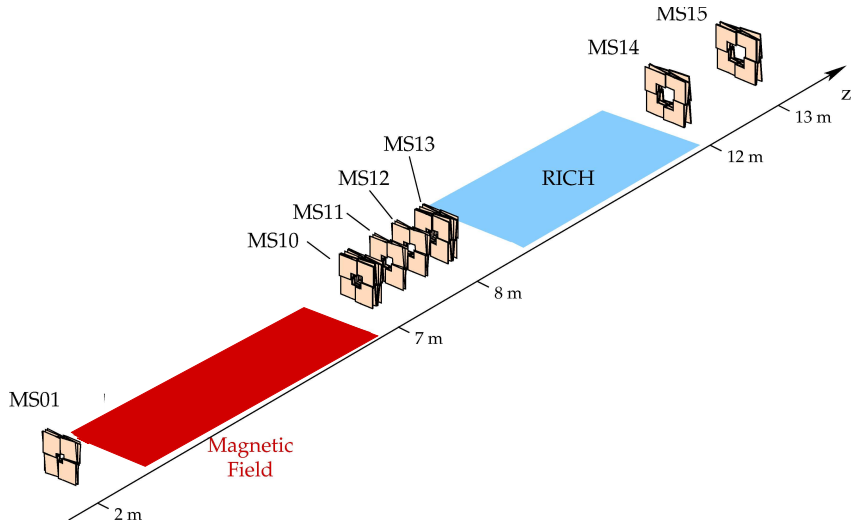

Figure 3.4: Location of the Inner Tracker superlayers along the beam axis (configuration of 2002). The z positions are indicated.

ITR station	number of chambers	Type	stereo views	contribution to the FLT
MS01	16	I	$0^0, -5^0, +5^0, 0^0$	no
MS10	32	II	$0^0, 0^0, -5^0, -5^0, 0^0, +5^0, +5^0, 0^0$	yes
MS11	16	II	$0^0, -5^0, +5^0, 0^0$	no
MS12	16	II	$0^0, -5^0, +5^0, 0^0$	no
MS13	32	II	$0^0, 0^0, -5^0, -5^0, 0^0, +5^0, +5^0, 0^0$	yes
MS14	24	III	$0^0, 0^0, -5^0, -5^0, +5^0, +5^0$	yes
MS15	24	III	$0^0, 0^0, -5^0, -5^0, +5^0, +5^0$	yes

Table 3.2: The configuration of the ITR tracking stations in 2002.

The front-end electronics of the Inner tracker system need a stable low voltage supply. The front-end electronics need voltages ± 5, $+3$, ± 2 V. The system was developed by a commercial supplier. Each half superlayer has its own low voltage power supply.

For the operation of the GEM-MSGC, a permanent exchange of the counting gas is needed. Due to aging problems specific to GEM-MSGC detectors, the gas system has to provide an extremely clean gas mixture. In order to avoid pollution of the gas, the materials used for the detector construction have been selected according to their out-gassing properties. The fact that part of the gas system is placed in the acceptance region of the experiment influenced the selection of the materials in addition. A rather critical point in the gas system is the controlling of the detector gas pressure relative to the ambient pressure. It has to be controlled with an accuracy of about 10 μbar.

The crucial point of the system is the steering system (Slow control system). It allows to tune applied voltages and to get the status information from all components of the system. Further access to the various informations (such as: actual voltages, currents, number of GEM sparks and etc) related to the performance of the detector during data

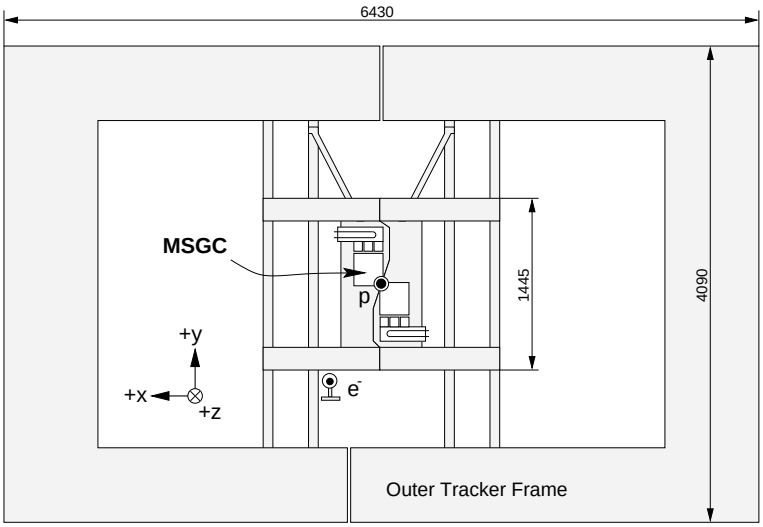

Figure 3.5: Mounting of the two half stations on the frame of the Outer Tracker station. The dimensions given for the chambers situated in the PC area.

taking is possible via a slow control database.

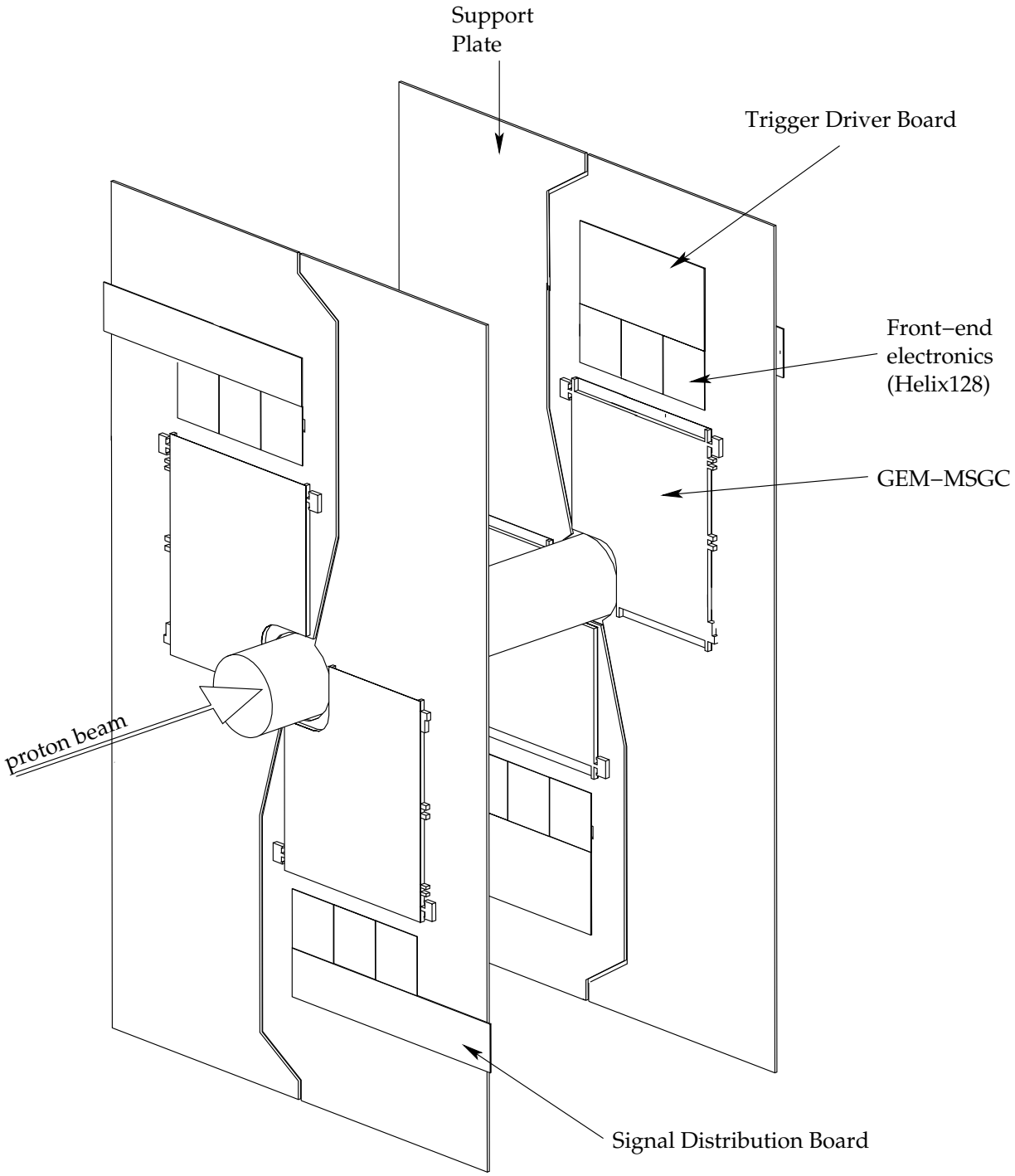

Figure 3.6: The drawing shows the construction of the support plates with mounted GEM-MSGC chambers. In order to cover all four quadrants, two layers of the supports are needed.

Chapter 4

Pattern recognition

This chapter describes the track reconstruction package OTR/ITR-CATS developed for the Pattern Tracker of the HERA-B experiment. This package employs a combined approach for track reconstruction based on the use of a cellular automaton for track searching and the Kalman filter technique for track fitting.

The developed package has been tested on simulated and real data. The results of the tests regarding reconstruction efficiency, accuracy of estimates and computing time are presented.

4.1 Introduction

In the general concept of the HERA-B experiment track reconstruction in the Pattern Tracker is the first step in the reconstruction chain. The next steps, magnet tracking and track prolongation to the trigger chambers, are essentially track following procedures which use tracks reconstructed in the pattern tracker as seeds.

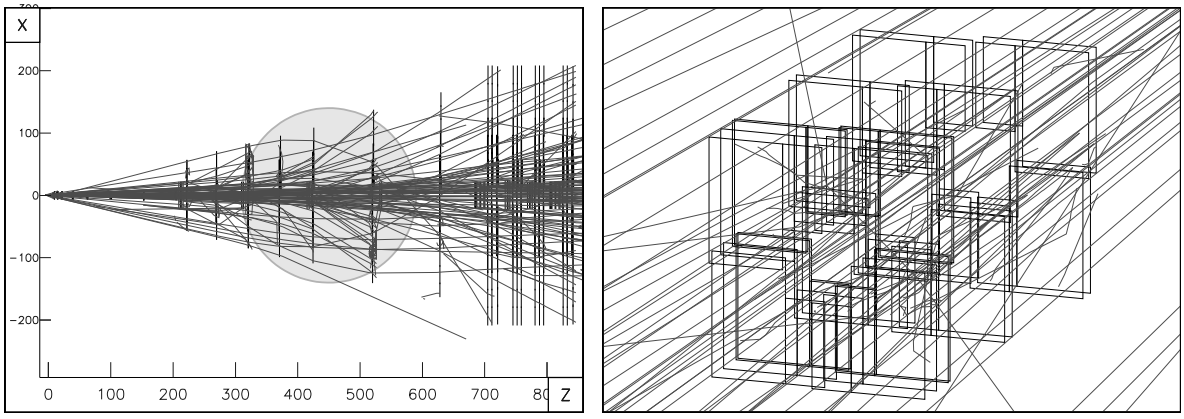

Figure 4.1: A typical simulated event: $J/\psi \to \mu^+\mu^-$ decay superimposed with two inelastic interactions. For details see text.

A typical simulated event demonstrating the large track density with the pronounced radial dependence is shown in Fig. 4.1. Evidently, not all tracks passing through the pattern tracker are straight-line high-momentum tracks coming from the vertex region.

There are also a considerable fraction of low-momentum tracks affected by multiple scattering which come from secondary interactions and in-flight decays. This is clearly visible in the isometric closeup (right figure) of the Inner Tracker section of the event shown in the left part of Figure 4.1. Due to the large track density the probability of track overlap is relatively high and any tracking algorithm must routinely cope with clusters of hits from nearby tracks. In the Outer Tracker, the problem of track recognition becomes even more complicated due to the small cell size in the drift chamber which makes resolution of the left-right ambiguity particularly difficult.

In the past years members of the HERA-B collaboration have performed an extensive analysis of different track recognition methods [25, 37, 38, 39]. In particular, the reconstruction package RANGER based on track following and concurrent track evolution has been developed. After extensive tests on simulated data, RANGER was chosen as the default track reconstruction package for HERA-B.

RANGER was tuned to the detector parameters expected for the original experiment design [28]. As a result, it has faced serious problems when the actual hit efficiencies of the detectors turned out to be lower than expected in [28] (the most pessimistic estimates are 90% for the OTR and 86% for the ITR). At the same time hit resolutions were also found to be worse than in the original design (lower bound estimates are 500 μm in the OTR and 200 μm in the ITR). In addition an unexpected large fraction of channels (up to 7%) in the Outer Tracker was insensitive due to high voltage problems.

These circumstances motivated new and alternative approaches to track reconstruction which should be more robust and tolerant against hardware problems than RANGER.

4.2 Methods of Track Recognition

In general, all track recognition methods can be divided into three classes: local, global and semi-global.

Local methods, also referred to as track following methods, need a starting initial set of track parameters for a track candidate called a "seed". These methods usually employ the Kalman filter with its advantages already at the track recognition stage. Given a seed, the algorithm follows the track by trying to find the next hit and improves the track parameters recursively with each new hit added. The method splits the track whenever more than one hit is observed in the neighborhood of the predicted hit location. In order to keep the number of simultaneously propagated track branches at a reasonable level, the algorithm must discard some of them relying upon a quality index of the track. Usually such an index is simply a weighted sum of the χ^2 of the track and a penalty on the number of "faults", i.e. cases when the algorithm could not find a hit in a detector plane.

The reconstruction package RANGER employs so-called concurrent track evolution approach which can serve as a good example of local track recognition methods. As was pointed out in [25], this algorithm is quite sensitive to detector efficiency and hit resolution. Above $\epsilon_{HIT} = 95\%$, the hit inefficiency is well compensated by the algorithm, while smaller hit efficiencies lead to sizeable losses in the fraction of detected particles. In the course of the track following procedure, RANGER decides to discard some track candidates using a χ^2-based quality index. Therefore the detector resolution becomes a crucial point for the ability of RANGER to separate real tracks from ghost tracks. At bad detector

resolution and large track density RANGER can provide a reasonable track reconstruction efficiency and ghost rate only by allowing a higher number of simultaneously explored track branches. This property of RANGER makes the computing time in case of bad detector resolutions grow excessively due to the dramatic increase of hit cobinations to be evaluated.

Global methods of track recognition use a parametric description of a track by a set of its parameters like slopes and offsets. Once the track model and detector measurement model are given, all hits in the detector can be projected into the track parameter space creating a complex density distribution with many local maxima. In this case the track recognition becomes a search for the local maxima corresponding to tracks. For a numerical implementation the density distribution is approximated using a multidimensional grid introduced in the track parameter space. The global methods are essentially maximum likelihood algorithms of parameter estimation. This property makes them, in principle, the most robust techniques for pattern recognition for simple geometries which allow parameterization, for instance, straight lines and circles.

One of the well-known global methods is Hough transform which was implemented in the reconstruction package TEMA [26].

A clear disadvantage of global methods is that they require an explicit track model, which makes them quite sensitive to random perturbations of the track caused, for example, by multiple scattering. Another problem arises from the grid approximation, since the separation of tracks with similar parameters depends on the cell size of the grid. Due to this fact any attempt to improve such separation leads to an increase in the number of grid nodes which, in turn, moves memory and CPU consumption beyond feasibility.

The drawbacks of the global approach for track recognition are improved in *semi-global methods* which try to enhance the efficiency of global methods by local formation of space-points or short track segments in neighbored detector planes. The algorithm employed in the package OTR/ITR-CATS described in this chapter belongs to the semi-global methods combining features of cellular automata for track recognition with the advantages of the Kalman filter for track fitting. In the next section we describe the basic principles and some details of track reconstruction techniques implemented in the CATS package.

4.3 CATS Track Recognition Strategy

The main development goals of CATS were the highest possible efficiency of track reconstruction and the minimization of the computational cost at each step of the track recognition procedure. This approach has resulted in the optimized track recognition strategy schematically shown in Fig. 4.2. As can be seen, the multi-step track reconstruction process for the OTR is similar to that for the Inner Tracker.

4.3.1 Association of Neighboring Hits into Clusters

This step is done only for hits in the OTR, since in this detector a track usually produces more than one hit in a layer (up to four in case of double layers). The main idea behind this preliminary clusterization is to resolve left-right ambiguity at least partially and suppress

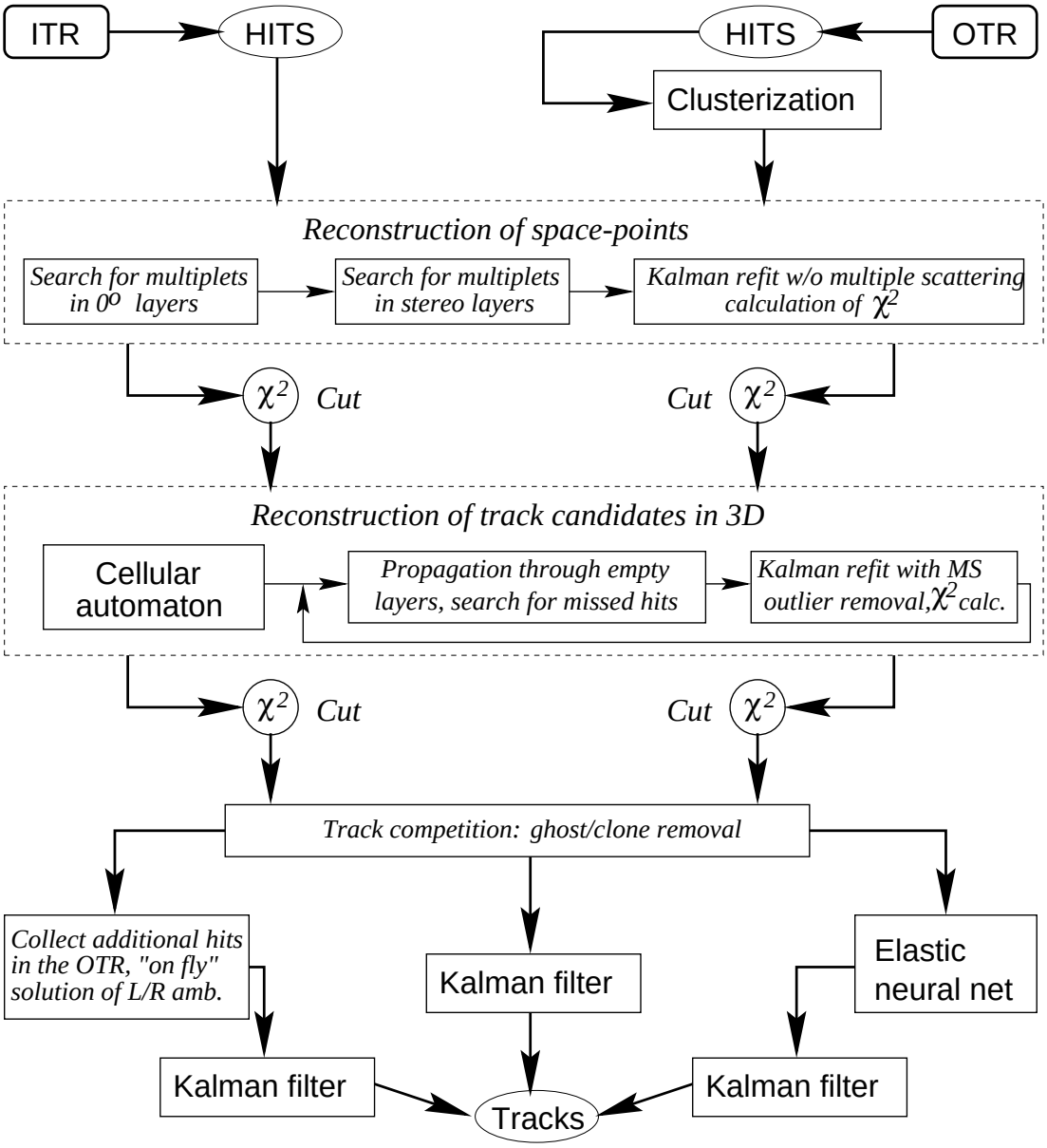

Figure 4.2: Flow chart of the track recognition process implemented in CATS.

combinatorial pile-up already at this early step of reconstruction.

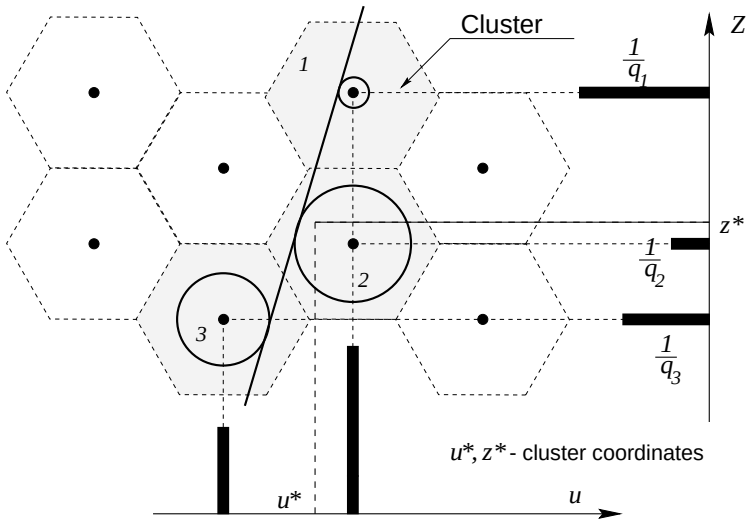

Figure 4.3: The method for hit clusterization in the OTR.

The clusterization process is illustrated in Fig. 4.3. In order to account for drift distance information, cluster coordinates $(u^*,\ z^*)$ are calculated as a weighted sum of the coordinates of the wires participating in the cluster:

$$u^* = \frac{\sum\limits_{i=1}^{N} w_i(q_i)u_i}{\sum\limits_{i=1}^{N} w_i(q_i)}, \qquad z^* = \frac{\sum\limits_{i=1}^{N} w_i(q_i)z_i}{\sum\limits_{i=1}^{N} w_i(q_i)},$$

where q_i is a measured drift distance for the i-th wire, and the weighting function $w(\cdot)$ is given by

$$w(q) = \frac{1}{q}.$$

This dependence simply reflects the fact that the smaller the drift distance, the closer to the wire a particle passed. Of course, in case of large occupancies, the clusterization can give clusters with noise and wrongly associated hits from nearby tracks. In CATS the problem of identification and rejection of such hits is solved at the final step of the track recognition process.

4.3.2 Reconstruction of Space-Points

This step is common for both ITR and OTR. The only difference is the input – clusters for the OTR and hits for the ITR.

In the framework of the CATS algorithm, the term *space-point* means a short 3D track segment inside a superlayer. The space-points are reconstructed by first searching for hit (cluster) multiplets in the 0^o-layers and then attaching multiplets in the stereo layers. The parameters of 0^o-multiplets are estimated using the Least Squares Method (LSM). The combined 0^o- and stereo-multiplets are used as space-point candidates and are fitted by a

Kalman parameter estimator (KPE). The KPE is a Kalman-type filter that estimates four (x_0, y_0, t_x, t_y) parameters of a space-point at a given reference z-plane and also calculates the χ^2 value for the space-point. Only space-points which successfully pass a cut on χ^2 are used. An example of an event with reconstructed space-points is shown in Fig. 4.4.

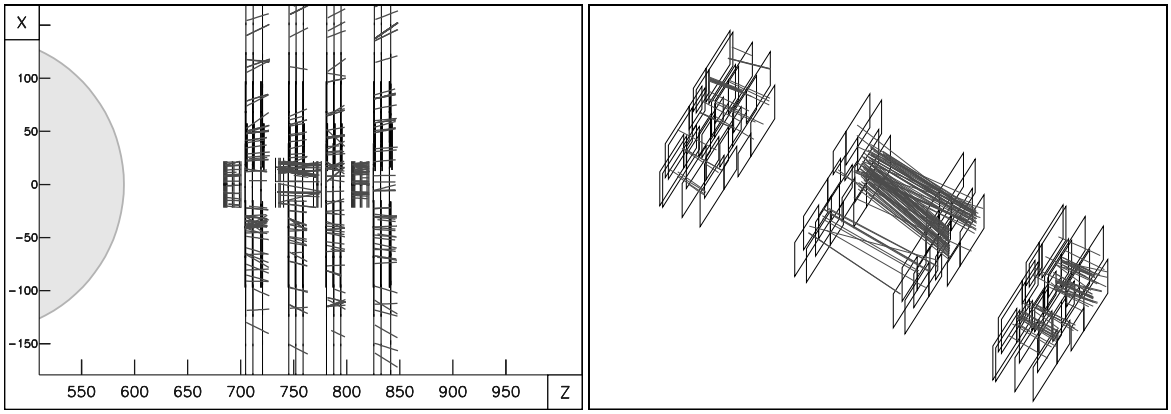

Figure 4.4: Reconstruction of space-points — short 3D track segments inside superlayers.

4.3.3 Reconstruction of Track Candidates

In this step CATS creates track candidates out of space-points and collects hits missed in layers where space-points could not be reconstructed due to dead regions or detector inefficiencies.

The first task is fulfilled by a cellular automaton, which uses space-points as input elementary units or *cells*. A cellular automaton is a discrete-time dynamical system that evolves in a phase space consisting of cells. Lets denote the space-points as s_{ij}, where i is the number of superlayer, $i = 1, \ldots, N$, j is the number of a space-point inside i-th superlayer and each space-point is defined by a set of its parameters: $s = \{x, y, t_x, t_y\}$. At any moment k of discrete time, each cell (or space-point) can take several states $p_{ij}^k = \{1, 2, \ldots, N\}$. The automaton's evolution, i.e. evolution of the cell states, is determined by a set of *rules* (for instance, a table) according to which the new state of a cell is calculated on the basis of the states of its *neighbors* in the next and previous superlayers. The final value of a state p_{ij}^n is equal to a position of the space-point s_{ij} on a reconstructed track candidate. All initial states p_{ij}^0 are assumed to be equal unity.

After initialization the cellular automaton performs the following loop over superlayers $L = 2, \ldots, N$, starting with the second superlayer, $L = 2$:

1. For each space-point s_{Lj} the automaton finds its neighbors in the previous superlayer $L - 1$. A space-point $s_{L-1,l}$ is regarded as neighboring if

$$D(s_{ij}, s_{L-1,l}) \leq D_{max},$$

where $D(\cdot, \cdot)$ is a χ^2-distance between two space-points, D_{max} is a predefined cut.

2. If a neighbor is found, the new value of the state p^k_{Lj} is calculated as follows

$$\widetilde{p}^k_{Lj} = p^k_{Lj} + \begin{cases} 1, \text{ if } p^k_{L-1,l} = p^k_{Lj} \\ 0, \text{ if } p^k_{L-1,l} \neq p^k_{Lj} \end{cases} .$$

3. When the automaton calculates new states for all space-points in all superlayers, the states are updated simultaneously and the algorithm proceeds with the next iteration:

$$p^{k+1}_{Lj} = \widetilde{p}^k_{Lj}, \qquad k = k+1, \qquad L = 2, \ldots, N.$$

If, during an iteration, all states keep their values, the automaton stops the iteration and proceeds with the collection of track candidates:

1. The algorithm starts with space-points for which $p^n_{ij} = N$.

2. If they exist, the algorithm finds a neighbor for each such space-point in the previous superlayer so that

$$p^n_{i-1,l} = p^n_{i,j} - 1.$$

3. If such a neighbor exists, the algorithm tries to find its neighbor in the $(i-2)$-th superlayer and so on, creating a branch or track candidate.

4. If, in some superlayer, more than one neighbor is found, the algorithm splits the candidate into two branches which are then propagated independently.

5. The collection of a track candidate is completed if the algorithm found a neighboring space-point with $p^n = 1$.

When all branches starting with states $p^n_{ij} = N$ are completed, the algorithm proceeds with the remaining space-points with lower states $p^n_{ij} = N - 1$, and so on.

All collected track candidates are refitted by the Kalman parameter estimator, candidates with a bad χ^2 are discarded.

Further details on the application of cellular automata for track searching can be found in [24].

The clear advantage of a cellular automaton is its intrinsic simplicity which makes tracking based on it extremely fast. Unfortunately, the search for tracks performed by a cellular automaton is not exhaustive, for example, if, in an intermediate superlayer, there is no neighboring space-point, the cellular automaton cannot jump over such a hole. This problem is typical in case of dead regions in the OTR.

Due to this reason, in CATS, the tracking based on a cellular automaton is accompanied by a simple (and fast) track following procedure. As seeds, this procedure uses track candidates found by the cellular automaton and space-points for which the automaton could not find any neighbors.

A special track following procedure is also used for propagation of track candidates reconstructed in the ITR into the Outer Tracker. Since the hit resolution of the ITR is much better than for the OTR, it is possible to resolve L/R ambiguity "on the fly", i.e., in the course of the track following. Therefore this particular procedure works with the OTR hits rather than clusters of hits. An example of the picture obtained at this step of the CATS reconstruction chain is shown in Fig. 4.5.

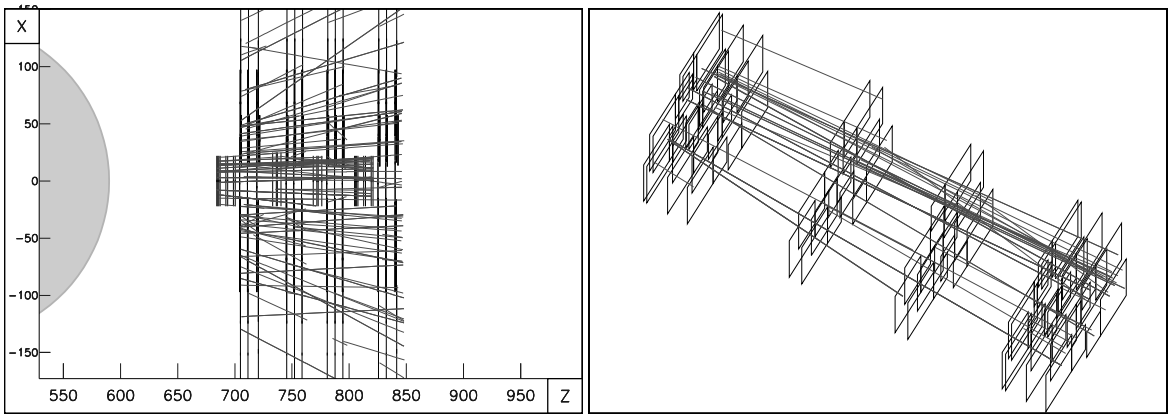

Figure 4.5: Track candidates reconstructed by the cellular automaton after the track following procedure.

4.3.4 Track Competition for Clone and Ghost Removal

At the beginning of this phase of the reconstruction all track candidates are sorted according to their length. Starting with the longest candidate the algorithm marks all hits belonging to these candidates as *used*. Proceeding track by track, the algorithm checks how many hits belonging to the track have already been used. If the fraction of used hits exceeds some predefined level (in the current version — 30%), the track is discarded. If the track has survived, all its hits are marked as used.

The main idea of this procedure is straightforward: to favor the longest tracks and to get rid of short ghost tracks and nearby clones[1]. Studies on simulated data have shown that this track competition procedure drastically reduces the ghost level while the reconstruction efficiency is only slightly reduced. The event already depicted in Fig. 4.5 is again shown in Fig. 4.6 after clones and ghosts are removed.

4.3.5 Left-Right Ambiguity Resolution

It is mentioned already, problems with the left-right ambiguity resolution occur naturally in the reconstruction of tracks in the OTR. In addition, the algorithm for the left-right ambiguity resolution allows to eliminate noise and wrongly associated hits.

In this step it is assumed that the track recognition is completed. Each track candidate is simply a sequence of fired wires $\{w_i\}$, $i = 1, \ldots, N$ for which two problems have to be solved:

1. Detection and removal of outliers, i.e. hits that most likely do not belong to the track.

2. Resolution of left-right (L/R) ambiguity for the other hits.

To solve both problems CATS uses a very promising approach that was proposed recently [42, 43]. This approach is based on so-called elastic neural nets (ENN) [40, 41] and generally employs the following heuristic idea:

[1] *A clone* is a track that is reconstructed more than once.

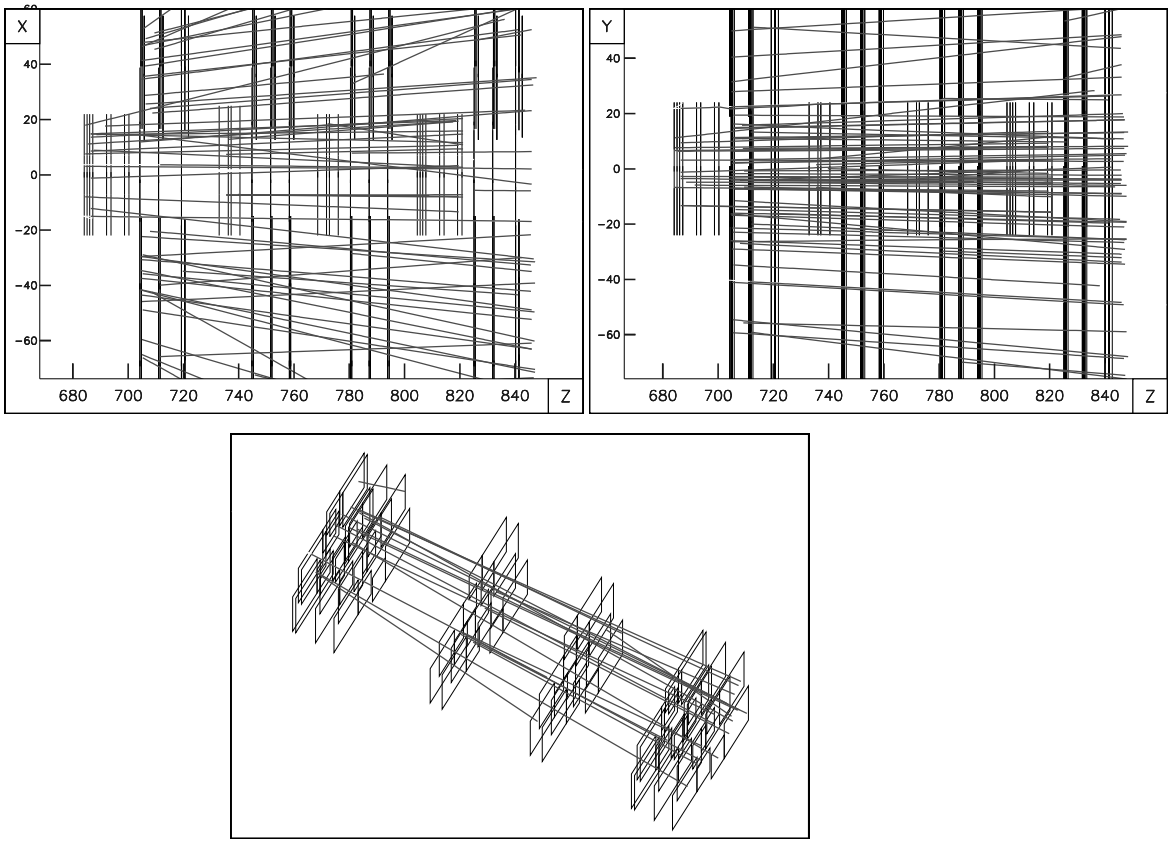

Figure 4.6: The final event reconstruction.

In the presence of multiple scattering a track can be defined as the longest and the smoothest line which approaches the drift circles as close as possible.

Following this idea the problem of L/R ambiguity resolution and removal of outlying hits can be considered as an optimization problem in a form of either a variational problem or a problem of optimal trajectory control. Naturally, the optimization criterion is to be a sum of

1. penalty on non-smoothness of a track;

2. penalty on a sum of the minimal distances between the track and drift circles around the wires.

The latter term can also account for outlying hits: for large distances between the track and a given drift circle the penalty for the hit should be decreased in order to suppress the influence of outliers on the optimal solution.

Mathematically the ENN algorithm is an iterative numerical method to solve the given optimization problem. This method to solve L/R ambiguities has already successfully been applied to similar problems in [42, 43]. The ENN in its elastic arm modification has also been studied by members of the HERA-B collaboration [39] where a full description and a detailed analysis of the method are presented.

Starting from the general ENN-based method to solve L/R ambiguities we describe a simplified version of the algorithm as implemented in CATS and applicable for relatively fast tracks.

The ENN algorithm employs a *segment* model for track description: a track is considered as a sequence of neighboring straight-line segments connecting nodes of the ENN — points in 3D space which can change their positions during iterations of the method. The ENN which is implemented in CATS consists of two interacting arms (lower and upper ENNs in Fig. 4.7), each arm includes M nodes. The initial positions of the nodes on both ENN arms are chosen to fully encompass a given sequence of drift circles around the wires fired $\{w_i\}$, $i = 1, \ldots, N$.

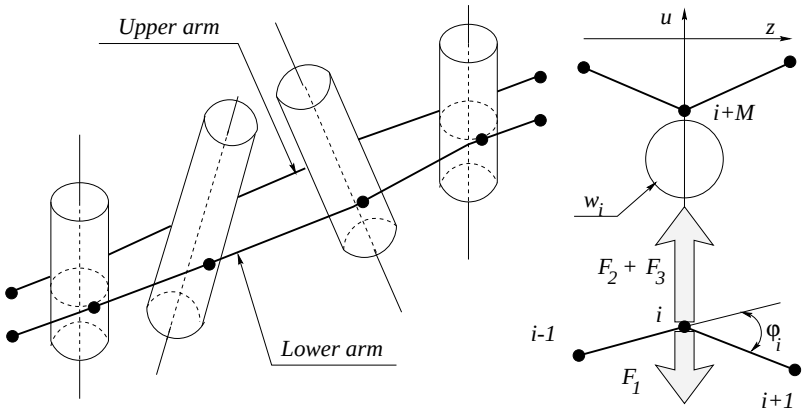

Figure 4.7: Left: segment track model in a two-arm elastic neural net, right: ENN node dynamics — for details see text.

During an iteration an ENN node i moves under the influence of three forces:

- the retracting force F_1 that tries to improve the smoothness of the track by minimizing the breaking angle ϕ_i between the two neighboring segments sharing the node;
- the attracting force F_2 that pulls the node to the nearest drift circle w_i;
- the attracting force F_3 that brings together opposite nodes i, $i + M$ on the lower and upper arm.

All three forces, F_1, F_2, and F_3, depend on the mutual position of a node, its counterpart in the other arm and the nearest drift circle. It is assumed that the changes in the node's positions, u, due to the different forces are described by the following equations:

$$\Delta u_1 = \beta\phi_i, \qquad \Delta u_2 = \alpha\rho_i, \qquad \Delta u_3 = \gamma\left(u_{i+N} - u_i\right),$$

where ρ_i is the residual between the node and the nearest drift circle, α, β and γ are coefficients linearly changing during iterations:

$$\alpha = \alpha_1 j, \qquad \beta = \beta_1\left(1 - \beta_2 j\right), \qquad \gamma = \gamma_1 j.$$

Here j is the number of the iteration, α_1, β_1, β_2, and γ_1 are adjustable parameters of the algorithm.

In each iteration the positions of all nodes are updated according to the equation:

$$u_i^{(j+1)} = u_i^{(j)} + (\Delta u_1)_i^{(j)} + (\Delta u_2)_i^{(j)} + (\Delta u_3)_i^{(j)}, \quad i = 1, \ldots 2M.$$

This approach is very general, it can, in principle, be applied to a wide spectrum of track reconstruction problems from reconstruction of straight, high-momentum tracks to fits of low-momentum hard scattered, even broken, tracks (the latter is the case in [42, 43]). However, the algorithm can be simplified and made significantly faster, if the specific circumstances of the experiment are taken into account. CATS is dealing with relatively fast straight-line tracks. Most of the tracks which are of physics interest have momenta well above 1 GeV. Thus it is feasible to substitute a deformable segment-wise double ENN by a single straight-line rigid template.

The template's dynamics is described as a motion under the influence of an attraction force pulling towards the drift circles. In order to suppress the influence of outlying hits the force depends on the distance between the template and a drift circle decreasing for large distances. Let $R_k = (x_k, y_k, t_{xk}, t_{yk})$ be a vector of the template's parameters at k-th iteration. The algorithm assigns two weight coefficients C_i^- and C_i^+ to each drift circle:

$$C_i^-(R_k) = f(\rho_i^-(R_k)), \qquad C_i^+(R_k) = f(\rho_i^+(R_k)), \qquad i = 1, \ldots, N,$$

where $f(\cdot)$ is the truncated normal density function, $\rho^+(\cdot)$, $\rho^-(\cdot)$ are the residuals between the template defined by the vector R_k and the drift circles corresponding to L/R equal $+1$ and -1. Using weights the vector R is updated as follows:

$$R_{k+1} = R_k + \beta_k \left(R_m - R_k\right),$$

where β is a coefficient approaching unity during the iteration process. The vector R_m is a solution of the following auxiliary optimization problem:

$$R_m = \arg\min_R \sum_{i=1}^{N} \left(C_i^-(R_k) \left(\rho_i^-(R)\right)^2 + C_i^+(R_k) \left(\rho_i^+(R)\right)^2 \right).$$

Studies on simulated data have shown that this algorithm provides remarkably high efficiency of the L/R ambiguity solution and very low level of noise hits. This is very important since an insufficient quality of L/R resolution and noise contamination in tracks can deteriorate the accuracy of the estimates produced by the Kalman refit of the reconstructed tracks.

4.3.6 Track Fit by the Kalman Filter and Smoother

As already noted, using Kalman filtering techniques is one of the basic principles of the CATS track reconstruction strategy. The Kalman filters and Kalman-type parameter estimators are embedded in

- space-point parameter estimation during space-point reconstruction;
- propagation of track candidates through empty superlayers and gathering of missed hits during the track following procedure;

- outlier detection and elimination;
- smoothed refit of reconstructed segments. This refit includes the treatment of multiple scattering effects using a preliminary estimate of the track momentum. It is the final step of track reconstruction.

The Kalman filter addresses the general problem of trying to estimate the state vector R of a discrete-time process that is governed by the *linear* stochastic difference equation

$$R_k = A_{k-1}R_{k-1} + \nu_{k-1}, \qquad k = 1, \ldots, N, \tag{4.1}$$

where the matrix A_{k-1} relates the state at step $k-1$ to the state at step k. $\{\nu\}$ is a *process noise*, a sequence of independent Gaussian variables which can, for example, account for the multiple scattering influence on the state vector. Within the model (4.1) a track in the Pattern Tracker can be described as a straight-line motion in the presence of Gaussian disturbances:

$$\begin{aligned} x_k &= x_{k-1} + t_{x\,k-1}(z_k - z_{k-1}), & y_k &= y_{k-1} + t_{y\,k-1}(z_k - z_{k-1}), \\ t_{x\,k} &= t_{x\,k-1} + \nu_{x\,k-1}, & t_{y\,k} &= t_{y\,k-1} + \nu_{y\,k-1}. \end{aligned} \tag{4.2}$$

The state vector $R_k = \left(x,\, y,\, t_x,\, t_y\right)^T$ describes the track parameters taken at the detector plane with $z = z_k$. T denotes transposition, the random variables $\nu_{x\,k}$, $\nu_{y\,k}$ describe the influence of multiple scattering on the track when it passes through detector plane $z = z_k$, $k = 0, 1, \ldots$. According to the track model (4.2), the matrix A in equation (4.1) has the form

$$A_k = \begin{pmatrix} 1 & 0 & \Delta z_k & 0 \\ 0 & 1 & 0 & \Delta z_k \\ 0 & 0 & 1 & 0 \\ 0 & 0 & 0 & 1 \end{pmatrix}, \qquad \Delta z_k = z_k - z_{k-1}, \quad k = 1, 2, \ldots.$$

In CATS the detector volumes and insensitive walls are treated as so-called *thin scatterers* [25]. For such scatterers, the non-zero elements q_{ij} of the covariance matrix Q_k of the noise vector $\nu = (\nu_x, \nu_y)$ equal to

$$\begin{aligned} q_{33} &= p^2\sigma^2_{MS}(1 + t_x^2)(1 + t_x^2 + t_y^2)\sqrt{1 + t_x^2 + t_y^2}, \\ q_{34} &= q_{43} = p^2\sigma^2_{MS}t_x t_y(1 + t_x^2 + t_y^2)\sqrt{1 + t_x^2 + t_y^2}, \\ q_{44} &= p^2\sigma^2_{MS}(1 + t_y^2)(1 + t_x^2 + t_y^2)\sqrt{1 + t_x^2 + t_y^2}, \end{aligned}$$

where p is an external estimate of the inverse momentum of the particle, σ^2_{MS} is the mean variance of the multiple scattering angle for a 1 GeV particle.

The input to the filter is a sequence of measurements $\{u\}$ which are described by a *linear* function of the state vector R

$$u_k = H_k R_k + \eta_k, \qquad k = 1, \ldots, N, \tag{4.3}$$

where the matrix H_k in the *measurement equation* (4.3) relates the state to the measurement u_k, η_k is a sequence of Gaussian random variables with the covariance matrix V_k.

The ITR and OTR have different measurement models. In addition, the OTR measurement model needs linearization. The matrix H_k for the ITR reads:

$$H_k = \Big[\cos\alpha_k,\ -\sin\alpha_k,\ 0,\ 0\Big],$$

where α_k is the rotation angle of the strips in the ITR plane $z = z_k$. The linearized measurement matrix for the OTR has the form:

$$H_k = \frac{1}{\sqrt{1+t_{uk}^2}}\Big[\cos\alpha_k,\ -\sin\alpha_k,\ -\frac{\Delta u_k\cos\alpha_k}{1+t_{uk}^2},\ \frac{\Delta u_k\sin\alpha_k}{1+t_{uk}^2}\Big],$$

where α_k is the rotation angle of the sensitive wires in the OTR plane $z = z_k$, and

$$t_{uk} = t_{xk}\cos\alpha_k - t_{yk}\sin\alpha_k, \quad \Delta u_k = x_k\cos\alpha_k - y_k\sin\alpha_k - w_k,$$

where w_k is the x-coordinate of the k-th wire in the rotated coordinate system.

Let's define $\widehat{R}_k$ to be a *state estimate* at step k after processing measurement u_k. The main idea of the Kalman filter is that the optimal (in mean-square sense) estimate $\widehat{R}_k$ should be the sum of an extrapolated estimate $\widetilde{R}_k$ and a weighted difference between an actual measurement u_k and a measurement prediction $H_k\widetilde{R}_k$

$$\widehat{R}_k = \widetilde{R}_k + K_k(u_k - H_k\widetilde{R}_k), \qquad \text{where } \widetilde{R}_k = A_{k-1}\widehat{R}_{k-1}.$$

The matrix K_k is called the *filter gain* and is chosen to minimize the sum of diagonal elements of an estimation error covariance matrix $\widehat{\Gamma}_k$. By definition,

$$\widehat{\Gamma}_k = \mathbf{E}\Big[(R_k - \widehat{R}_k)(R_k - \widehat{R}_k)^T\Big],$$

where $\mathbf{E}$ denotes the mathematical expectation. Note, that for both detectors, OTR and ITR, the measurement models are scalar. In this case the minimization leads to the following formula for K_k

$$K_k = \frac{\widetilde{\Gamma}_k H_k^T}{V_k + H_k\widetilde{\Gamma}_k H_k^T},$$

where $\widetilde{\Gamma}_k$ is the extrapolated estimation error covariance matrix $\widehat{\Gamma}_{k-1}$. The formula for $\widetilde{\Gamma}_k$ follows from equation (4.1):

$$\widetilde{\Gamma}_k = A_{k-1}\widehat{\Gamma}_{k-1}A_{k-1}^T + Q_{k-1}.$$

The new minimized value of the error covariance matrix $\widehat{\Gamma}_k$ is defined by the equation

$$\widehat{\Gamma}_k = (I - K_k H_k)\,\widetilde{\Gamma}_k,$$

where I is the unity matrix.

The computational algorithm of the discrete Kalman filter consists of two steps:

1. Prediction step — extrapolation of the estimate $\widehat{R}$ and the error covariance matrix $\widehat{\Gamma}$ to the next step of the algorithm.

$$\widetilde{R}_k = A_{k-1}\widehat{R}_{k-1}, \qquad \widetilde{\Gamma}_k = A_{k-1}\widehat{\Gamma}_{k-1}A_{k-1}^T + Q_{k-1}. \tag{4.4}$$

2. Filtering step

   (a) the gain matrix calculation

$$K_k = \frac{\widetilde{\Gamma}_k H_k^T}{V_k + H_k \widetilde{\Gamma}_k H_k^T}, \tag{4.5}$$

   (b) the updated estimate

$$\widehat{R}_k = \widetilde{R}_k + K_k(u_k - H_k \widetilde{R}_k), \tag{4.6}$$

   (c) the updated error covariance matrix

$$\widehat{\Gamma}_k = (I - K_k H_k)\, \widetilde{\Gamma}_k. \tag{4.7}$$

The two steps, prediction and filtering, are repeated until all measurements are processed.

In order to speed up the CATS reconstruction procedure, all fitting routines are written using the optimized numerical implementation of the Kalman filter algorithm described in [24]. In general, there are several ways to reduce the computational cost of the standard Kalman filter/smoother algorithm:

- calculate the covariance matrix in triangular form taking its symmetry into account;
- optimize the procedure to update the covariance matrix.

The most time-consuming parts of the filtering step are the calculation of the gain matrix and the updated covariance matrix. Let's rewrite (4.5) as follows

$$K_k = s_k^{-1} B_k,$$

where the vector B and the scalar s are

$$B_k = \widetilde{\Gamma}_k H_k^T, \qquad s_k = V_k + B_k^T H_k^T.$$

In terms of B and s the filtering step can be simplified. The optimized update of the triangular covariance matrix reads

$$\widehat{\Gamma}_{ij} = \widetilde{\Gamma}_{ij} - B_i K_j, \quad i = 1, \ldots, 4, \quad j = i, \ldots 4. \tag{4.8}$$

In order to get smoothed estimates at each point of a track, CATS employs the standard backward Kalman smoother. The smoother is an recursive algorithm that starts with the last point $k = N$ and updates the estimates and their covariance matrix at the next point $k = N-1$ using the estimates and the covariance matrix given by the Kalman filter at the last point. The update of the estimate $\widehat{R}_{N-1}$ is described as follows

$$\widehat{R}^s_{N-1} = \widehat{R}_{N-1} + C_{N-1}\left(\widehat{R}^s_N - A_{N-1}\widehat{R}_{N-1}\right),$$

where superscript "s" denotes a smoothed value, C_{N-1} is the *smoother gain* given by the equation

$$C_{N-1} = \widehat{\Gamma}_{N-1} A_{N-1}^T \widetilde{\Gamma}_N^{-1}.$$

The calculation of C_{N-1} requires the inversion of the 4×4 symmetrical matrix $\widehat{\Gamma}_N$ at each point. The smoothed covariance matrix reads

$$\widehat{\Gamma}^s_{N-1} = \widehat{\Gamma}_{N-1} + C_{N-1}\left(\widehat{\Gamma}^s_N - \widetilde{\Gamma}_N\right) C^T_{N-1}.$$

By definition $\widehat{\Gamma}^s_N = \widehat{\Gamma}_N$ and $\widehat{R}^s_N = \widehat{R}_N$. After updating point $k = N-1$ the smoother proceeds with point $k = N-2$ and so on until it reaches the first point $k = 0$. To update the k-th point the smoother uses smoothed values of $\widehat{R}^s$ and $\widehat{\Gamma}^s$ already calculated at the previous, $(k+1)$-th, point.

4.4 Performance Comparison

The CATS package was extensively tested on simulated data using as references two other track reconstruction packages, RANGER and TEMA. The evaluation procedure, criteria of the evaluation and results are summarized below. All described tests were performed for the HERA-B setup 2000, with ITR and OTR chambers in the MC area.

It should be mentioned that all three packages work within the standard reconstruction framework of HERA-B, which includes such modules as:

- hit preparation for the Inner and Outer tracker,
- pattern recognition in the PC area (can be used: CATS, RANGER, TEMA),
- track prolongation into the MC and TC area,
- usage of SLT tracks as seeds for pattern recognition in PC area,
- matching of track segments reconstructed in different areas,
- track creation (RTRA) and refitting with full knowledge about traversed material.

The track reconstruction strongly depends on the pattern recognition, because results of the track propagation, matching and refitting are strongly depended on the quality of the reconstructed track (fraction of wrong associated hits, number of wrong reconstructed segments).

Tests for the evaluation of the pattern recognition packages are selected according to the physical program of the HERA-B experiment. The physical program is described in Chapter 1. The topics of the physical program made clear that the following set of tracks are important:

- lepton tracks from J/ψ decays (J/ψ prompt or B-meson decays), a high efficiency and good understanding of the ghost rate is needed,
- all tracks which originate from primary decays are important, because the resolution of the primary vertices depends on the number of associated tracks,
- decay tracks from B-decays are important, the efficiencies and ghost rates are important to calculate an efficiency for $J/\psi X$.

Decay tracks from long lived particles were not included in the official test program but they were checked as well.

The number of interactions per event is chosen to be one $J/\Psi \rightarrow \mu^+\mu^-$ event and two superimposed Poisson distributed inelastic events with the aim to represent the track multiplicity in the triggered data of 2000. But the performance is checked also for up to four superimposed interactions per event. The sample of simulated data consists of 60.000 minimum bias events and 100.000 prompt $J/\Psi \rightarrow \mu^+\mu^-$ events. All events were generated using the same carbon target wire "Inner 2".

For the detector simulation two scenarios are defined: generic and realistic, according to the measured performance during the run period in 2000. Table 4.1 summarizes the parameters. For the OTR hit preparation dead and noisy channels of the OTR were masked according to the run 14577, which belongs to the "Golden Minimum Bias" data taking period in 2000.

For the tests on data, the "Golden" minimum bias run 14577 is used. For J/ψ tracks a sample of preselected data is used. This sample contains about 2000 events with at least one J/ψ candidate per event.

Table 4.1: Parameters used for detector simulation.

	generic	performance of 2000
Hit resolution for OTR, μm	350	500
Hit resolution for ITR, μm	150	200
Hit efficiency for OTR, %	95	90
Hit efficiency for ITR, %	90	86
Dead strip simulation	–	according to the run 14577

4.4.1 Reference Quantities

For simulated data the following reference quantities are selected:

1. for MC:
   - reconstruction efficiencies of reference tracks,
   - clone and ghost rate,
   - residuals of track parameters (x, y, tx, ty),
   - number of hits used for the reconstruction of a track,
   - number of unused hits in the event (hits which are not used for the reconstruction of any tracks),
   - percentage of tracks that can be correctly tracked through the TC area,
   - percentage of correctly matched VDS-PC segments,
   - time consumption.

2. for data:

   - number of hits used for the reconstruction of a track,
   - number of unused hits in the event,
   - percentage of tracks that can be tracked through the TC area,
   - percentage of matched VDS-PC segments,
   - time consumption,
   - agreement with MC.

For evaluation purposes all simulated and reconstructed tracks are subdivided into several categories: a "reference set" of tracks, an "all set", an "extra set", clone and ghost tracks.

By definition, a track from *the all set of tracks* should intersect the sensitive regions of at least 5 layers (roughly 1 superlayer). A *reference track* should have a momentum greater than 1 GeV/c and intersect the sensitive regions of more than 17 layers (this number corresponds roughly to 3 traversed superlayers). Note, that the requirement of more than 17 traversed layers is simply an acceptance cut and does not imply the presence of more than 17 hits, since hit inefficiencies and track overlaps might reduce the number of hits considerably. Therefore, the obtained numbers for the reconstruction efficiency depends on the hit efficiencies of the detectors. All track sets are summarized below:

- *reference tracks* (particle momenta larger than 1 GeV/c, more than 17 layers in the PC area are crossed),
- *all tracks*, (more than 5 layers are crossed in the PC area),
- *physics tracks,*
  - *primary tracks,*
    - *all primaries*, more than 5 layers are crossed in the PC area,
    - *reference primaries*, more than 17 layers are crossed in the PC area and particle momenta larger than 1 GeV/c,
  - *lepton tracks from J/ψ decays,*
    - *all J/ψ-leptons*, more than 5 layers are crossed in the PC area,
    - *reference J/ψ-leptons*, more than 17 layers are crossed in the PC area and particle momentum large than 5 GeV/c.

In addition to these tracks the so-called *extra* set of tracks, containing short high-momentum and low-momentum tracks, was also considered.

A reconstructed track is *assigned* to a generated particle, if at least 70% (70% criteria [46]) of its hits have been caused by this particle. A generated particle is regarded as found, if it has been assigned to at least one reconstructed track. *Ghost* tracks are reconstructed tracks for which no simulated tracks were found. The *ghost rate* is normalized to all reconstructed tracks. *Clones* are reconstructed tracks for which a simulated track is found, but a better match exists (If one simulated track causes n tracks to be

reconstructed, the match with the highest number of hits agreeing is called "the right track", the n-1 other tracks are counted as clones. If the number of agreeing hits is equal, the track with better parameters is "the right track"). The clone rate is normalized to all reconstructed tracks.

4.4.2 MC Study Results

During comparison many efficiency studies were performed, the results obtained for the scenario one $J/\Psi \to \mu^+\mu^-$ event mixed with 2 superimposed inelastic events are summarized below in Table 4.2.

Table 4.2: Reconstruction efficiencies and clone/ghost rates obtained on simulated $J/\Psi \to \mu^+\mu^-$ events mixed with 2 superimposed inelastic events for CATS, RANGER and TEMA packages for realistic scenario.

	Efficiency (%)		
Set	CATS	RANGER	TEMA
Ref. J/Ψ	97.4	93.6	90.8
Ref. Prim.	96.2	91.5	87.4
Ref. Tracks	92.3	84.6	82.7
All Tracks	55.6	40.	44.8
Extra	33.3	13.	21.7
Clone	2.1	2.5	0.8
Ghost	14.	17.2	17.1
MC tracks per event	59	42	47

On average, the CATS efficiency is 97% for reference tracks coming from the target region. The efficiencies for the other types of tracks are smaller, which can be attributed to their average momenta being smaller than those of primary and J/ψ tracks.

The ghost rate is roughly 14%. It should be noted that the ghost rate at this level of reconstruction is uncritical because ghost tracks are very likely to be removed at the next steps, the magnet tracking or matching with VDS segments. The overall clone rate and the absolute number of ghost tracks is lower for CATS, on condition that CATS reconstructs many more soft tracks. Table 4.3 shows reconstruction efficiencies for all types of reference tracks for $J/\Psi \to \mu^+\mu^-$ events mixed with 5 superimposed inelastic events.

In order to understand the dependence of the track reconstruction performance on the track multiplicity, the reconstruction efficiency of reference tracks and the ghost level were measured with different numbers N of superimposed inelastic interactions exactly mixed. On average, the number of reconstructable tracks per event scales linearly with the number of exactly mixed interactions, rising from 40 tracks for one interaction up to 320 for eight. For this test, RANGER was taken as a reference. The results are summarized in Fig. 4.8.

Table 4.3: Reconstruction efficiencies and clone/ghost rates obtained on simulated $J/\Psi \rightarrow \mu^+\mu^-$ events mixed with 5 superimposed inelastic events for CATS, RANGER, TEMA packages for realistic scenario.

	Efficiencies (%)		
Set	CATS	RANGER	TEMA
Ref. J/Ψ	95.5	89.1	81.5
Ref. Prim.	93.1	87.7	77.1
Ref. Tracks	90.5	82.1	74.4
All Tracks	60.1	41.2	39.8
Extra	43.3	17.3	20.6
Clone	5.	4.8	1.8
Ghost	18.4	21.6	22.8
MC tracks per event	119	82	79

While the mean interaction rate was expected to result in four Poisson distributed superimposed interactions, the performance of CATS was investigated for up to 8 interactions. The reconstruction efficiency for reference tracks slowly decreases from about 93% to 78%, ghost rate grows from 6% to 23%. As can be seen, the efficiency and ghost level of CATS show the same trends as those of RANGER demonstrating the stability and robustness of CATS.

In order to estimate the accuracy of the track reconstruction algorithm, track residual distributions are investigated at two planes: $z = z_f$ and $z = z_e$, where z_f, z_e are the z-coordinates of the first and the last hits of the reconstructed track, respectively. The reliability of the track covariance matrix produced by the reconstruction algorithm is studied by investigating normalized residual distributions, using diagonal elements of the covariance matrix for normalization. By definition, the normalized residual (also called pull) of a track parameter, for instance x-coordinate, is

$$P(x) = \frac{x^{REC} - x^{MC}}{\sqrt{\Gamma_{xx}}},$$

where x^{REC} is the estimated value of x, x^{MC} the value taken from Monte Carlo truth, Γ_{xx} the corresponding diagonal element of the covariance matrix. Ideally, the distributions of pulls should be unbiased and have a Gaussian core of unity.

Table 4.4 presents values of pulls and residuals for four parameters x, y, t_x and t_y of properly reconstructed tracks and the mean length of the tracks given in the number of associated hits for all three algorithms.

The pulls in the OTR are typically wider than unity. As was mentioned in [25] wider pulls are caused by inevitably unresolved left/right ambiguities, hits picked up from other tracks, and a simplified treatment of multiple scattering. However, it should be mentioned, that this problem only affects the accuracy of track parameter estimates, leaving the track reconstruction efficiency untouched.

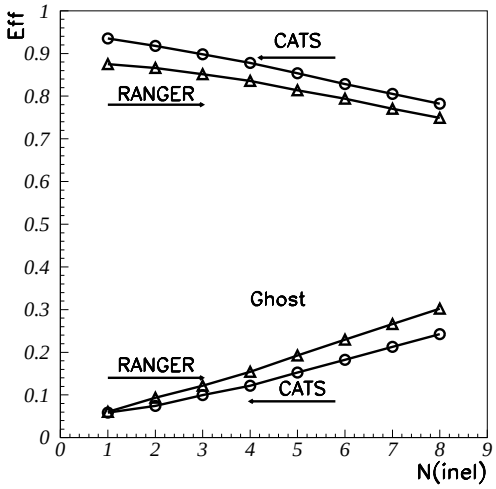

Figure 4.8: Reconstruction efficiency for reference tracks and ghost level versus the number of superimposed (exactly mixed) inelastic interactions

The efficiency of L/R ambiguity resolution in the OTR is investigated for three sets of tracks: lepton, primary and all reference tracks. The evaluation method was based on the comparison of the reconstructed sign of the drift radius $\widehat{q}$ with its true value q taken from simulated data. Only significant errors in the L/R sign determination are taken into account, i.e. those for which the residual ρ is

$$\rho = |\widehat{q} - q| \geq 3\sigma_0,$$

where σ_0 is the detector resolution. For each correctly reconstructed track (more than 70% of the hits belong to a certain simulated track) the fraction of L/R errors is calculated. The results are summarized in Table 4.5.

As can be seen, CATS provides the most accurate resolution of L/R ambiguities for all types of reference tracks.

A PC with dual 500 MHz CPU Pentium III processor was used to measure the time consumption of the algorithm. The mean CPU time needed for CATS to reconstruct an event with 2 mixed interactions was about 240 ms. The computing time dependence on the number of superimposed inelastic events for CATS and RANGER is shown in Fig. 4.9. For CATS, the CPU time consumption shows only a very moderate increase, corresponding to an almost constant time requirement per track. The main reasons for the observed computational superiority of CATS are

- the avoidance of combinatorial pile-up by hit clusterization in the OTR;
- the space-point based approach for track recognition performed by the cellular automaton;
- the fast algorithm for L/R ambiguity resolution;
- the optimized implementation of the Kalman filter.

Table 4.4: Resolutions, pulls P and mean length of reconstructed primary tracks.

	CATS		**RANGER**		**TEMA**	
Resolutions	OTR	ITR	OTR	ITR	OTR	ITR
x, μm	246	93	322	91	291	98
y, mm	3.7	1.4	5.0	1.4	4.1	1.4
t_x, mrad	0.62	0.24	0.71	0.24	0.76	0.26
t_y, mrad	4.73	1.79	6.96	1.79	5.39	1.87
Pulls						
$P(x)$	1.59	1.11	1.37	1.10	1.45	1.06
$P(y)$	1.52	0.98	1.25	1.11	1.81	1.16
$P(t_x)$	1.16	0.93	1.25	0.89	1.18	1.15
$P(t_y)$	1.53	0.99	1.39	1.15	1.92	1.23
Hits/track	31	23	26	21	31	21

Table 4.5: Fractions of wrong L/R assignment in correctly reconstructed tracks.

Algorithm	CATS	RANGER	TEMA
Ref. J/ψ, %	1.9	4.6	3.7
Ref. Prim., %	2.9	4.4	3.9
All Refset, %	3.3	5.1	4.3

Studies of J/Ψ reconstruction efficiency on simulated $J/\Psi \rightarrow \mu^+\mu^-$ events mixed with 2 superimposed inelastic events, have shown that CATS provides an about 10% higher efficiency for J/Ψ mesons than RANGER and 20% higher efficiency than TEMA with about the same mass resolution. CATS also has shown a higher efficiency for K^0_S signal, it finds about 20% more K^0_S than the other packages.

4.4.3 OTR/ITR-CATS on Real Data

For the efficiency studies on real data, several runs (14577, 16784, 17137) were reprocessed using the three different pattern recognition packages in the tracking. The result of these studies is that CATS finds 10-18% more J/Ψs than RANGER and TEMA, depending on the applied cuts. CATS also produces better signal to background ratios and significantly narrower J/Ψ-peaks. In additional CATS has demonstrated higher efficiency for K^0_S signal, it finds 20% more K^0_Ss than RANGER and TEMA. It can be seen that results obtained on MC and real data are in the good agreement.

Since June 2001 CATS is the default track recognition algorithm for the Pattern Tracker. It has been used to reprocess all data collected in 2000 and 2002/2003.

The relatively high efficiency of CATS for steep tracks crossing different sectors of the detector is especially useful for alignment procedures. In addition, the space-points produced by the package are used for the initial alignment of the OTR superlayers and cross-checks of the relative positions of ITR modules and OTR superlayers.

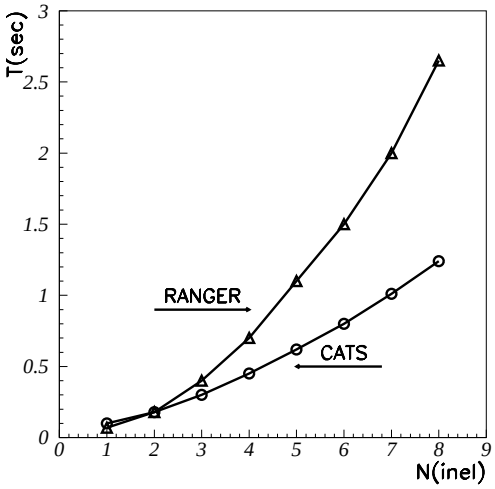

Figure 4.9: Mean computing time per event versus the number of superimposed (exactly mixed) inelastic interactions.

4.5 Conclusion

The package OTR/ITR-CATS was developed for the reconstruction of tracks in the Pattern Tracker of the HERA-B experiment. The reconstruction algorithm implemented in the package is based on a cellular automaton for track searching and the Kalman filter for track fitting. Comprehensive tests of the package have shown remarkably high reconstruction efficiency, good accuracy of track parameter estimates, a reasonable behavior of CPU time consumption and robustness of the algorithm with respect to large track multiplicities.

Chapter 5

Hit efficiency

This chapter is devoted to one of the most important characteristics of all tracking devices - the hit efficiency. A method was developed to measure the hit efficiency for the Inner Tracker system. In order to exclude inefficient channels from the efficiency determination a masking procedure was developed. The average efficiency for each single chamber of the Inner Tracker system was calculated. The measured efficiencies and masking information was used to achieve a realistic model of the ITR performance for MC simulation.

5.1 Introduction

A charged particle traversing the sensitive volume of one GEM-MSGC detector ionizes the gas and the amplified electrons are collected on the MSGC structure. A cluster produced by a minimum ionizing particle has an average width of 3 strips. The center of gravity of such a cluster is called a hit position and used for the track reconstruction. To identify bad areas in a chamber, clusters found by the online hit-preparation program are used to determine the functionality of all strips contributing to the clusters.

A strip is defined as *dead* if the number of times, when it is used in clusters is 20% below the average number. Another group of problematic strips is defined as *hot* channels. These channels contribute to clusters more often than the average.

The *hit efficiency* is defined as the probability to find a hit if a charged particle traverses the sensitive volume of the chamber. For the purpose of off-line reconstruction, the meaningful quantity is the real efficiency of a single chamber, i.e. including dead regions.

For a better understanding of the performance of Micro-Strip Gas Counters (MSGC) with Gas-Electron Multiplier (GEM), it is more interesting to study the *pure efficiency*, i.e. excluding dead channels from the consideration.

5.2 Masking Procedure

The *wiremap* is a distribution which contains the positions of all strips belonging to clusters. The *mean wiremap* is the wiremap normalized to the number of processed events and to the rate. The *occupancy* consists of the clusters' center of gravity positions normalized to the number of events. The example of an occupancy and a wiremap is shown

in Fig. 5.1. The overall shape is determined by the beam pipe cut-out and the radial decrease of particle density. At first glance occupancy and wiremap look almost the same, but the wiremap has several advantages: it allows to locate problematic channels more easily, which could not be used during clusterization, and it increases the accumulated statistics by a factor of about 3.

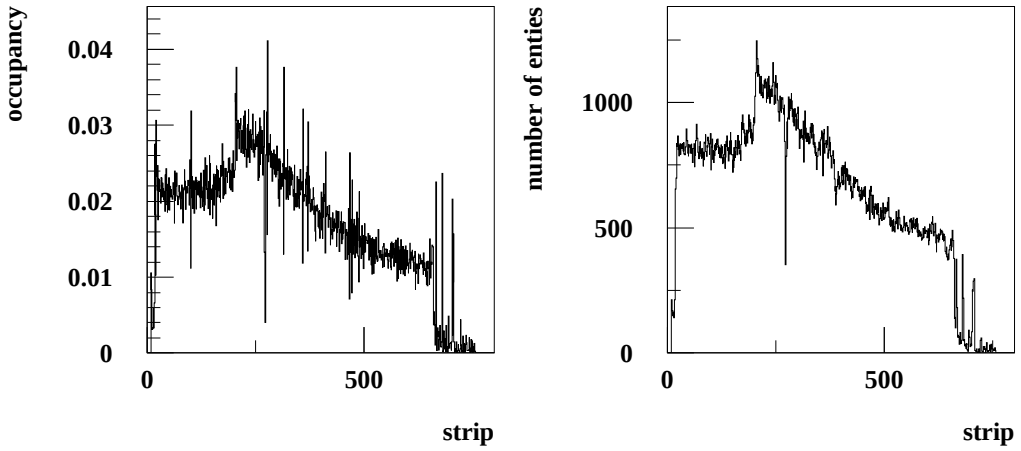

Figure 5.1: On the left, occupancy for chamber MS01++4. On the right, wiremap for chamber MS01++4.

The masking procedure is based on the assumption that the *average hit density* of a single chamber does not deviate too much from the *average hit density* of the station. The *average hit density* of the station is defined as the sum of the wiremaps of all chambers in one superlayer normalized to the number of events, the rate and the number of chambers in the station. We can subdivide the procedure into the following steps:

1. In order to find completely dead chambers, the average hit density of an investigated chamber μ_i is compared to the average hit density of the station μ_{sl}. The average hit density for the chamber i can be written as

$$\mu_i = \frac{1}{N} \sum_{k=1}^{768} n_{k,i} \tag{5.1}$$

and for the station

$$\mu_{sl} = \frac{1}{l * N} \sum_{j=1}^{l} \sum_{k=1}^{768} n_{k,j} \tag{5.2}$$

$n_{k,i}$ is the number of times charge is deposited on a strip k of a chamber i. The value l denotes the number of chambers in the particular station and N is the number of processed events. If the average hit density of a chamber is below 20% of the average hit density,

$$\mu_i \leq 0.20 * \mu_{sl}, \tag{5.3}$$

of the station all channels are marked as dead. In case it is above 140% all channels are marked as hot

$$\mu_i \geq 1.40 * \mu_{sl}. \tag{5.4}$$

All chambers which are not hot and dead are further considered at steps 2 and 3.

2. At the next step, the search for dead and hot PCBs[1] among the remaining chambers is done. A sketch showing the distribution of PCBs over the chamber is shown in Fig. 5.3. The hit densities for each single PCB are accumulated and three average hit densities of a station (for each PCB) are calculated. The hit density thresholds are optimized in order to take into account the shape of the wiremap:

   - low C_A^{low}=30%, high C_A^{high}=150 % for PCB A
   - low C_B^{low}=50%, high C_B^{high}=180 % for PCB B
   - low C_C^{low}=20%, high C_C^{high}=140 % for PCB C

   According to the following condition PCBs are marked as dead, hot and normal.

$$\mu_i^{PCB} \leq C_m^{low} * \mu_{station}^{PCB}, \tag{5.5}$$

$$\mu_i^{PCB} \geq C_m^{high} * \mu_{station}^{PCB}. \tag{5.6}$$

   The value m denotes the type of PCB: A, B or C.

3. Finally, single strips are considered. For each strip, the average number of hits is calculated. The average hit densities of the PCBs in similar positions in one station[2] are calculated and normalized to the number of strips (256 stips are connected to one PCB). If the hit density of the strip is below 20% or higher than 140% of the average hit density of this PCB then the strip is marked as dead respectively as hot.

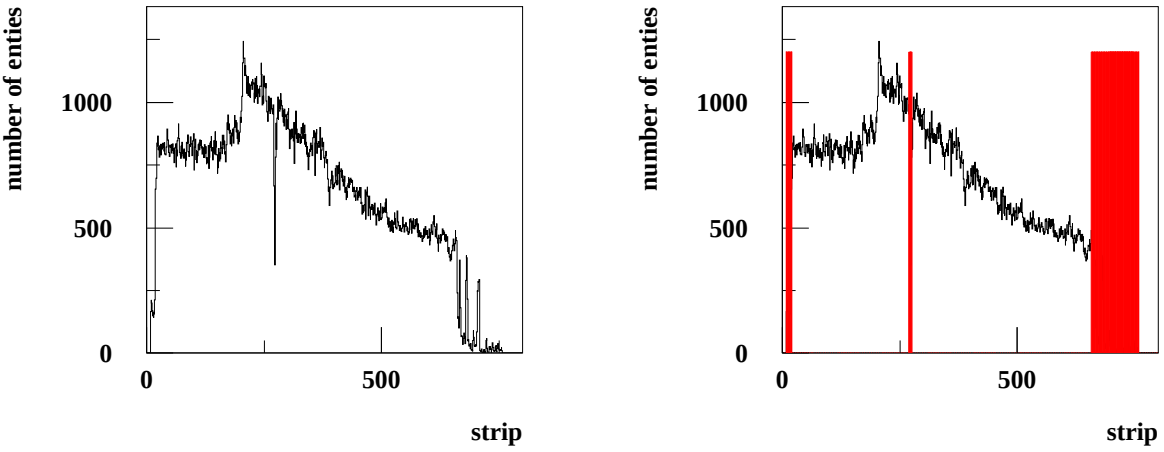

Figure 5.2: On the left, wiremap for chamber MS01++4. On the right, wiremap with dark color masked strips are shown for chamber MS01++4.

[1]To read out the 752 channels of one Inner Tracker chamber, six Helix chips are used. Two chips are mounted on one common Printed Circuit Board (PCB).

[2]The mean wiremaps of a station of PCB is defined as wiremap accumulated by PCBs in all chambers in the station.

In order to produce masks for all chambers in one run, a sample of approximately 10.000 events is needed. Only runs without problems were considered. For some runs the stability of the Inner Tracker high voltage during data taking was checked. Masks have been produced for most of the minimum bias and triggered runs in 2002 - 2003.

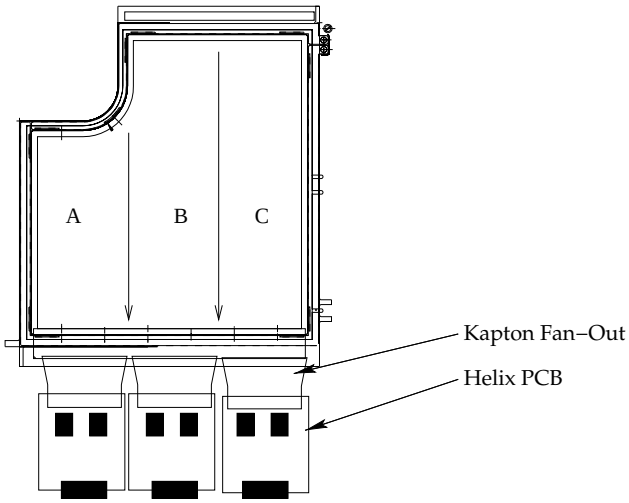

Figure 5.3: Sketch of an ITR chamber indicating the distribution of PCBs over the chamber.

The mean number of masked strips in runs of 2002 are shown in table 5.1. The time period between the run 20096[3] and 21072 is approximately four months. Fig. 5.2 shows on the right the mask produced with the described masking procedure overlaid on top of the associated wiremap.

Table 5.1: Percentage of masked channels in the inner tracker system. The first and the last eight not connected strips are not counted (dead chambers are included).

Station	run 20096	run 21072
MS01, %	7.1	8.8
MS10, %	50,35	53.68
MS11, %	16.54	16.87
MS12, %	14.2	16.62
MS13, %	60.28	61.30
MS14, %	—	18.8
MS15, %	—	57.6

The obtained masks are stored in the Data Base.

During running in 2002-2003 several chambers in the Inner Tracker system have shown a rather bad performance. A typical wiremap for one of the problematic chambers is shown in Fig. 5.4.

It was found that the resistance between neighboring strips on the Kapton Fanin which connects MSGC and Frontend electronics was too low. It seems that the reason for

[3]In run 20096 MS14, MS15 were not available.

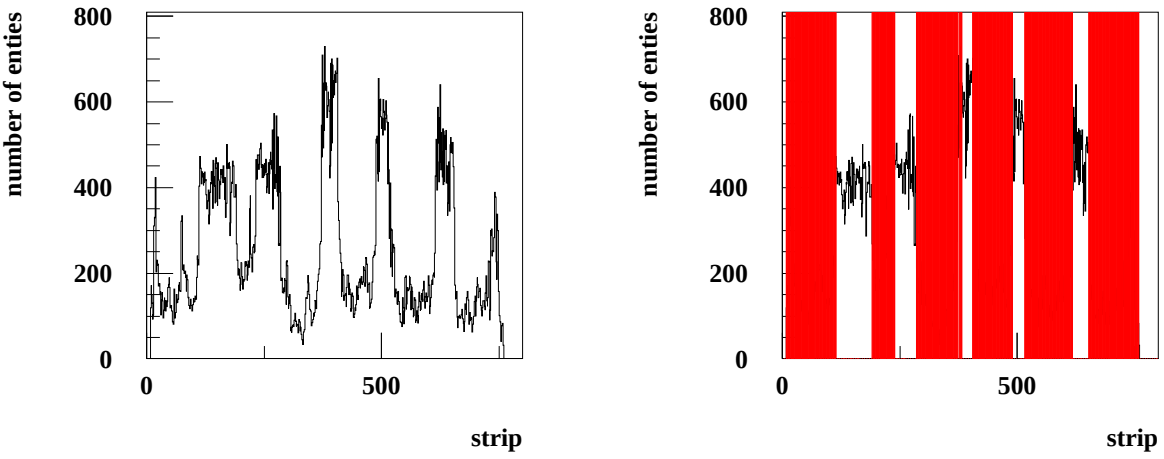

Figure 5.4: On the left, a wiremap for chamber MS10++4. On the right, a wiremap with masked strips shown in dark color for chamber MS10++4.

this behavior is due to the glue or the glueing procedure, used for bonding the chamber to the PCB [16]. Fig. 5.4 shows a wiremap and the mask for an affected chamber. The distribution on Fig. 5.4 at the right shows the masked channels (dark) overlaid on top of the wiremap of the chamber. These masked regions have to be excluded for the determination of the pure efficiency.

5.3 Track Selection

The track selection is essential for the efficiency estimation, because not properly reconstructed tracks are the main source of bias for the final efficiency numbers. In order to suppress this effect the selection cuts have been adjusted by Monte Carlo simulation. The final selection criteria are described below.

Station MS01

The first superlayer of the Inner Tracker system is MS01, situated just behind the silicon detector. For the efficiency estimation in this station tracks reconstructed in the silicon detector are used. There are several reasons which motivate this choice:

1. no standalone tracking inside MS01 is possible because only four layers are available,
2. the distance between the silicon detector and MS01 is only a few centimeters and the resolution of the VDS is nearly a factor 10 better than that of the ITR.

In order to reduce the number of wrongly reconstructed segments, which otherwise could introduce a bias in the efficiency measurement, the following requirements are applied to the VDS segments used:

- at least 6 hits in the VDS detector,
- track fit χ^2 probability larger than 0.05,

- at least 2 confirming hits in MS01 (out of 3 possible).

The algorithm looks for confirmation hits within a search window around the predicted impact point calculated using the parameters extrapolated from the last point of the segment to the investigated plane. The size of the search window is chosen according to the extrapolated covariance matrix of the segment.

PC region

The next part of the ITR is the "PC" region situated behind the magnet and in front of the RICH vessel. It consists of four superlayers (MS10, MS11, MS12, MS13). In this region the standard pattern recognition program is used. Hits of the investigated layer are excluded for the pattern recognition program, in order to avoid a bias in the efficiency calculation. Tracks reconstructed in the ITR have been used only if they fulfill the following requirements:

- at least 14 hits in the PC region of the ITR,
- at least three crossed superlayers in the "PC" region,
- the track has to consist of matched ITR and VDS segments,
- track fit χ^2 probability after refit larger than 0.05,
- momentum less than 100 GeV/c.

TC region

The last part of the ITR is situated in the "TC" region (between RICH and ECAL). It consists of two superlayers (MS14, MS15). Only 24 chambers of the installed 48 chambers are read out. No standalone pattern recognition in these chambers is available. The used tracks should meet the following requirements:

- at least 11 hits in the ITR are used for the track reconstruction (excluding TC),
- at least 4 confirming[4] hits in stations MS14 and MS15,
- the track segment reconstructed in the main tracker should have a matched VDS segment,
- track fit χ^2 probability after refit larger than 0.05,
- momentum less than 100 GeV/c.

For each selected track it is required that it has to traverse the sensitive volume of the investigated chamber. The hit is defined as *found* if a cluster is found in a 3σ region around the track parameter u extrapolated to the z plane of the investigated chamber, u defined as $u = x * cos\alpha + y * cos\alpha$, where α is the rotation angle of the chamber. Sigma is chosen equal to the expected error of the track parameter u obtained via extrapolation of the track's covariance matrix to the z plane of the chamber.

[4]The confirmation procedure is implemented in the same way as for MS01 superlayer.

5.4 Efficiency of the Superlayer MS01

The most stable results were shown by chambers in station MS01. The station contains 16 chambers in four layers, which use the old Helix chips of version 2.1 which have not been replaced during the shutdown in 2000-2002.

The efficiency of the chambers and the number of masked strips have been checked for a running period of 6 weeks. For each run a sample of 50.000 events was considered and a new mask was created.

The main factor which influenced the measured efficiency is some specific feature in the Inner Tracker steering program. In case of sparks or cathode shorts the GEM voltage setting of one chamber or a group of chambers is temporarily reduced to lower values. This causes a lower efficiency of this group of chambers. Another possible bias could come from ghost tracks produced by the VDS track reconstruction program. This is at a negligible level with the applied cuts on the number of used VDS hits and the ITR confirmation requirement.

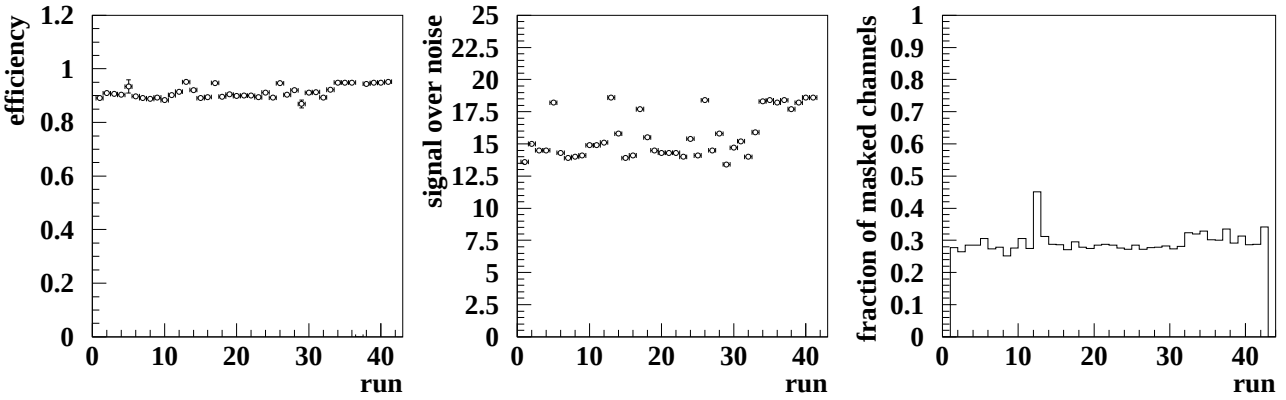

Figure 5.5: On the left, efficiency vs run for the chamber MS01 ++ 1. In the middle, signal over noise vs run for chamber MS01 ++ 1. On the right, fraction of masked channels vs run for chamber MS01 ++ 1.

The behavior of the efficiency with time for one of the chambers in MS01 is shown in Fig. 5.5 on the left. The development in time of the signal over noise distribution for the hits used in the efficiency calculation is shown in the middle plot. Fig. 5.6 shows that a strong correlation exists between signal over noise and efficiency.

Runs with higher efficiency or better signal over noise ratio (S/N) correspond to minimum bias data taking while the runs taken with dilepton trigger (most of the runs) show a slightly lower efficiency. Such a behavior can be explained by a read-out instability observed in triggered runs.

The stability of the number of masked channels for this particular chamber is shown on the right plot in Fig. 5.5. As can be seen the distribution is flat and only in a few runs more channels were masked. The deviation is in the order of a few percent. No indication of performance degradation (for example, increase of the number of masked channels or decreasing efficiency) can be observed.

The mean efficiencies for all chambers in MS01 are shown in Fig 5.8. As can be seen 80% of all chambers have efficiencies well above 90% with a standard deviation of the

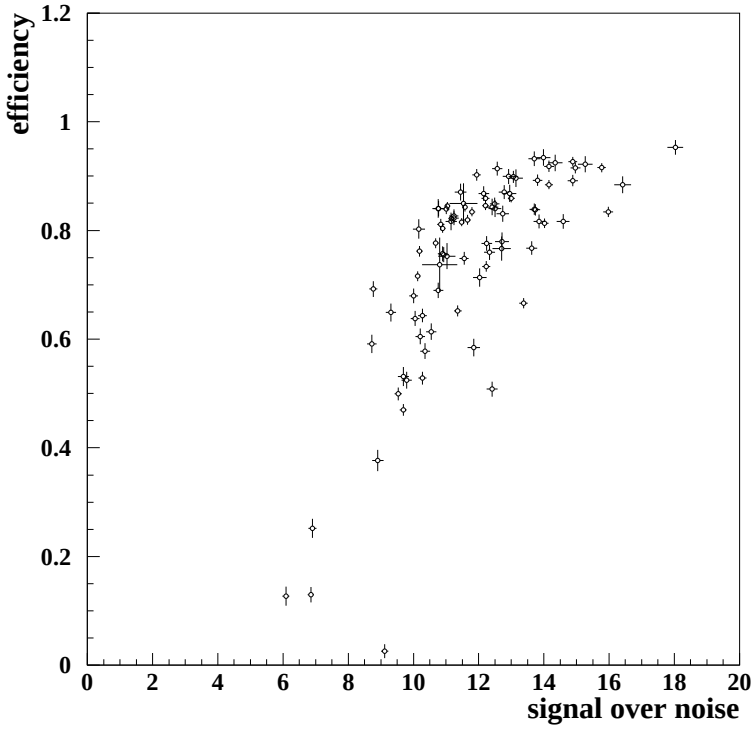

Figure 5.6: Correlation of measured efficiency versus signal over noise for the run 21056 for chambers of the PC region. Statistical errors are shown as error bars.

order of 2-3%.

The "real" efficiency strongly depends on the number of masked strips in the chambers. Figure 5.7 shows efficiencies for chambers of MS01 for the run 20794 with and without mask.

To achieve the shown efficiency level the GEM voltages have been adjusted in 2000 and 2002, in order to compensate gain variations from the GEM foils. Further increase of the GEM voltage parameters causes an operational instability without further increase in efficiency.

5.5 Efficiency of the PC Superlayers

There are four ITR superlayers in the PC region, they consist of 96 chambers organaized in 24 layers. The first and last superlayers consist of eight layers each. The two superlayers in between have only four layers each.

In order to avoid the bias which can appear if the pattern recognition program uses hits of the investigated chamber, a special version of the program was developed. Each event is reconstructed 24 times and every layer is excluded once from the reconstruction, in the excluded layer the efficiency estimation for all four chambers in the excluded layer is done. The parameters and covariance matrices of the nearest end-points of segments are extrapolated to the investigated z plane.

For the analysis a sample of 30.000 - 50.000 events is used for each run. For each run a new mask is produced. The main contribution to the number of masked channels comes

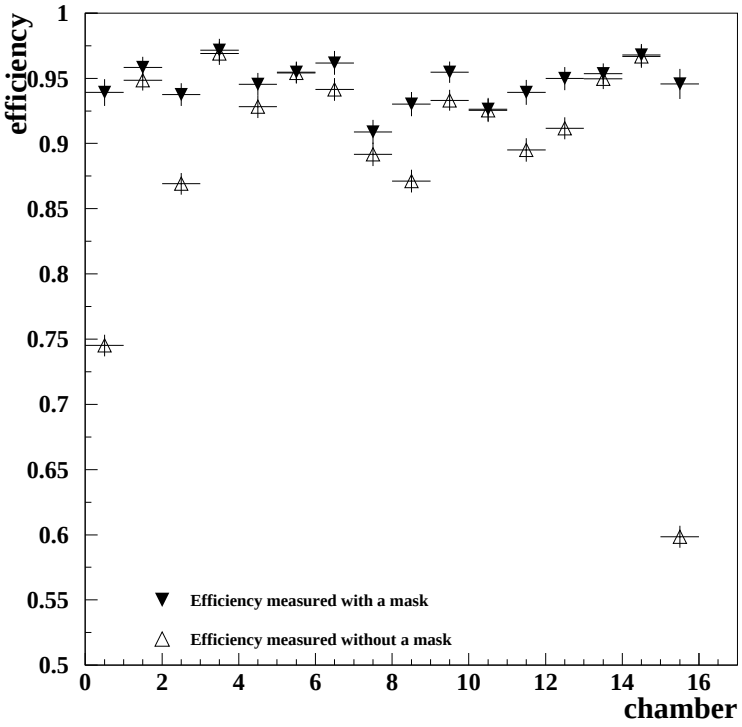

Figure 5.7: Efficiencies for all chambers of the superlayer MS01 for the run 20794. Efficiencies measured with help of mask are shown with filled triangles and with transparent triangles efficiencies measured without applying any masks. Statistical errors are shown as error bars.

from superlayers MS10 and MS13 (up to 60%).

As an example, the efficiency, S/N and number of masked channels over time are shown in Fig. 5.9 for one of the relatively good chambers, MS10 +- 2. Some spikes are seen in the distribution of masked channels, they are caused by low voltage problems for half of the superlayer.

Drops of the high voltage in a group of chambers and problems caused by low voltage power supplies lead to the effect that even for properly working chambers it was not always possible to calculate the efficiency with sufficient statistic. In some areas the reconstruction program was not able to find enough hits in order to reconstruct segments.

Figure 5.10 shows pure efficiencies for all chambers of PC superlayers. In the range from 0 to 31, chambers of station MS10 are placed, the range from 32 to 63 corresponds to the superlayers MS11 and MS12 and the rest are chambers of MS13. One can see that the chambers in MS10 and MS13 show rather low efficiencies and large variations. Superlayers MS10 and MS13 have approximately 40% chambers with rather low efficiencies and large variations, this group mainly consist of chambers with only 10-20% of working channels. Another influence on the efficiency is due to non perfect masks. The non perfect masks can be produced for the chambers with rather low number of working channels (only 10-20%) because it is difficult to distinguish between working and dead channels. In addition, some of these channels work only sporadically.

With the help of the obtained numbers, a GEM voltage tuning was performed in order to increase the efficiency of those chambers showing low efficiency. In some chambers the efficiency could be increased (in the order of 10%). Figure 5.11 shows the raise of the

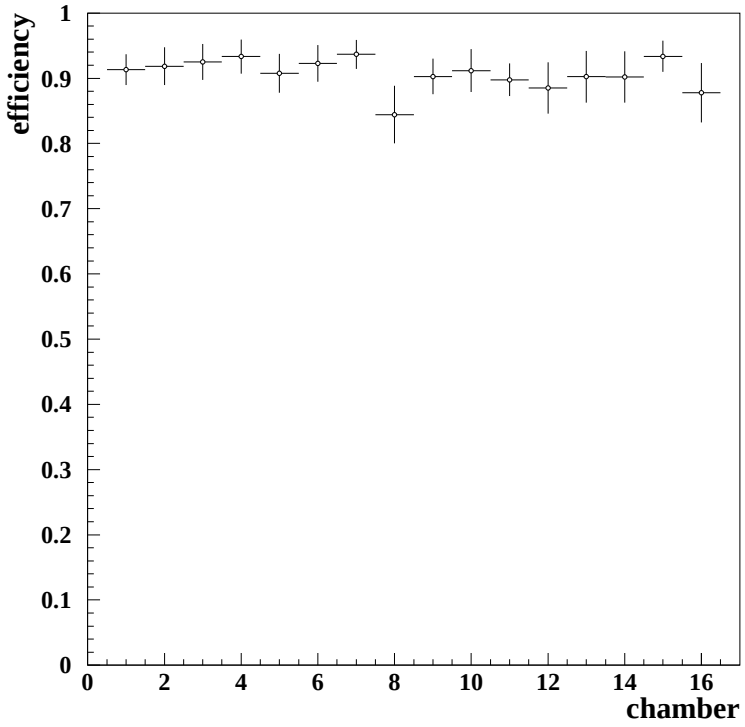

Figure 5.8: Mean efficiency distribution for the MS01 superlayer. Standard deviations are shown as error bars.

efficiency after GEM voltage increase for the chamber MS10 ++ 4. Approximately 80% of the chambers did not show any change in the efficiency after a tuning of the GEM voltage, one of these chambers is shown in Fig. 5.12. For approximately 5% of them the increased voltage affected the operation stability. For those chambers the voltage was set back to the original value.

5.6 Efficiency of the TC Superlayers

The TC area contains 2 superlayers with 6 layers each (MS14, MS15). Only three layers in each superlayer are read out. The chambers are installed in such a way that in each station a measurement in $0^0, +5^0, -5^0$ layers is provided. They are foreseen for trigger purposes and were first installed in 2001.

In the current setup the number of possible measurements, for the pattern recognition in TC superlayers, is limited by three measurements per superlayer, this caused the decision not to extend the pattern recognition program to perform standalone reconstruction in the TC chambers. To measure the efficiency in TC, tracks reconstructed in the PC region of the tracker are used. This leads to the effect that the efficiency estimation depends on the quality of the reconstruction in the PC region of the ITR because mainly tracks reconstructed in this region are in the acceptance of the TC chambers. In order to avoid ghost and badly reconstructed tracks confirming hits in TC chambers are required.

The search window, is defined with the help of the extrapolated covariance matrix with additional corrections to compensate the remaining misalignment. The misalignment can be expected because alignment of the TC chambers is based on the tracks reconstructed

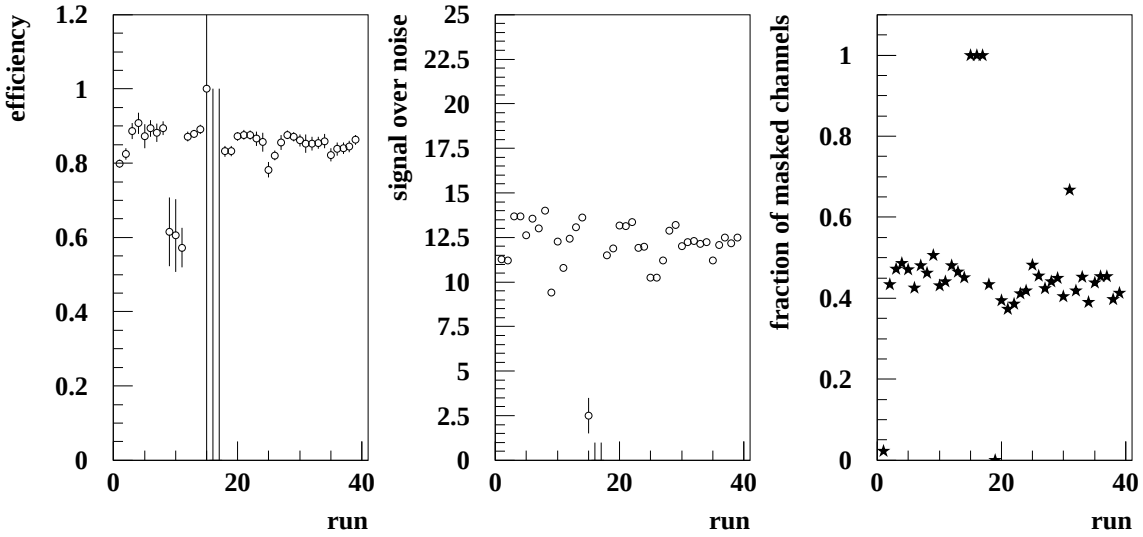

Figure 5.9: From left to right for the chamber MS10-+2: efficiency vs run number, signal over noise vs run number, fraction of masked channels vs run number. For the efficiency plot statistical errors are shown.

in the PC region and extrapolated over a rather large distance ($\approx 4m$). For this refining some additional fitting procedure is needed. In the first iteration, the mean position $\bar{u}$ of the residual peak is calculated and only hits which fulfilled the following requirement

$$|u_{extrapol} - u_{hit} - \bar{u}| < 3\sigma$$

are counted as efficient hits, σ - size of a search window and u_{hit} - measured hit position.

In each run a sample of 50.000 events corresponding to the period of stable operation (background and interaction rate) is used.

The obtained numbers are shown in Fig. 5.13. The left part of the plot corresponds to the chambers in station MS14 and the right to the chambers in MS15. The efficiency of MS14 is about 90% and significantly better compared with MS15. Four chambers of MS15 were switched off at that time period and two others showed efficiencies below 20%. The variation of efficiencies for the proper working chambers are about 5%. The main contribution to the inefficiency comes from hardware problems mentioned above and not perfect masking for some chambers[5] MS15 is equipped with several chambers which failed to fulfill the requirements of the pre-installation tests, due to a lack of good chambers these bad chambers had to be used.

The chambers of TC superlayers were foreseen to be used for purposes of SLT and FLT triggers. To achieve a performance necessary for these purposes further GEM voltage adjustments and the replacement of not working chambers would be needed.

[5]For some particular chambers it was not always clear whether the chamber is dead or not.

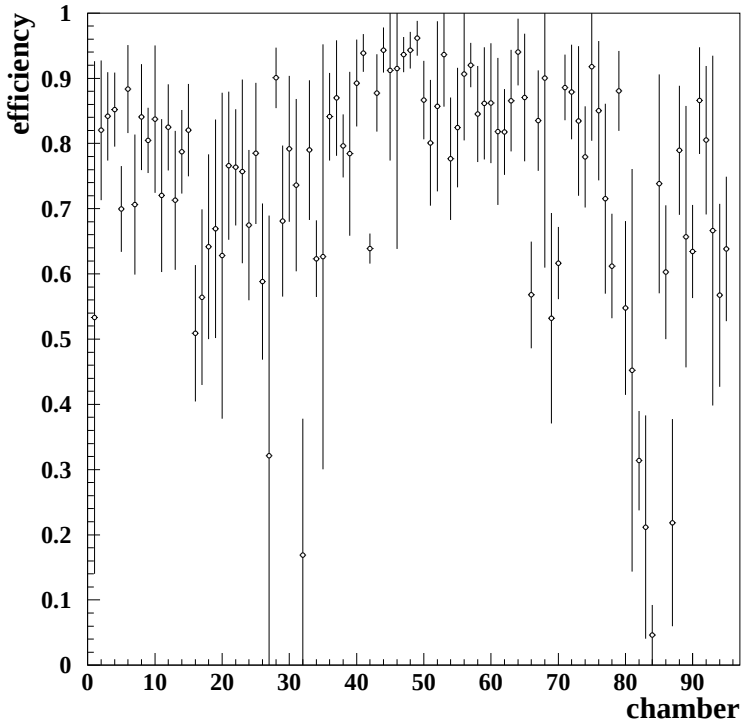

Figure 5.10: Mean efficiency distribution for the PC superlayers. Standard deviations are shown as error bars.

5.7 Test of the Algorithm with Monte Carlo

In order to estimate systematic errors and to define the accuracy of the hit efficiency measurement algorithm a special tool for Monte Carlo data tuning was used. This tool allows to apply efficiencies measured on MC data simulation. For the tests, the following mean efficiencies were used:

- 90% for chambers of the MS01 ,
- 80 % for chambers of the PC region,
- 80 % for chambers of the TC region.

Hits in the Inner Tracker chambers are produced according to the applied mean efficiencies. Neither global nor local misalignments for the ITR are applied.

On MC the same algorithm for hit efficiency measurement is used as on real data. The selected sample of MC data contains 20.000 events and allows to achieve approximately 50.000 entries for each of MS01 chambers and 4.000 measurements for each of PC and TC chambers. The obtained results are shown in Fig. 5.14. There are three plots which illustrate the obtained efficiencies for MS01 superlayer, PC and TC area. The efficiencies are constant for MS01 within about 1% and compatible with the applied efficiencies. In the PC and TC chambers a deviation of about 2% are measured. These differences can be explained by the limited statistic. The obtained efficiency numbers are summarized in Table 5.2.

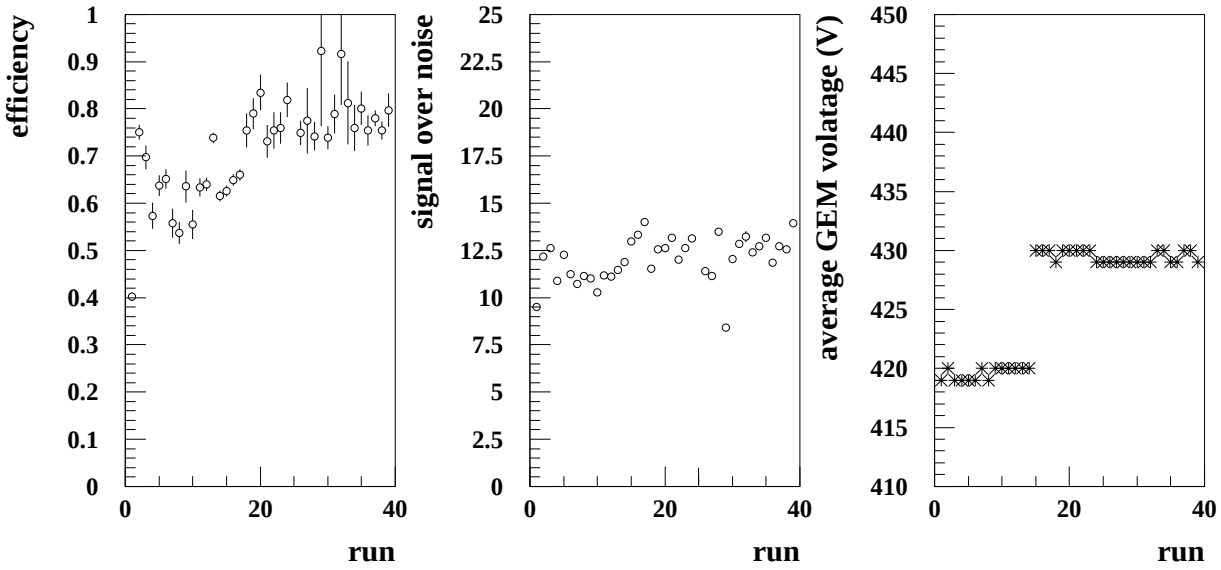

Figure 5.11: From the left to the right for the chamber MS10 ++ 4: efficiency vs run, signal over noise vs run, average GEM voltage vs run.

In order to check if the algorithm is able to deal with the ITR detector performances of 2002, with the large number of dead regions and observed low efficiency in PC region, a "realistic scenario" is applied:

1. for a particular run masks are produced and efficiencies for all chambers are calculated,
2. MIMPs[6] which are situated in the masked regions are discarded,
3. hits are produced from the MIMPs with a probability equal to the efficiencies measured on data for each chamber.

After applying efficiencies and masks, the standard routine for efficiency estimation is used. The obtained numbers are in agreement within about 2% with the efficiencies applied during simulation.

This shows that the pattern recognition program and the routine for efficiency estimation are robust enough to handle the real data and able to deliver reliable results.

	MS01	PC	TC
hit efficiency, %	89.98	81.72	80.01
efficiency variation, %	0.37	0.83	0.69
statistical error of efficiency, %	2.2	5.03	4.78

Table 5.2: Mean efficiencies, efficiency variations and statistical errors obtained on Monte Carlo data with realistic settings.

[6]Monte Carlo Impact Point. The point in space where the sensitive volume of the detector is crossed by a particle.

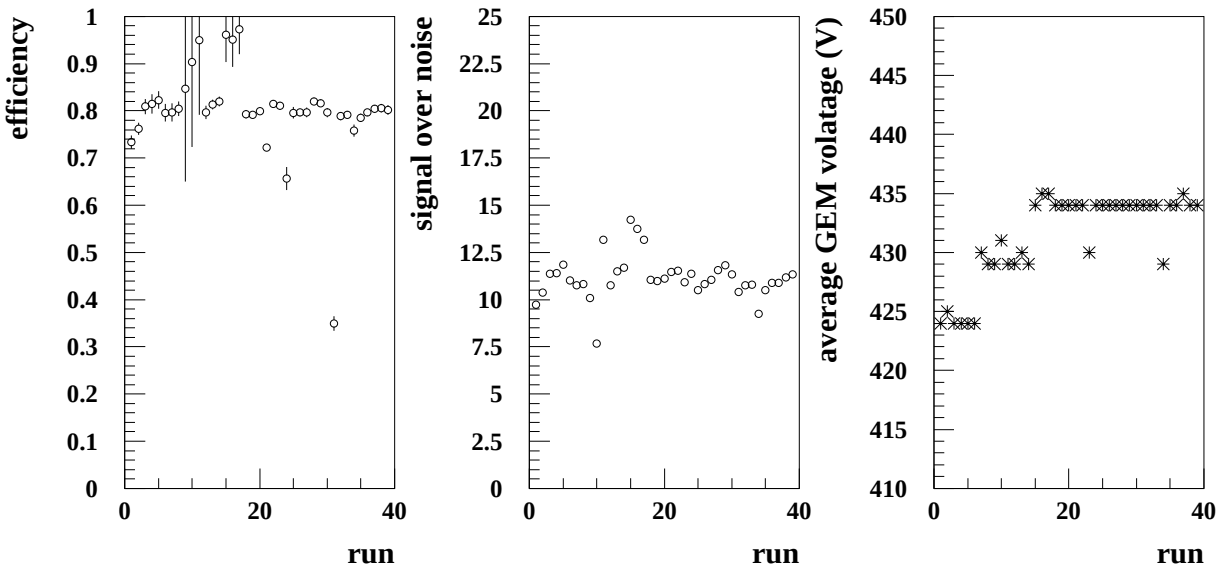

Figure 5.12: From the left to the right for the chamber MS12 – 1: efficiency vs run, signal over noise vs run, average GEM voltage vs run.

5.8 Summary

A method to measure the efficiency in all chambers of the Inner Tracker is described. This method has been applied to real and simulated data. Possible sources of bias to the estimated efficiency numbers have been investigated and found to be small. The only problem not accounted completely for is the bias introduced by dead strips remaining after masking. It can be seen from the large efficiency deviation for chambers with a very large number of non working channels.

The measured average efficiencies for chambers which were not re-equipped during the shutdown in 2001 vary between 90% and 95%. For chambers equipped with the new version of Helix the efficiency is between 50% and 90%. These numbers are significantly below the expected efficiency of 95% (this low efficiency seriously affects the track reconstruction efficiency of the Inner Tracker system). In principle the hit efficiency of several chambers can be improved by adjusting GEM voltages. However this is limited by the required operational stability of those chambers.

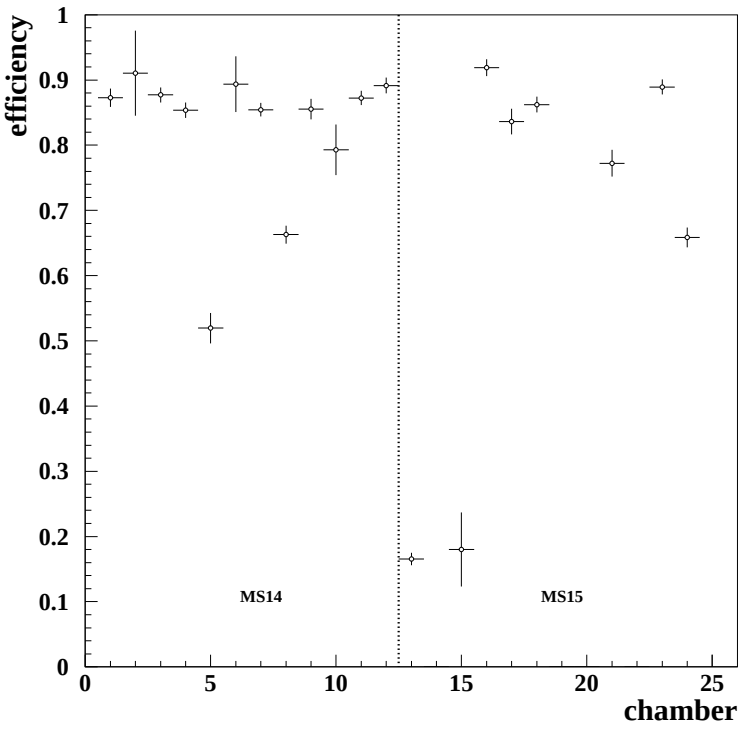

Figure 5.13: Mean efficiency distribution for the TC superlayers. Standard deviations are shown as error bars.

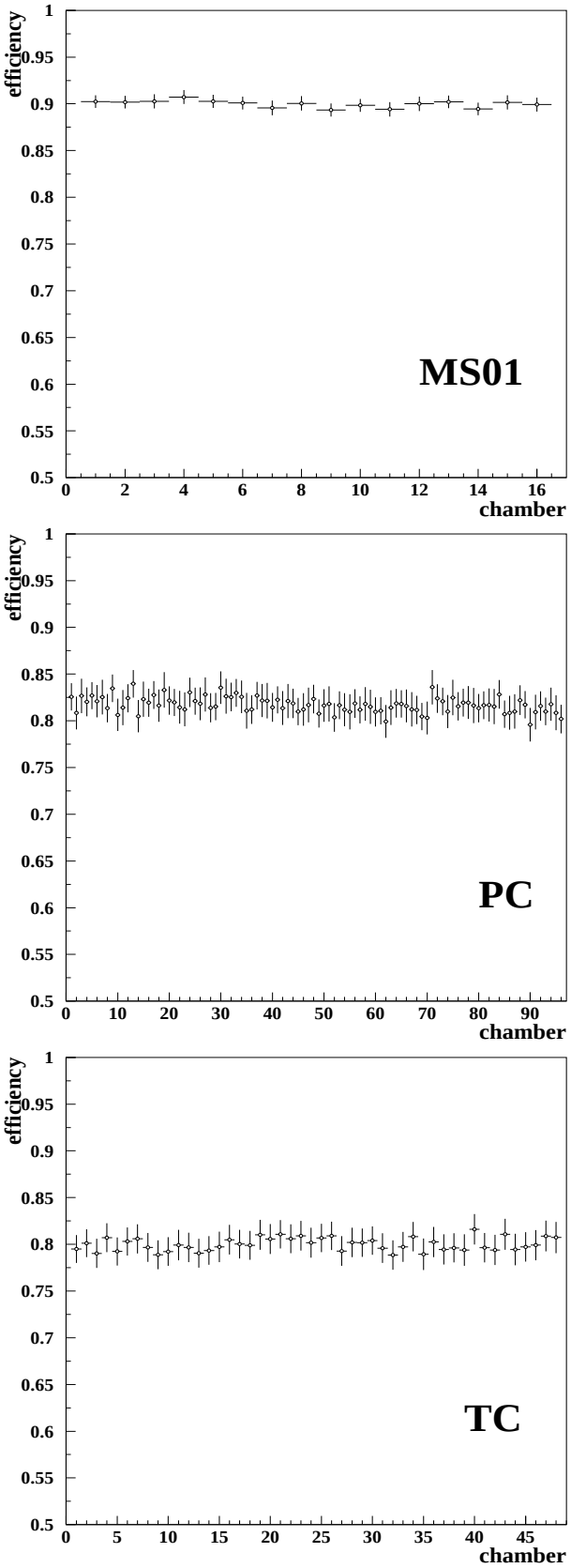

Figure 5.14: Hit efficiencies distribution obtained with Monte Carlo data for chambers of the Inner Tracker in the MS01 station, PC and TC area. Statistical errors are shown as error bars.

Chapter 6

V_0 Inclusive Production Cross Sections

Neutral strangeness production is an important probe for the study of fragmentation processes. Two-body decays $K^0_S \rightarrow \pi^+\pi^-$, $\Lambda \rightarrow p\pi^-$, $\bar{\Lambda} \rightarrow \bar{p}\pi^+$ can easily be identified due to abundant production, large branching ratios and long lifetime. These particles are labeled as 'V_0 decays'. The tracks of the decay products look like the letter "V" on bubble chamber photos when they were first discovered.

In this chapter a measurement of the V_0 production cross section of HERA-B is presented. The cross sections per nucleus are transformed to cross sections per nucleon and compared to previous measurements. The analysis is performed with the minimum bias data taken in December 2002 with three different target materials (C,Ti and W).

6.1 Monte Carlo Generation

The main goal of the simulation is to study the behavior of the HERA-B detector and to obtain the acceptance correction function. The generation of Monte Carlo (MC) events is done in two steps: first, particles produced in the primary interactions are generated and then the particles are propagated through the simulated detector.

PYTHIA (version 5.7) and FRITIOF (version 7.02) [50, 48] are the generators used at HERA-B to simulate events. PYTHIA internally makes use of the jet fragmentation utilities of the JETSET [51] package. The PYTHIA package simulates the collisions of nucleons (protons and neutrons), nuclear effects are not covered. After the simulation of the primary interaction the remaining energy is passed into the FRITIOF simulation package. FRITIOF is used for simulating nuclear effects.

HBGEAN [52] is the package used in HERA-B for detector simulation, it is a modified version of the GEANT [49] package. At this step of the simulation all geometrical features and materials of detector components of HERA-B are taken into account.

All particles produced by PYTHIA and FRITIOF are passed into HBGEAN and propagated through the simulated detector. All traced particles are leaving Monte Carlo Impact Points (MIMP) in the sensitive volumes of the detector (see Chapter 5). Energy loss and multiple scattering are taken into account at this step according to the initial particle momenta. All important information is stored in ARTE tables: MIMP table for MIMPs, MTRA (MC tracks) table for generated particles and MVER (MC vertices)

table for vertices. All these tables are linked with each other in order to provide easy navigation.

Up to this point no information about efficiencies and resolutions of detector components are taken into account. The information at this step can be treated as MC *truth*.

Simulated information is then digitized in a format so that it can be treated by the reconstruction program in the same way as real data. At this stage realistic detector performance can be simulated by applying efficiencies and dead channel masks. The detector resolution is simulated by smearing the hit positions according to the resolution measured on data.

To extract resolution and efficiencies of the Inner Tracker from Monte Carlo simulation, several runs were selected (one run per minimum bias data taking period) and the efficiencies and masks are produced with the procedure discussed in Chapter 5.

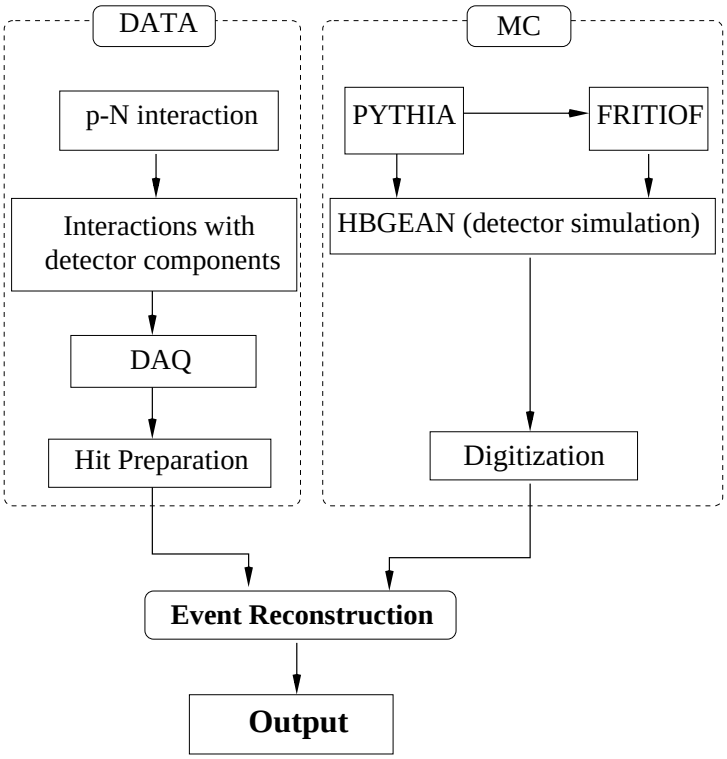

Figure 6.1: Schematic overview over data taking and simulation chains. The picture is based on [54]

After digitization all tables (HITB, HITC (hits in ECAL) etc) are filled. They are identical for MC and data, the identity makes it possible to treat data and MC in the same way (to use the same reconstruction packages in both cases). Figure 6.1 shows the path of data and MC in HERA-B.

6.2 Event Reconstruction

For the offline and online event reconstruction the same software framework ARTE (Analysis and Reconstruction Tool) [53] is used. This framework contains several packages responsible for cluster finding, pattern recognition, track matching etc.

The algorithm starts with hit preparation and filling the tables HITB, HITC etc.

At the next step standalone reconstruction in subdetectors and track finding starts. For the track finding in the main tracker system the OTR/ITR CATS package is used (see Chapter 4), and for pattern recognition in the Silicon detector a similar algorithm is utilized. The obtained clusters and segments are filled into the corresponding tables i.e. RSEG (reconstructed segments), RCCL (reconstructed ECAL clusters [17]), RHIT (reconstructed hits).

After the standalone reconstruction is completed for all subdetectors, the information is combined to complete tracks by the package MARPLE [22] and stored in the table RTRA (Reconstructed TRAcks). Only tracks produced by matched VDS and ITR/OTR segments are used for this analysis.

For the secondary and primary vertex finding GROVER (Generic Reconstruction Of VERtices) [23] package is used. The package also includes a target wire following algorithm for wire position refining. All vertices found are filled into the RVER (Reconstructed VERtex) table.

All tables listed are linked with each other and for example it is possible to find out which hits are used to reconstruct a segment or which hits are used in an ECAL cluster.

The event reconstruction chain is identical for MC and data and differs only in the step of the hit preparation.

6.3 K^0_S, Λ, $\bar{\Lambda}$ Selection

The selection criteria are always a crucial point in an analysis chain. In order to select appropriate cuts an optimization procedure was based on signal events from Monte Carlo and background from data. In this section, the optimization procedure is explained and the chosen cuts are presented.

6.3.1 Event Selection

In order to provide a fast event selection and rejection of nearly empty events the algorithm starts with the following criteria:

1. an event should contain at least two tracks which are not marked as clones by the clone removal algorithm [47],

2. at least one primary vertex consisting of more than three tracks or VDS segments should be reconstructed in the event.

The RTRA table contains all possible combinations of track segments, this leads to the fact that track segments can be used more than once. However, for the analysis purposes it is important to have a sample of tracks with a low number of clones (see Chapter 4). Therefore a standard procedure for clone removal was developed, based on the number of hits used in the track and the χ^2 of the track. The performance of the algorithm was adjusted with the help of a K^0_S reference data set (details about tests and the algorithm can be found in [47]).

6.3.2 Selection Cuts

To provide a fast background rejection the following cuts are used:

- Tracks which do not have VDS or Main Tracker segments are rejected by the cut on the number of hits used in tracks from the tracking detectors. The distribution of hits used for reconstruction of track segments in the VDS and Main Tracker obtained on data are shown in Fig. 6.2.

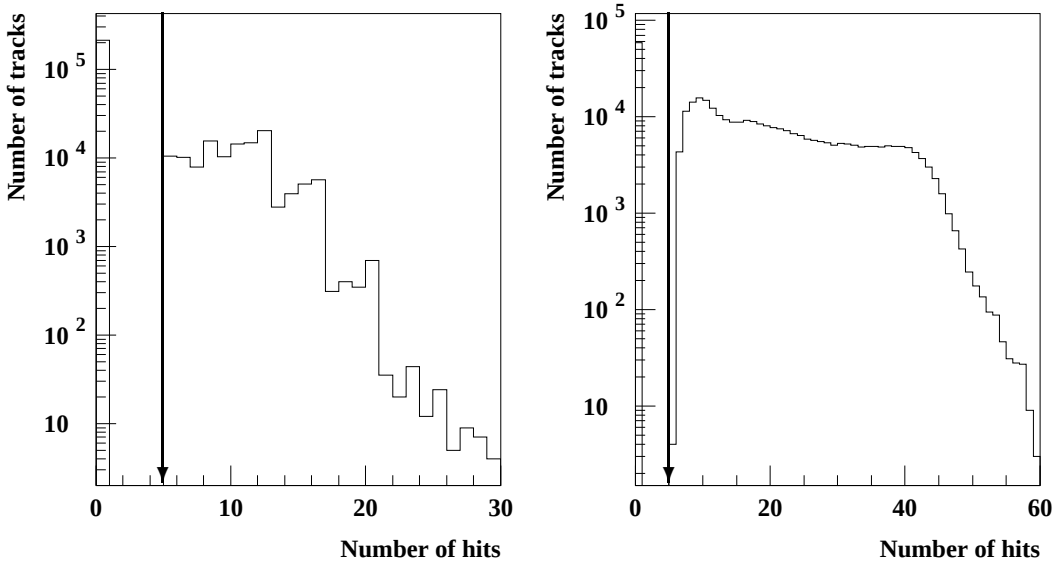

Figure 6.2: On the left, number of hits used in the Silicon detector for the track segment reconstruction. On the right, number of hits used in the Main tracker (ITR+OTR) for the track segment reconstruction. The chosen cut values are indicated by the vertical arrows.

- The next cut is based on the Distance of Closest Approach (DCA) between two V_0 tracks. The idea of the DCA cut is to reject tracks which are far from each other to speed up the selection algorithm.

- Cut on the vertex impact parameter. This cut selects the best primary vertex.

These three cuts can be understood as a soft preselection in order to reduce the amount of data to be further processed.

The main cuts for extraction of V_0 signals are DCA, impact parameter and flight path cuts. In order to optimize these cuts studies on MC and data are performed. Efficiencies versus applied cut distributions are shown in Fig. 6.3 for K^0_S. The plots at the top show the behavior of signal and background versus the applied cut. Signals are taken from generated MC and the background is obtained from data. The lower plots show the significances ($S/\sqrt{S+B}$) for these cuts.

To cut on the flight path of the V_0 in the rest frame of the V_0 candidate is the most efficient possibility to get rid of shortlived background, coming from the target region.

A similar dependence of signal and background on the applied cuts was observed for Λ and $\bar{\Lambda}$, but as Λs are longer lived particles compared to K^0_S (the flight path cut for K^0_S is

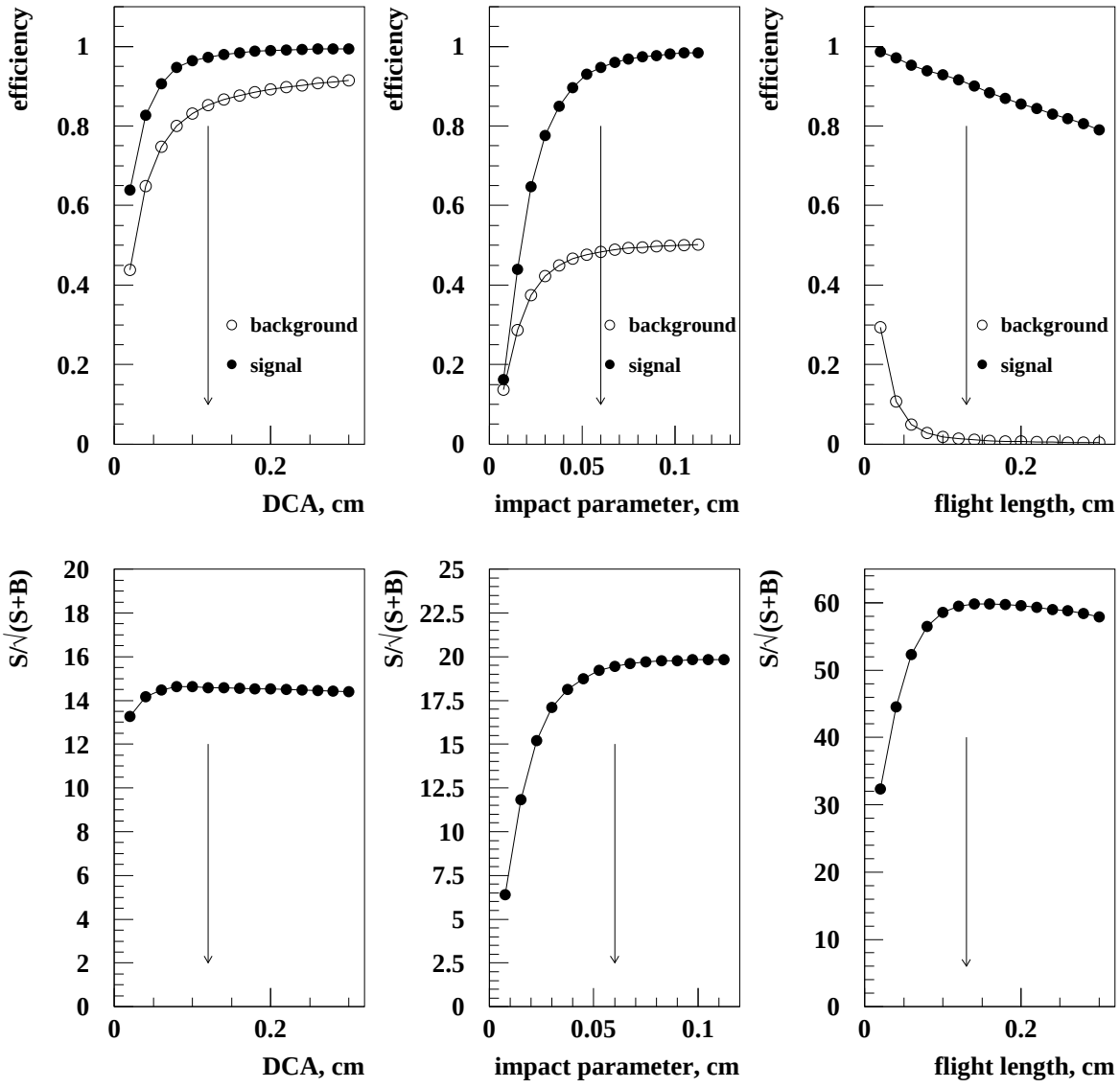

Figure 6.3: On the left, the dependence of signal and background on the cut on the applied distance between two tracks is shown. In the middle plot, the dependence of signal and background on the applied impact parameter cut. On the right, the dependence of signal and background on the applied flight path cut. The chosen cut values are indicated by the vertical arrows.

0.13 cm), the cut for them was increased to 0.39 cm, this corresponds to 5% of the flight path of Λs.

All cuts are selected such that they are placed in the flat regions of the efficiency curves. This allows us to be sure that if the V_0 MC signals behave not exactly like in data, additional systematic uncertainties are small.

6.3.3 Armenteros-Podolanski Plot

The kinematic properties of the V_0 candidates can be illustrated by the Armenteros-Podolanski plot. This is a two dimensional plot, of transverse momentum p_t of the oppositely charged decay products with respect to the V_0 versus the longitudinal momentum

asymmetry $\alpha = \frac{p_l^+ - p_l^-}{p_l^+ + p_l^-}$. The obtained distribution (see Fig.6.4) can be explained by the fact that decay products of the $K_S^0 \rightarrow \pi^+\pi^-$ have the same mass and therefore their momenta are distributed symmetrically on average, while for decays $\Lambda \rightarrow p\pi^-(\bar{\Lambda} \rightarrow \bar{p}\pi^+)$ the proton (antiproton) takes on average a larger part of the momentum and as a result the distribution is asymmetric.

K_S^0 are kinematically indistinguishable from $\Lambda/\bar{\Lambda}$ in the area where the corresponding bands of the Armenteros-Podolanski plot overlap and contribute to the background in the invariant mass distributions. A simple cut allows to remove these overlaps: all Λ and $\bar{\Lambda}$ candidates are removed that fulfill a K_S^0 mass hypothesis in the mass range $0.48\ GeV/c^2 \leq m_{K_S^0} \leq 0.515\ GeV/c^2$. The loss of V_0 signals due to the cut at the Armenteros-Podolanski plot is approximately 10-15%. The bands in the Armenteros-Podolanski plot can be explained by the applied mass cut.

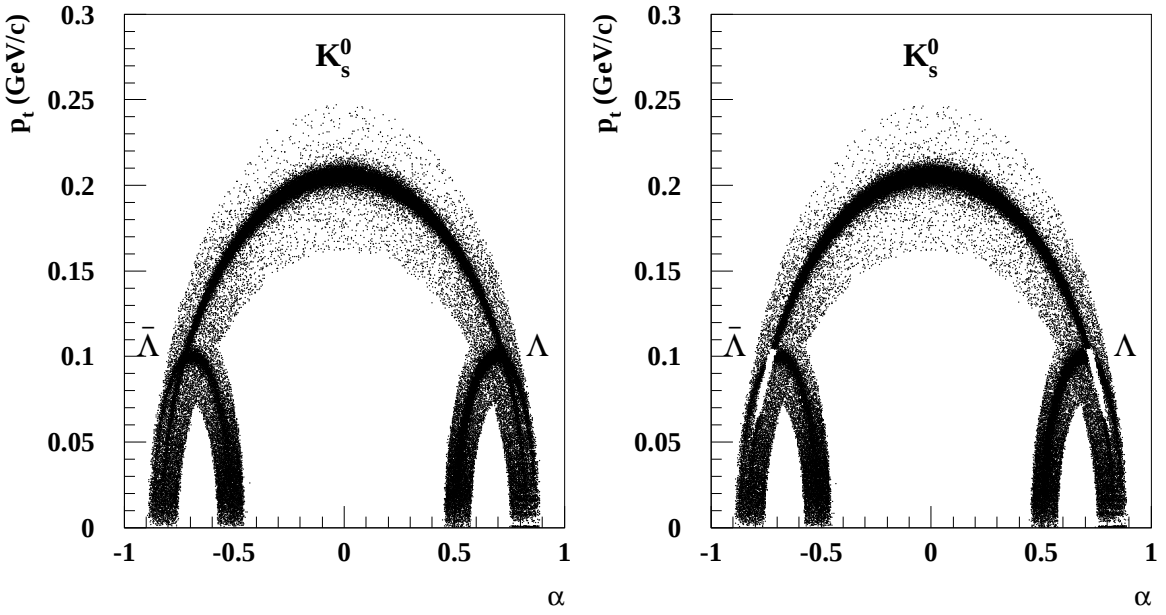

Figure 6.4: On the left, the Armenteros-Podolanski plot for K_S^0, Λ, $\bar{\Lambda}$ candidates reconstructed in run 20677. Right, the Armenteros-Podolanski plot after removal of overlap in the masses.

6.3.4 Summary of Used Cuts

The following selection criteria were used in the analysis to reject background and to ensure a reliable event reconstruction:

1. for the reconstruction of each track, at least 5 hits in the Vertex Detector System (VDS) and 5 hits in the Main Tracker (MT) have to be used,

2. tracks have to be marked by the clone removal algorithm as not being clones,

3. only opposite charged track pairs are considered,

4. for a quick rejection of track pairs a cut on the DCA between two V_0 candidate tracks is applied, cut at ≤ 0.12 cm.

5. for every track pair, three mass hypotheses are checked:

   (a) first the K^0_S mass hypothesis is checked, with a cut at the calculated invariant mass $0.428\ GeV/c^2 \leq m_{K^0_S} \leq 0.568\ GeV/c^2$. It corresponds to approximately 10σ of the signal mass width (see table 6.3),

   (b) at the next step Λ and $\bar{\Lambda}$ hypotheses are examined, taking into account the charge of the track with dominant momentum (in order to correctly assign the masses of decay products), with invariant mass cut
   $1.10\ GeV/c^2 \leq m_{\Lambda/\bar{\Lambda}} \leq 1.13\ GeV/c^2$. It corresponds to approximately 8 σ of the signal mass width (see table 6.3)

6. impact parameter cut of the V_0 candidate to the closest primary vertex, cut at $\leq$ 0.06 cm. This criteria is used also to select a primary vertex for the V_0's flight path calculation.

7. the most powerful cut is the cut on the flight path ($c\tau$) of the V_0 candidate in the V_0 rest frame, cut at ≥ 0.13 cm for K^0_S and cut at ≥ 0.39 cm for Λ, $\bar{\Lambda}$ candidates.

8. all Λ and $\bar{\Lambda}$ candidates which fulfill the K^0_S mass hypothesis in the mass region $0.48\ GeV/c^2 \leq m_{K^0_S} \leq 0.515\ GeV/c^2$ are removed

	K^0_S		Λ		$\bar{\Lambda}$	
Cut	$\varepsilon_{\mathrm{Sg}}$, %	$\varepsilon_{\mathrm{Bg}}$, %	$\varepsilon_{\mathrm{Sg}}$, %	$\varepsilon_{\mathrm{Bg}}$, %	$\varepsilon_{\mathrm{Sg}}$, %	$\varepsilon_{\mathrm{Bg}}$, %
Opposite charge requirement	100.0	–	100.0	–	100.0	–
Clone removal requirement	91.6	–	86.7	–	86.5	–
DCA ≤ 0.12 cm	97.2	15.1	94,9	18.2	96.0	17.6
Mass hypothesis	99.8	0.0	100.0	0.0	99.5	0.0
Impact Parameter ≤ 0.06 cm	93.3	51.6	90.8	47.1	89.5	49.
$c\tau \geq 0.13$ cm	90.6	98.7	91.6	94.9	89.8	95.2
K^0_S indistinguishable from Λ and $\bar{\Lambda}$ removal	88.8	7.3	86.9	12.1	89.9	12.7
Over all	66.7	99.5	59.5	98.1	59.7	98.2

Table 6.1: Cuts applied to the minimum bias data sample, efficiency and rejection for each cut for K^0_S, Λ and $\bar{\Lambda}$.

6.3.5 Detector Resolution

Using the full chain of the detector simulation, track reconstruction and V_0 selection, the resolution of the kinematic variables can be estimated. Fig. 6.5 shows residuals for kinematical variables x_F and p_t^2 for K^0_S, Λ and $\bar{\Lambda}$. The Feynman scaling variable (x_F) describes the longitudinal momentum P_z of the scattering product, expressed in terms of the maximally possible momentum P_{zmax},

$$x_F = \frac{P_z}{P_{zmax}}\,. \tag{6.1}$$

The quoted resolutions are from fits of Gaussians to the residual distributions (see Fig. 6.5), they are summarized below:

$$\sigma_{x_F(K^0_S)} = (0.32 \pm 0.01) \qquad \sigma_{p_t^2(K^0_S)} = (2.5 \pm 0.1)\ \ MeV^2/c^2 \tag{6.2}$$

$$\sigma_{x_F(\Lambda)} = (0.47 \pm 0.01) \qquad \sigma_{p_t^2(\Lambda)} = (3.2 \pm 0.2)\ \ MeV^2/c^2 \tag{6.3}$$

$$\sigma_{x_F(\bar{\Lambda})} = (0.46 \pm 0.01) \qquad \sigma_{p_t^2(\bar{\Lambda})} = (4.7 \pm 0.3)\ \ MeV^2/c^2 \tag{6.4}$$

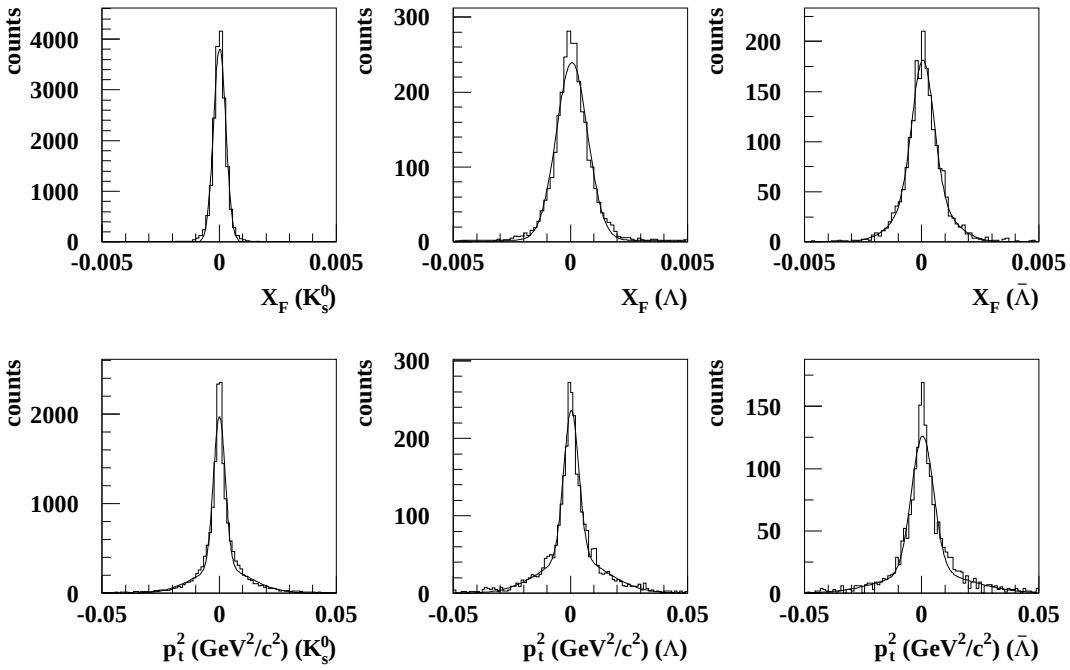

Figure 6.5: Top: Resulting residual distributions X_{gen}- X_{rec} for the x_F variable of K^0_S, Λ, $\bar{\Lambda}$. Bottom: Resulting residual distributions X_{gen}-X_{rec} for the p_t^2 variable of K^0_S, Λ, $\bar{\Lambda}$. Only V_0 candidates which were selected by the same analysis algorithm are used for these plots.

The bin widths are chosen 0.015 for x_F variable and 0.2 MeV^2/c^2 for p_t^2.

6.4 Acceptance

In order to produce a cross section measurement effects of the detector acceptance have to be corrected. For the proper acceptance determination, parameters like detector efficiencies and resolution are very important, because they can influence the track reconstruction efficiency. For the simulation of the Innner Tracker performance, the efficiencies obtained in the ITR performance studies and described in the Section 5 are used.

For the study of the acceptance of HERA-B 1,000,000 inelastic events for each target wire, used during data taking in 2002, were generated with the HERA-B Monte-Carlo chain, including the full detector simulation.

The overall acceptance can be subdivided into the geometrical acceptance and the reconstruction efficiency. A V_0 is considered to be in the geometrical acceptance of the

detector if its decay products pass through enough layers of tracking stations in the PC area. In additional, the decay's vertex has to be measured, which means the tracks have to be measured by the Vertex Detector System. These requirements are checked with the Monte Carlo Impact Points (MIMPs) and the decay position (z coordinate) of the V_0 candidate. A requirement on the number of crossed layers in the PC area is needed, because a track with less than 5 MIMPs can not be reconstructed by the pattern recognition program. The cut at the z position of the secondary vertex is based on the plot shown in Fig. 6.6

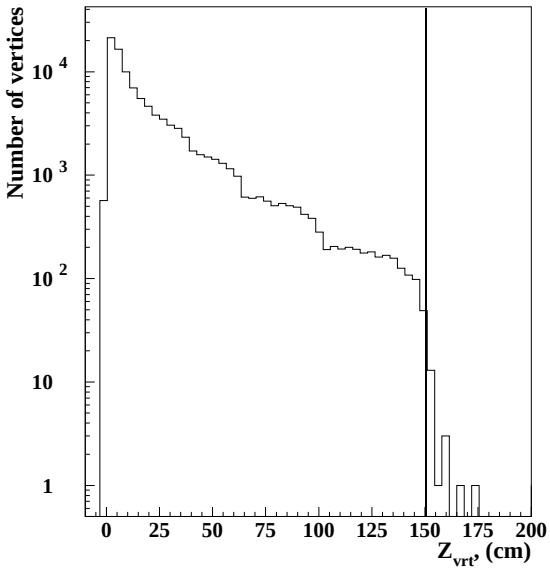

Figure 6.6: Reconstructed secondary vertex Z coordinate distribution for run 20678 taken with Below I wire (Carbon). The cut applied in the analyzed events is indicated.

Finally, the requirements used for this study were:

1. tracks have to pass through at least one superlayer and produce at least 5 MIMPs each in Main Tracker (Inner + Outer tracker),

2. the V_0 has to decay before 155 cm from the target ($z_{\text{target}} - z_{\text{vert.second.}}$).

The geometrical description used for this acceptance study is valid for the detector configuration used during data taking in 2002/2003 (both Inner Tracker and Outer Tracker were fully installed and equipped). The resulting geometrical acceptance functions are shown in Fig. 6.7.

For the cross-section calculation a full acceptance (geometrical acceptance plus reconstruction efficiencies) function is needed. In order to obtain the full acceptance function, the generated MC sample was reconstructed and distributions of the kinematical variables (x_F, p_t^2) are produced. Such variables are chosen because they are of special interest for the fragmentation processes. The kinematical variables are plotted for reconstructed MC and the original MC truth. The ratios of these distributions:

$$A = \frac{X_{\text{MC reco}}}{X_{\text{MC truth}}}, \tag{6.5}$$

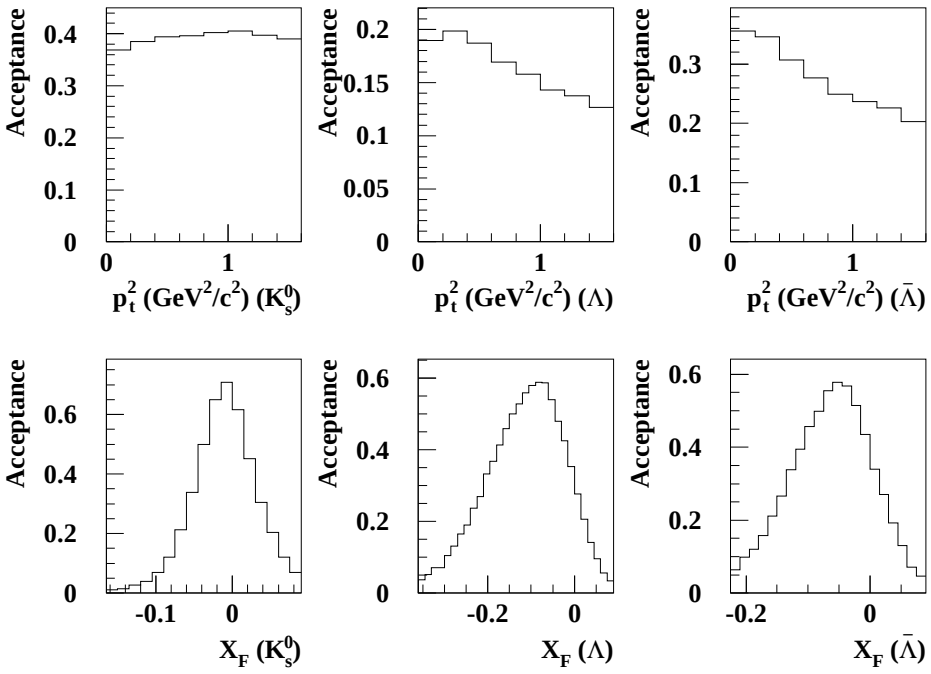

Figure 6.7: Geometrical acceptances for V_0s.

are the final acceptance functions (see Fig. 6.8).

The HERA-B spectrometer covers the central production region in the overall proton-nucleon center of mass system. This can be seen from the acceptance plots as a function of x_F. The range -0.03 $< x_F <$ 0.01 is covered with an acceptance larger than 0.1 and with lower acceptance it extends up to -0.12 and 0.04 for K_S^0. Acceptances of Λs and $\bar{\Lambda}$s are approximately covering the same region with lower values $\approx 6\%$ and the center of gravity of the distributions are shifted more to the negative region compared to the acceptance of the K_S^0.

6.5 Luminosity Determination

In HERA-B several methods for luminosity determination are available [56]. The algorithms used for luminosity determination of minimum–bias data taken in 2002/2003 are discussed in this section. The luminosity L is the number of particles passing down the line per unit time, per unit area, and can be expressed as:

$$L = \frac{\mathrm{d}N}{\mathrm{d}\sigma}, \tag{6.6}$$

where $\mathrm{d}N$ is the number of particles per unit time passing through area $\mathrm{d}\sigma$. At fixed target experiments the luminosity is proportinal to the number of beam particles hitting the target. The time integrated luminosity in case of HERA-B is defined as:

$$L = \frac{N_{proc}}{\sigma_{proc}}, \tag{6.7}$$

where N_{proc} is the number of interactions of a process of a specific type in a given time interval and σ_{proc} is the process cross section. The cross section of inelastic processes

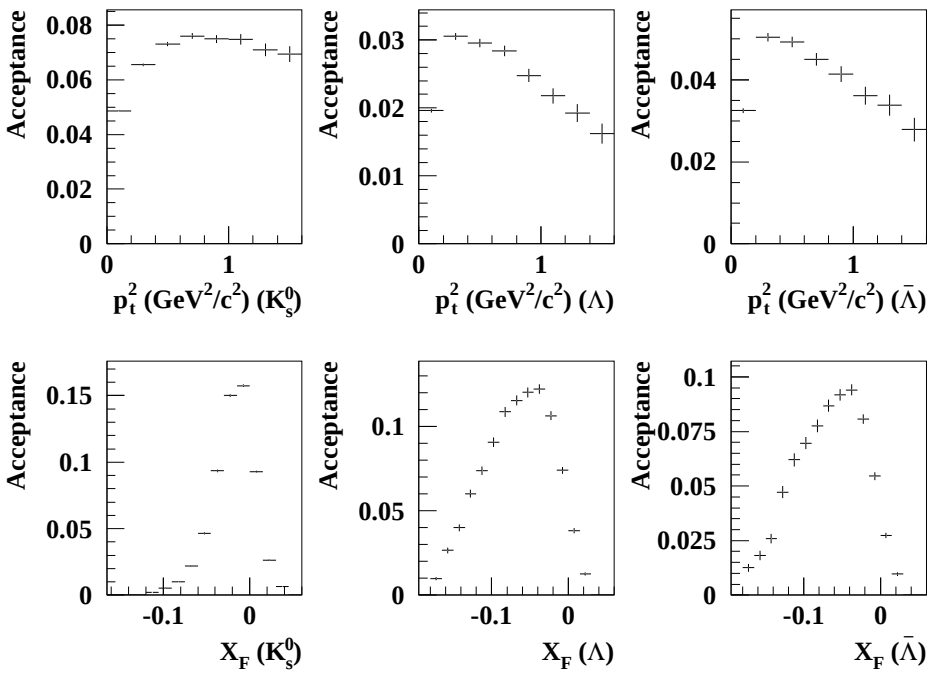

Figure 6.8: Acceptances for V_0s, including geometrical acceptances and reconstruction efficiencies. For the acceptance determination the standard MC sample for Below I wire (Carbon) was used.

σ_{inel} dominates the total pN cross section for HERA-B energies. Therefore one uses for the luminosity determination, the inelastic cross section as reference. Another advantage is that σ_{inel} is known with a good accuracy and measured for a large variety of target materials and beam energies. Taking into account the HERA proton bunch structure and HERA-B setup of 2002/2003, the luminosity can be expressed as follows:

$$L = \frac{N_{BX}^{SLT}}{\sigma_{inel}}\lambda, \tag{6.8}$$

where N_{BX}^{SLT} indicates how many times filled bunches crossed the target region and λ is the mean number of interactions for filled bunches.

For the luminosity determination of the minimum bias data of 2002/2003 three different methods were used:

1. *Hodoscope counters.* For the interaction rate measurement four pairs of scintillators mounted in front of the ECAL are used, they are placed symmetrically around the proton beam. Hodoscopes provide a good linearity between rate and mean number of interactions but they have only a small acceptance.

2. *ECAL energy sum method.* The idea used in this method is that the mean total energy deposited in the ECAL is proportional to the average number of superimposed interactions.

3. *Primary vertex counting method and counting of tracks from primary vertices.* The algorithm is based on the assumption that the number of reconstructed primary

vertices and the number of tracks assigned to the primaries scales linearly with the average number of superimposed interactions.

Hodoscope counters

The rate in the HERA-B setup 2002/2003 was measured by four pairs of scintillators, placed symmetrically around the beam pipe. Each counter has a geometrical acceptance equal to approximately 0.15%. The acceptance of these counters has been calibrated relative to a large acceptance hodoscope ($\approx$ 54% acceptance). This large acceptance hodoscope was temporary installed inside the magnet. Interaction rate measured by the hodoscope counters can be expressed as follows

$$\lambda = \frac{R_{\mathrm{HOD}} \cdot \varepsilon}{R_{\mathrm{BX}}}, \tag{6.9}$$

where R_{HOD} is the rate measured by the hodoscopes, ε is an acceptance correction factor, $R_{\mathrm{BX}} = 180R_0/220$ is the rate of the non-empty bunches crossing the target region and $R_0 = 1/96$ ns is the bunch crossing rate. However, there are several reasons why additional sources for rate calculation are needed:

- The acceptance of the counters was measured in 1998. Later the large acceptance hodoscope was removed to install the tracking stations. Therefore the acceptance of the small counters has changed, since it is depending on the amount of material in front of them.
- Sensitivity of the hodoscopes to non–interaction related background (coasting beam).

ECAL Energy Sum

The idea behind this method is that average energy measured in the ECAL proportional to the mean number of superimposed interactions.

The average energy $E^{(N)}$ deposited by events with exactly N interactions is

$$E^{(N)} = \frac{\sum_{i=1}^{N_{total}} E_i I(n_i \approx N)}{\sum_{i=1}^{N_{total}} I(n_i \approx N)}, \tag{6.10}$$

where N_{total} is the number of considered events, E_i is the total energy deposited in the calorimeter per event and n_i is the number of interactions per event. The mean energy can be expressed as

$$\bar{E} = \sum_{i=1}^{\infty} E^{(N)} P(N), \tag{6.11}$$

where $P(N)$ is the distribution function for the number of interactions N with the mean value λ. Assuming that the energy scale linearly with the number of superimposed interactions, the mean number of interaction can be expressed as

$$\lambda = \frac{\bar{E}}{E^{(1)}} \tag{6.12}$$

The assumed linearity of the ECAL energy with respect to the number of interactions was checked by a Monte Carlo simulation and verified with experimental data. A typical distribution of the average energy dependence on the interaction rate for two wire materials carbon and titanium, obtained on data, is shown in Fig. 6.9.

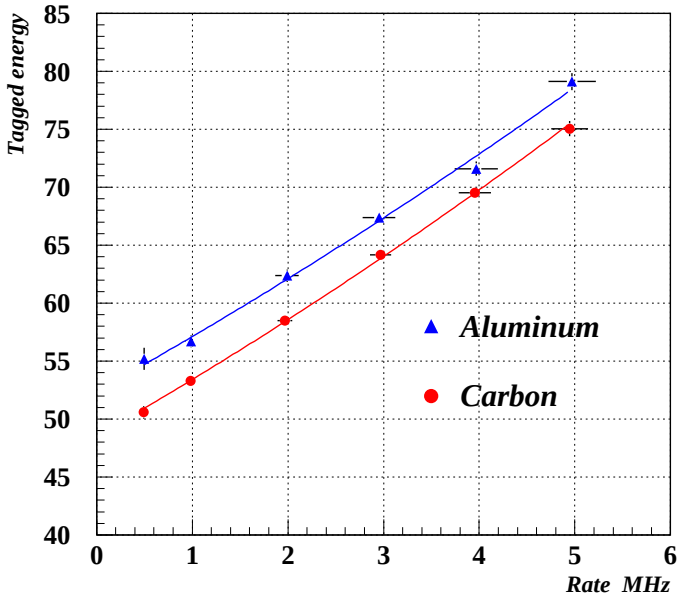

Figure 6.9: Dependence of energy deposited in the ECAL as a function of the interaction rate for carbon and titanium wire obtained with the help of rate scans.

For the purpose of determining the luminosity, special runs have been taken, in which the interaction rate has been varied from the minimum till maximum value.

The energy of a single interaction can be determined from MC or data. A single interaction can be tagged in the zero-rate limit (at low rate the probability to have multiple interactions becomes negligible small), by requiring at least one cell with energy above threshold, such event is called "tagged" event. Taking into account the assumption that the number of interactions follows the Poisson statistics, the mean energy per tagged event can be defined as a function of the parameter λ

$$< E >_{tagged} = \frac{\lambda E^{(1)}}{1 - e^{-\lambda\varepsilon(1)}}, \tag{6.13}$$

where $\varepsilon(1)$ is the efficiency to tag an event (measured on MC), $E^{(1)}$ is the energy released with one interaction [57]. The energy $E^{(1)}$ is obtained from a fit to the mean energy of tagged events using function 6.13

Vertex Detector System based method

As an additional method the response of the Vertex Detector System is used. Assuming that the number of reconstructed tracks and vertices scales linearly with the number of interactions N, we can express λ in a similar way as in the case of the ECAL energy sum method

$$\lambda = \frac{< n >_{\text{tracks}}}{< n >^{(1)}_{\text{tracks}}}, \tag{6.14}$$

$< n >_{\text{tracks}}$ is the average number of tracks assigned to vertices and $< n >^{(1)}_{\text{tracks}}$ is the average number of tracks assigned to one interaction. In order to extract the average number of tracks for one interaction a similar function (6.13) as for the ECAL energy sum method is used to fit the distribution of track multiplicity versus interaction rate.

The obtained numbers ($\varepsilon_{\text{ECAL}}$, $\varepsilon_{\text{vert}}$, $\varepsilon_{\text{IA trig}}$) are used to calculate the total number of filled bunches which crossed the target region and to correct the efficiencies of the applied cuts. The N_{BX}^{SLT} for each of the methods can be expressed as follows

$$N_{BX}^{SLT} = \frac{N_{\text{tape}}}{1 - e^{-\lambda} - e^{-\lambda\varepsilon_{\text{IA trig}}}}, \tag{6.15}$$

where λ is the average number of interactions determined with the Hodoscope counters,

$$N_{BX}^{SLT} = \frac{N_{E>E_{\text{thr}}}}{1 - e^{-\lambda\varepsilon_{\text{ECAL}}} - e^{-\lambda\varepsilon_{\text{IA trig}}}}, \qquad N_{BX}^{SLT} = \frac{N_{\text{vert}>0}}{1 - e^{-\lambda\varepsilon_{\text{vert}}} - e^{-\lambda\varepsilon_{\text{IA trig}}}}. \tag{6.16}$$

The λs are measured with random triggered data.

The numbers obtained with the different methods were compared for a set of runs for different wires. The results of the comparison are shown in Fig. 6.10 for Tungsten wire. The measurements obtained with the "mean" and "Poisson" method are in good agreement. The estimated systematic error of the luminosity measurements is $\approx 10\%$. The final luminosity numbers used in the analysis are listed in Appendix A.

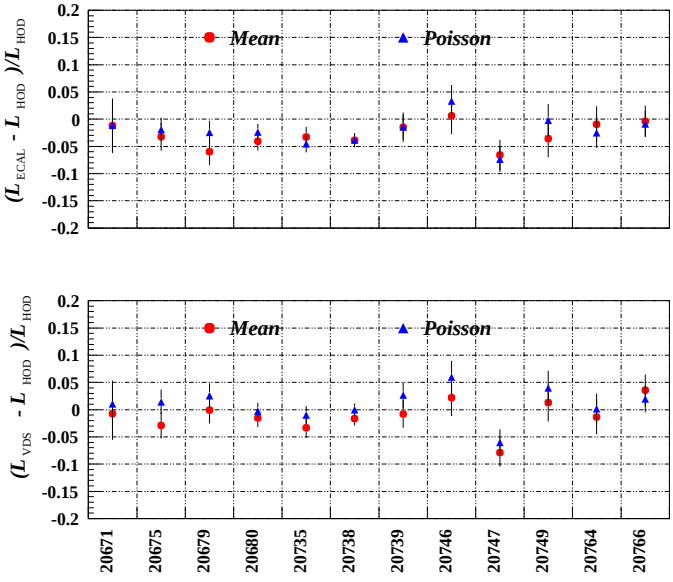

Figure 6.10: Distribution of the average number of interactions measured with VDS and ECAL methods relative to the measurements obtained with Hodoscopes for the Tungsten wire [58].

6.6 MC and Data Comparison

In order to understand differences between MC and data, a comparison of the main kinematical variables is performed. For each bin an invariant mass distribution for the corresponding V_0 candidate is produced. All obtained distributions are fitted by a Gaussian plus a polynominal of second order to describe the background. Finally in order to simplify the comparison, distributions of kinematical variables for data and MC are normalized to the same area.

The following kinematical variables are compared:

1. azimuthal angle (Φ) of the V_0 candidate,
2. polar angle (Θ) of the V_0 candidate,
3. Feynman x (x_F) of the V_0 candidate in the center of mass system,
4. rapidity (y) of the V_0 candidate in the center of mass system,

$$y = \frac{1}{2} ln \frac{E + p_z}{E - p_z} \,, \tag{6.17}$$

5. squared transverse momentum (p_t^2) of the V_0 candidate in the laboratory frame,

$$p_t^2 = p_x^2 + p_y^2 \,, \tag{6.18}$$

6. momentum (p) of the V_0 candidate in the laboratory frame,
7. flight path ($flight$) of the V_0 candidate in the rest frame,

The distributions of x_F and p_t^2 are of special interest for this analysis. In case of K_S^0 MC and data show an agreement on the level of 10-20%. The simulated distribution of x_F for Λ is within 25% in agreement with data, p_t^2 distribution within 30%. The x_F distribution of $\bar{\Lambda}$ demonstrated a better agreement, the maximum reached difference is o f the order of 15%, in case of p_t^2 distribution it is 30%.

Above a p_t^2 of about 0.8 GeV^2/c^2 the distributions for all three particles show large differences between MC and data. Such behaviour is due to a simplified model used in MC, p_t^2 spectra is simulated with one exponential. Data distributions indicate that it is better described by two exponentials. This behavior is well known and was mentioned already by [55].

6.6.1 ITR Contribution and Stability

The Inner Tracker participated during the minimum bias data taking in 2002-2003 and the contribution from ITR tracks to V_0 signal is estimated to be of the order of $\approx 20\%$. Since the ITR data was used in the analysis the question about the performance stability is very important. Studies of the ITR hit efficiency are described in Chapter 5.

For the acceptance and stability studies a special set of tracks is used. Tracks which are reconstructed with the help of at least 10 hits found in the ITR are called *tracks with significant contribution from the ITR detector*. This criterion is chosen because 10 ITR

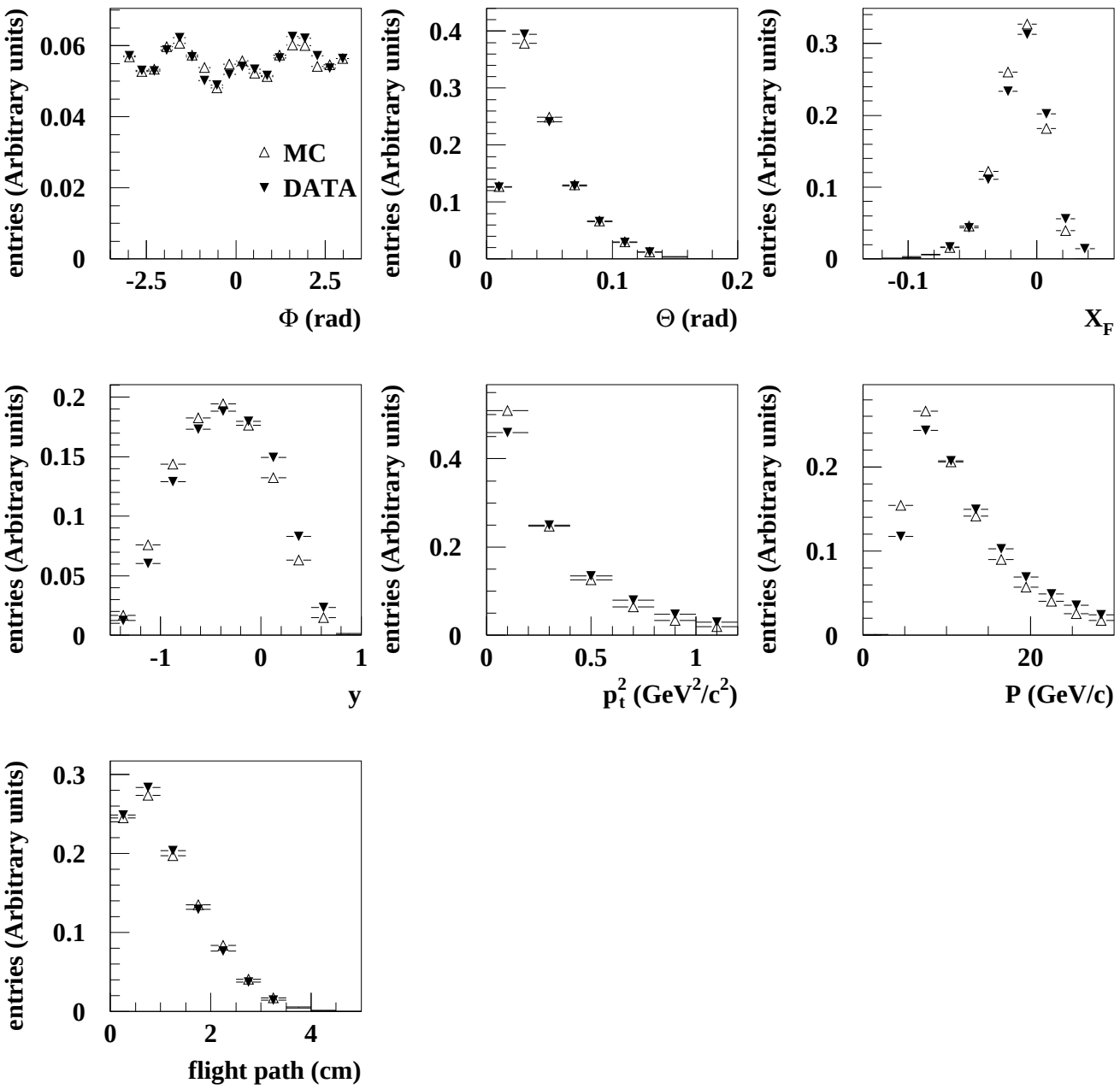

Figure 6.11: Comparison of K^0_S properties in MC and data. (filled triangles: MC, empty triangles: data.)

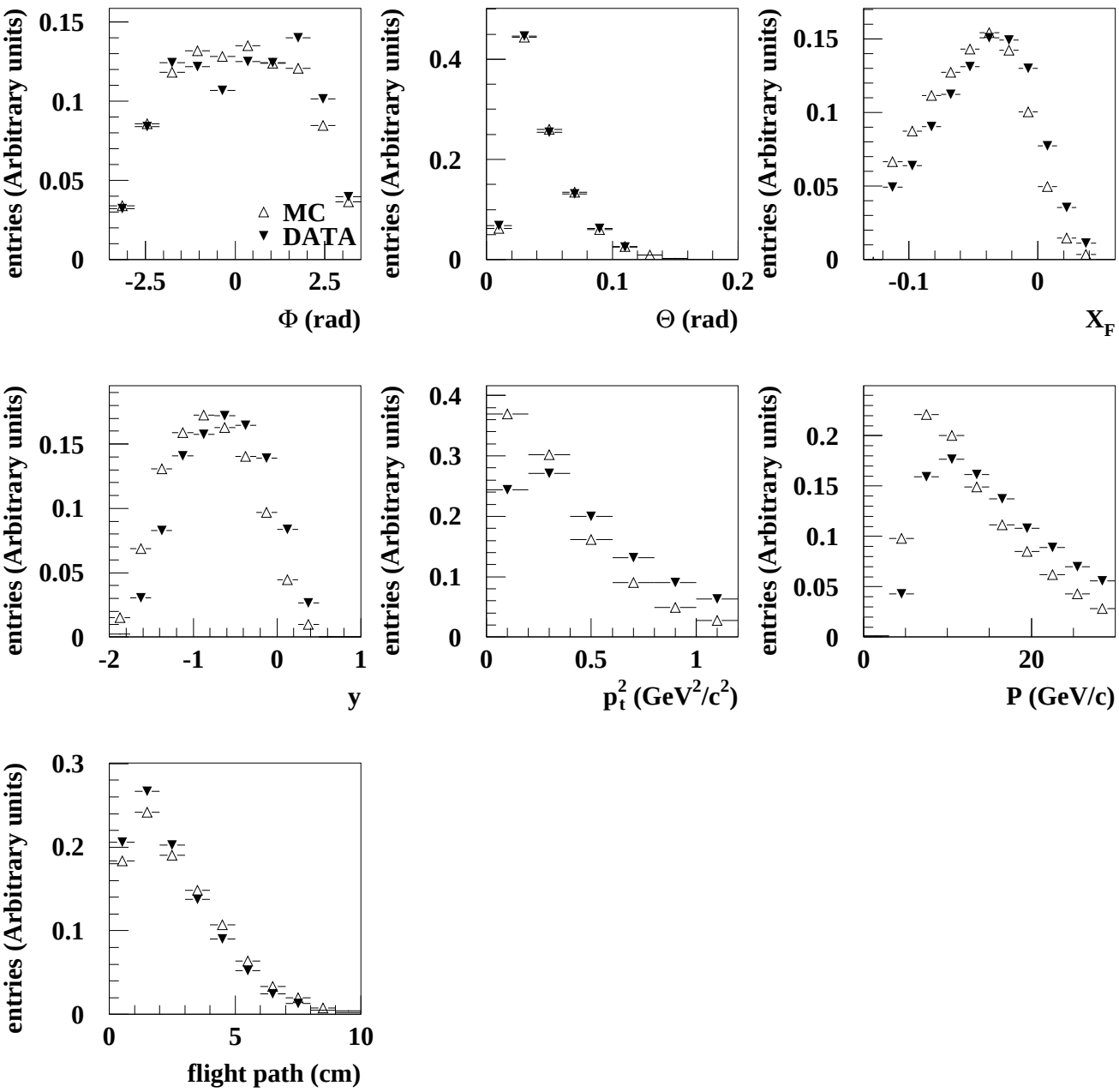

Figure 6.12: Comparison of Λ properties in MC and data. (filled triangles: MC, empty triangles: data.)

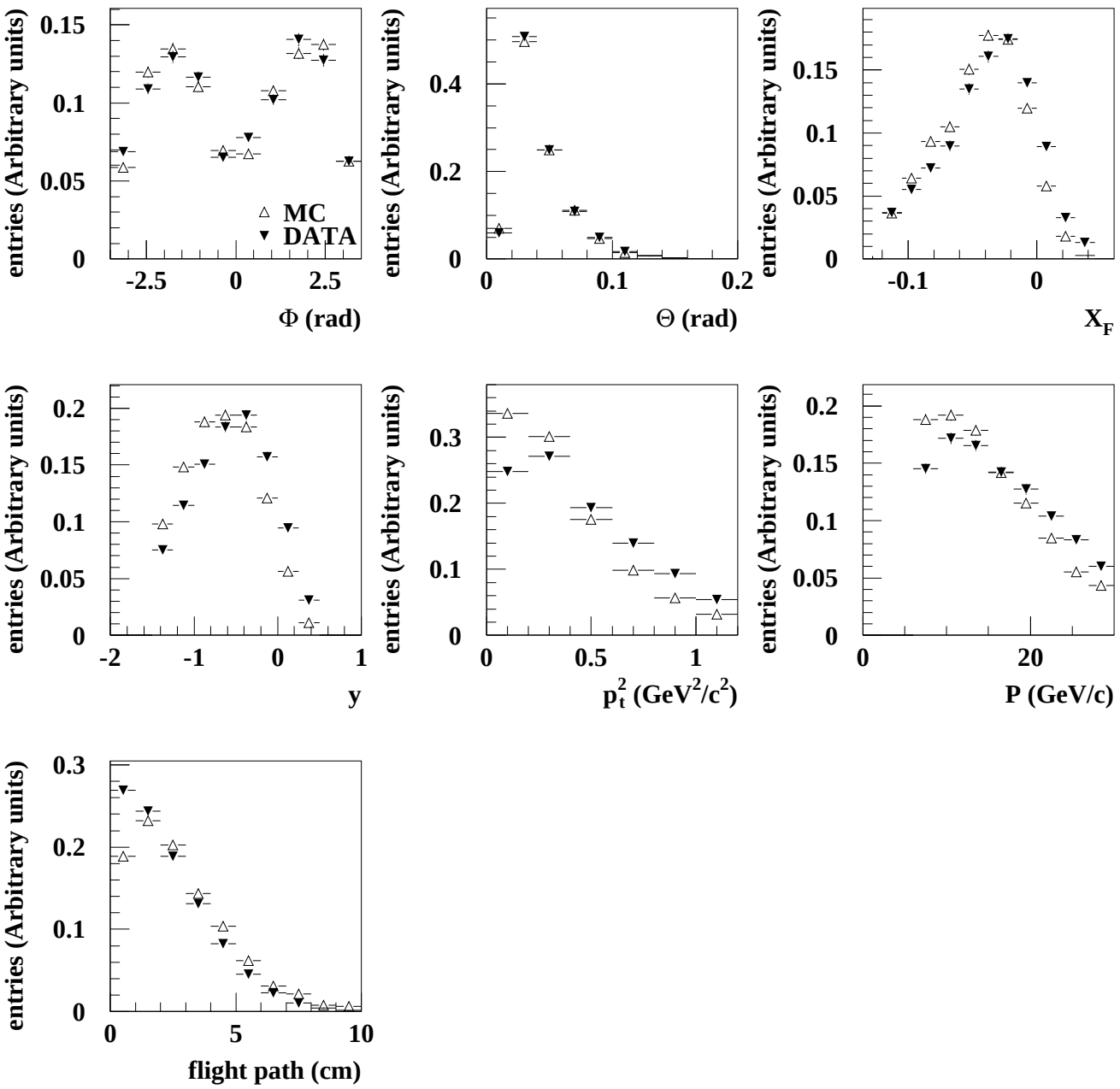

Figure 6.13: Comparison of $\bar{\Lambda}$ properties in MC and data. (filled triangles: MC, empty triangles: data.)

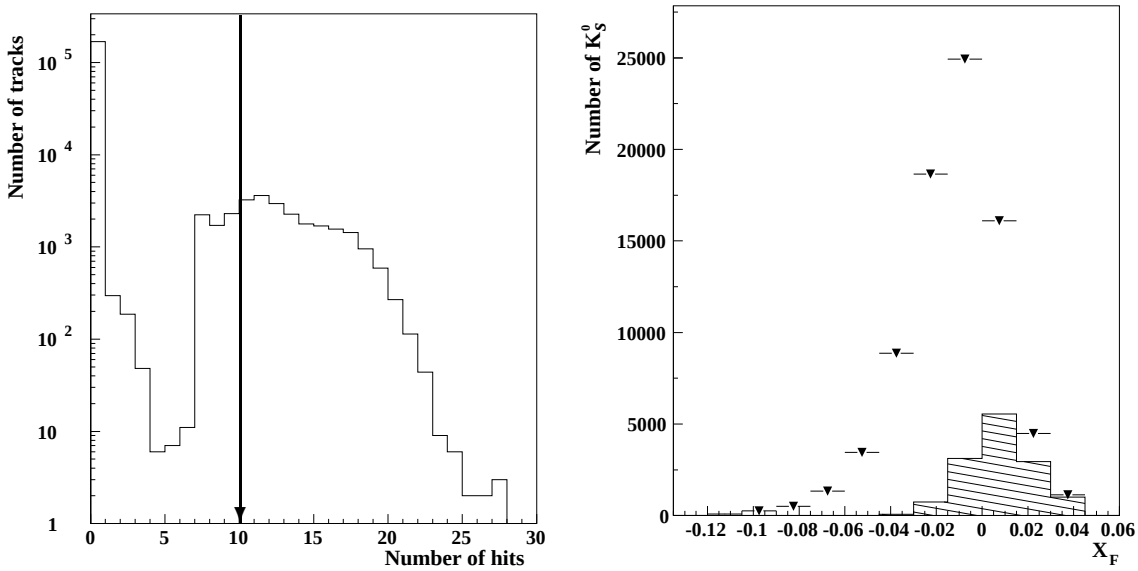

Figure 6.14: Left: distribution of the number of hits used in the Inner Tracker detector for reconstruction of track segments (run 20768). The applied cut is indicated by the arrow. On the right, the x_F distribution for K^0_S obtained with tracks with a large fraction of ITR hits (dashed), overlapped with x_F distribution obtained with all tracks.

hits correspond to approximately two superlayers crossed by a track. The distribution of ITR hits used for track reconstruction is shown in Fig. 6.14 left.

For those tracks which fulfilled the requirement mentioned above, the x_F distribution for K^0_S is shown in Fig. 6.14 (right plot), for comparison the x_F spectrum for K^0_S obtained with all tracks is overlapped. The contribution of the ITR is mainly in the positive x_F region, and the fraction of V_0s with large number of ITR hits is approximately 17-18%.

The next important point is the performance stability check. All runs which were proposed for the analysis were checked and a decision about the usability was done based on the following information: recorded module synchronization problems, power failures and data performance plots from the off-line reconstruction DQ. In addition the number of V_0s reconstructed with large fraction of ITR hits (more than 10 hits) and the number of V_0s reconstructed with all tracks are plotted versus time. The distribution of the number of reconstructed K^0_S versus time obtained for one of the runs is shown in Fig. 6.15. This run is one of the problematic runs, during it a power failure of MS13- and MS12+ happened. This failure can be seen as a drop of the number of K^0_S reconstructed with the help of the ITR tracks versus time at the middle plot.

Those runs which showed instabilities (like in the Fig. 6.15) are excluded from the analysis. In all other runs ITR tracks were kept in order to increase the statistics and to extend the kinematical acceptance.

6.7 V_0 signals

The final V_0 invariant mass distributions from the considered minimum bias data set for all four wires are shown in Figures 6.16 and 6.17 (all above described cuts are applied).

Each invariant mass distribution is fitted with a Gaussian plus polynomial of second

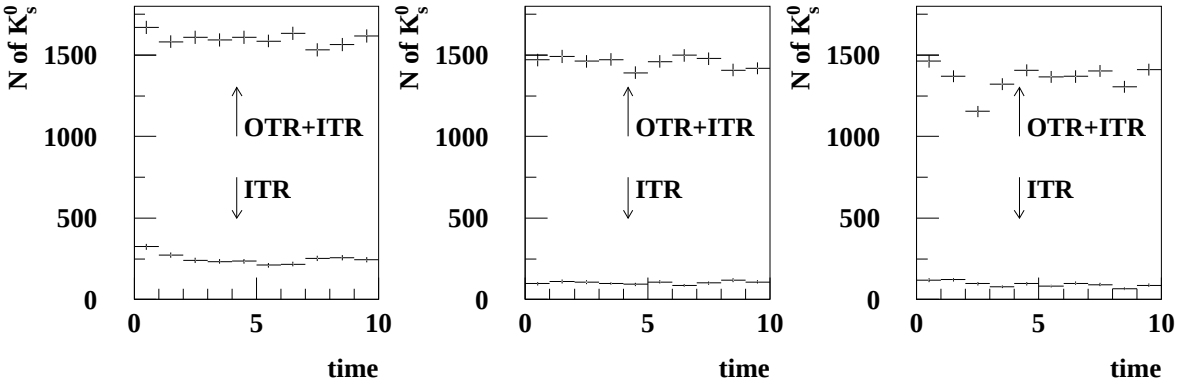

Figure 6.15: Number of K^0_S reconstructed with all tracks (OTR+ITR) and number of K^0_S reconstructed with tracks with a large fraction of ITR hits in the run 20695. Each bin contains approximately 50,000 consecutive events.

order. The obtained signals are summarized in table 6.2, the widths and the peak positions in table 6.3.

Wire	Inner II	Inner I	Below I	Below II
Material	Carbon	Tungsten	Carbon	Titanium
N(events)	17,514,469	9,969,385	14,414,486	10,222,072
N(K^0_S)	395,319. $\pm$ 880.	299,590. $\pm$ 773.	268,594. $\pm$ 817.	264,586. $\pm$ 721.
N(Λ)	82,830. $\pm$ 453.	70,139. $\pm$ 338.	56,832. $\pm$ 350.	59,759. $\pm$ 360.
N($\bar{\Lambda}$)	39,660. $\pm$ 559.	34,450. $\pm$ 343.	27,535. $\pm$ 277.	27,827. $\pm$ 291.

Table 6.2: V_0 yield used in the analysis, based on runs taken in 2002.

Wire	$\sigma_{K^0_S}$, MeV	$M_{K^0_S}$, MeV	σ_Λ, MeV	M_Λ, MeV	$\sigma_{\bar{\Lambda}}$, MeV	$M_{\bar{\Lambda}}$, MeV
Inner II	5.$\pm$0.01	497.14$\pm$0.01	1.8$\pm$0.01	1115.43$\pm$0.01	1.82$\pm$0.03	1115.7$\pm$0.06
Inner I	5.06$\pm$0.01	497.28$\pm$0.01	1.83$\pm$0.01	1115.61$\pm$0.01	1.82$\pm$0.02	1115.6$\pm$0.01
Below I	5.01$\pm$0.01	497.24$\pm$0.01	1.79$\pm$0.01	1115.63$\pm$0.1	1.77$\pm$0.02	1115.6$\pm$0.01
Below II	5.04$\pm$0.01	497.24$\pm$0.01	1.8$\pm$0.01	1115.62$\pm$0.01	1.81$\pm$0.02	1115.5$\pm$0.01

Table 6.3: Widths and peak positions of V_0s obtained from the signal spectrums fits (signal spectrums are shown in table 6.2).

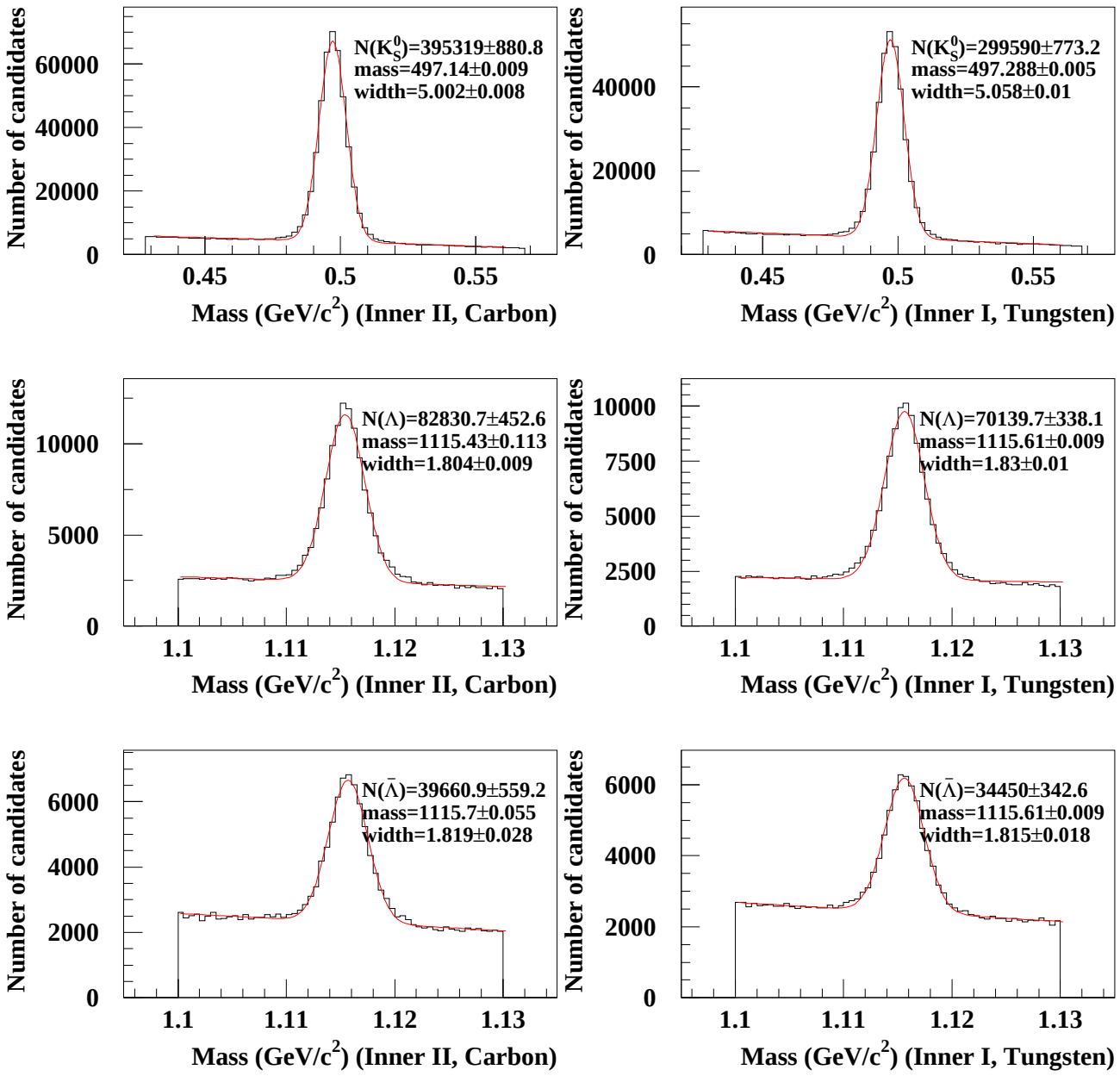

Figure 6.16: V_0 signals found in the 2002/2003 minimum bias data set. From the top to the bottom: invariant mass distributions for K^0_S, Λ and $\bar{\Lambda}$ candidates for runs taken Inner I and Inner II wires.

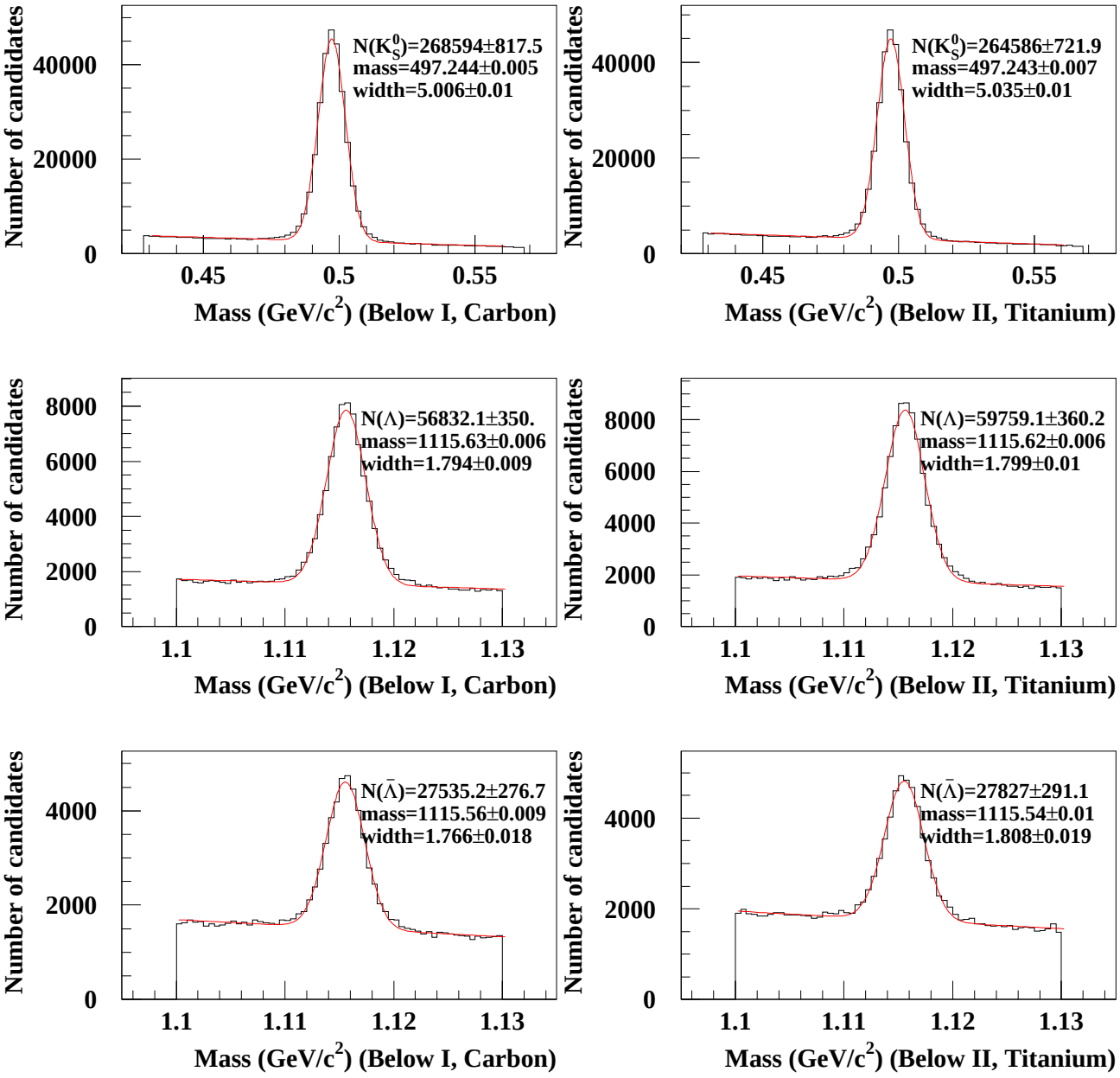

Figure 6.17: V_0 signals found in the 2002/2003 minimum bias data set. From the top to the bottom: invariant mass distributions for K^0_S, Λ and $\bar{\Lambda}$ candidates for runs taken Below I and Below II wires.

6.8 Cross Section

The production cross section for V_0 particles in the acceptance of the HERA-B detector can be expressed as follows:

$$\sigma_{V_0} = \frac{1}{Br(V_0)L} \iint \frac{N(p_t^2, x_F)}{\epsilon(p_t^2, x_F)} \, \mathrm{d}p_t^2 \, \mathrm{d}x_F \tag{6.19}$$

where $N(p_t^2, x_F)$ is the number of observed V_0s in bins of p_t^2 and x_F and $\epsilon(p_t^2, x_F)$ is the total acceptance which includes geometrical acceptance of the detector and reconstruction efficiency (see Section 6.4) for the considered kinematical range. The branching ratios $Br(V_0)$ are taken from Ref. [60] , and L is the luminosity which has been calculated for each wire separately, as it is described in 6.5.

The inclusive differential cross section per nucleon $\mathrm{d}\sigma_{pA}/\mathrm{d}x_F$ for various targets and target materials are shown in Table 6.4 for the x_F range [-0.12,0]. The inclusive differential cross section per nucleon $\mathrm{d}\sigma_{pA}/\mathrm{d}x_F$ for various targets and target materials are shown in Table 6.5 for the positive x_F range.

Particle	Target	$\mathrm{d}\sigma_{pA}/\mathrm{d}x_F$ (mb)	σ_{pA} (mb)
K_S^0	C	337.1 ± 17.6 ± 60.	135.2 ± 7.1 ± 20.5
	Ti	1709.2 ± 95.3 ± 227.8	693.7 ± 38.7 ± 92.5
	W	4521.2 ± 241.3 ± 617.4	1835. ± 98. ± 250.8
Λ	C	85.6 ± 4.4 ± 15.1	61.2 ± 3.2 ± 11.
	Ti	428.3 ± 22.9 ± 67.1	306.2 ± 16.4 ± 47.9
	W	1078.2 ± 55.9 ± 194.1	767.9 ± 39.9 ± 138.2
$\bar{\Lambda}$	C	42.1 ± 2.3 ± 6.5	14.8 ± 0.8 ± 2.7
	Ti	185.5 ± 11.9 ± 35.3	73.9 ± 4.2 ± 14.9
	W	550.7 ± 29.7 ± 85.4	193.4 ± 10.4 ± 36.0

Table 6.4: The inclusive differential cross sections for the $-0.12 \leq x_F < 0$ range for the production of K_S^0, Λ and $\bar{\Lambda}$ particles. The total cross sections obtained by extrapolation to the $-1. \leq x_F \leq 1$ range are listed.

In order to be comparable with results from other experiments the obtained cross sections have to be extrapolated to the full x_F range [-1.,1.]. The extrapolation was based on the measurements in the negative x_F region by using the parameterization $\mathrm{d}\sigma_{pA}/\mathrm{d}x_F \propto (1 - x_F)^n$ [62]. The parameter n is constant and values for different strange particles are taken from the measurements of inclusive strange-particle production done by other experiments [61]. The resulting production cross sections σ_{pA} for V_0 are listed in Table 6.4.

The differential cross sections $\mathrm{d}\sigma_{pA}/\mathrm{d}p_t^2$ are listed in Table 6.7. The results are plotted in Fig. 6.18, fits are done by the function

$$\frac{\mathrm{d}\sigma_{pA}}{\mathrm{d}p_t^2} = \sigma B exp(-Bp_t^2), \tag{6.20}$$

where B is a parameter independent from x_F and p_t^2 [63]. Measured parameter B for different target materials are listed in Table 6.6. The measured p_t^2 spectra is well described by the Eq. 6.20.

$\triangle x_F$	C	Ti	W
		K^0_S	
0. - 0.015	665.3 ± 7.5 ± 133.1	3056.5 ± 41.8 ± 611.3	7850.4 ± 71.7 ± 1570.1
0.015 - 0.03	648.3 ± 14.5 ± 129.7	2878.1 ± 78.9 ± 575.6	7439.9 ± 137.2 ± 1487.8
0.03 - 0.045	665.9 ± 33.1 ± 133.2	2773.3 ± 177.6 ± 554.6	6757.9 ± 289.9 ± 1351.6
0.045 - 0.06	626.8 ± 65.2 ± 125.4	3387.6 ± 554.7 ± 677.5	8482.1 ± 861.5 ± 1696.4
		Λ	
0. - 0.015	171.2 ± 8.3 ± 34.2	1149.3 ± 78.1 ± 229.8	2595.1 ± 102.4 ± 519.2
0.015 - 0.03	236.2 ± 19.6 ± 47.2	1217.6 ± 131.8 ± 243.5	2947.2 ± 188.3 ± 589.4
0.03 - 0.045	269.5 ± 44.5 ± 53.9	1327.1 ± 257.6 ± 265.4	4412.2 ± 588.2 ± 882.4
		Λ	
0. - 0.015	108.1 ± 6.4 ± 21.6	533.3 ± 41.1 ± 106.6	1345.9 ± 67.1 ± 269.2
0.015 - 0.03	111.5 ± 11.4 ± 22.3	646.1 ± 87.3 ± 129.2	1352.9 ± 112.7 ± 270.6
0.03 - 0.045	105.5 ± 17.9 ± 21.1	917.5 ± 277.4 ± 183.5	2263.7 ± 420.2 ± 452.7

Table 6.5: The inclusive differential production cross section $\mathrm{d}\sigma_{pA}/\mathrm{d}x_F$ in mb for K^0_S, Λ and $\bar{\Lambda}$ particles measured on three different targets for positive x_F range.

	$B(GeV/c)^{-2}$		
	C	Ti	W
K^0_S	3.3 ± 0.3	3.1 ± 0.3	3.1 ± 0.3
Λ	2.1 ± 0.2	2. ± 0.3	2.0 ± 0.2
$\bar{\Lambda}$	2.3 ± 0.2	2.1 ± 0.2	2.1 ± 0.2

Table 6.6: The values of the parameter B obtained by fitting the differential cross section.

The differential production cross sections $\mathrm{d}\sigma_{pA}/\mathrm{d}p_t^2\mathrm{d}x_F$ are listed in Table 6.8-6.10. Only statistical errors are quoted here.

The ratios of production cross sections from the measurements listed above for mid-rapidity for Carbon wire are

$$\frac{\sigma(K^0_S)}{\sigma(\Lambda)} = 5.9 \pm 0.3, \ \frac{\sigma(\bar{\Lambda})}{\sigma(\Lambda)} = 0.68 \pm 0.07.$$

Fig. 6.19 shows the ratios for all three different target materials used.

The dependences of production cross sections on the atomic number of the target material are shown in Fig. 6.20 and fitted by the $\sigma_{pA} \propto A^{\alpha}$. Production cross sections and α obtained from the fit are listed in Table 6.11.

The production cross sections per nucleon as a function of the atomic number of the target material are shown in Fig. 6.21

6.8.1 Systematic Errors

The following sources of systematic errors are considered in the analysis:

$\triangle p_t^2$	C	Ti	W
		K_S^0	
0. - 0.2	327.1 ± 16.6 ± 55.6	1549.5 ± 79.3 ± 263.4	4042.8 ± 204.4 ± 687.2
0.2 - 0.4	121.2 ± 6.2 ± 20.6	580.7 ± 30.2 ± 98.7	1542.1 ± 78.6 ± 262.1
0.4 - 0.6	56. ± 2.9 ± 9.5	281.2 ± 15.2 ± 47.8	743.8 ± 38.5 ± 126.4
0.6 - 0.8	29.5 ± 1.6 ± 5.	146.5 ± 8.3 ± 24.9	415.1 ± 22. ± 70.5
0.8 - 1.0	18.2 ± 1.1 ± 3.1	93.3 ± 5.8 ± 15.8	253.3 ± 14. ± 43.01
1.0 - 1.2	11.1 ± 0.7 ± 1.8	67.7 ± 4.9 ± 11.5	169.7 ± 9.9 ± 28.8
		Λ	
0. - 0.2	81.2 ± 4.5 ± 13.7	494.9 ± 28.1 ± 84.1	919.7 ± 48.7 ± 156.3
0.2 - 0.4	50.6 ± 2.8 ± 8.6	296.7 ± 17.1 ± 50.4	577.9 ± 30.7 ± 98.2
0.4 - 0.6	32.7 ± 1.9 ± 5.5	179.1 ± 11.2 ± 30.4	430.8 ± 23.9 ± 73.2
0.6 - 0.8	20.7 ± 1.4 ± 3.5	114.7 ± 8.1 ± 19.5	269.1 ± 15.9 ± 45.7
0.8 - 1.0	14.8 ± 1.1 ± 2.5	90.1 ± 8. ± 15.3	221.7 ± 14.6 ± 37.7
1.0 - 1.2	12.3 ± 1.2 ± 2.1	77.1 ± 8.8 ± 13.1	142.6 ± 10.7 ± 24.2
		Λ	
0. - 0.2	25.1 ± 1.5 ± 4.2	118.2 ± 7.2 ± 20.1	317.2 ± 17.6 ± 53.9
0.2 - 0.4	16.1 ± 0.9 ± 2.7	79.6 ± 4.9 ± 13.5	200.2 ± 11.1 ± 34.
0.4 - 0.6	9.7 ± 0.6 ± 1.6	51.3 ± 3.5 ± 8.7	126.6 ± 7.4 ± 21.5
0.6 - 0.8	6.1 ± 0.4 ± 1.	27.5 ± 2.2 ± 4.6	87.6 ± 5.6 ± 14.8
0.8 - 1.0	3.5 ± 0.3 ± 0.5	19.9 ± 2.1 ± 3.3	56.7 ± 4.1 ± 9.6
1.0 - 1.2	2.6 ± 0.2 ± 0.4	19.1 ± 2.6 ± 3.2	36.8 ± 3.1 ± 6.2

Table 6.7: The inclusive differential production cross section $\mathrm{d}\sigma_{pA}/\mathrm{d}p_t^2$ in $mb/(GeV/c)^2$ for K_S^0, Λ and $\bar{\Lambda}$ particles measured on three different targets. The p_t^2 bins ($\triangle p_t^2$) are in $(GeV/c)^2$.

- In order to understand the errors in the efficiency estimation, the selection criteria were varied within their measured resolution. As well, a dependence of the V_0 reconstruction on the event multiplicity was investigated. These two effects are summed into the efficiency estimation systematic error σ_{eff} of 5%.

- The limited MC statistic contributes into systematic error σ_{stat} 2%.

- The bias which is coming from the not proper described data behavior in simulated events is estimated by re-weighting the MC p_t^2 and x_F distributions, this results into a 10% systematic error σ_{mc}

- For the background fitting of the invariant mass distributions different functions were used and also bin sizes in x_F and p_t^2 were varied. This results in a change of the cross section in the order of 3% σ_{fit} .

- The integrated luminosity was determined with 3 different methods, the obtained results differ within 5-10%. Conservatively an error of σ_{Lumi}=10% is included in the total systematic uncertainty.

K^0_S (Carbon)						
$\triangle x_F$						
-0.12 - -0.1	-	-	-	-	-	-
-0.1 - -0.08	-	-	-	-	27.3 ± 5.1	15.2 ± 2.5
-0.08 - -0.06	-	-	115. ± 22.1	55. ± 5.	37.5 ± 5.2	22.6 ± 2.8
-0.06 - -0.04	-	280. ± 22.5	152.1 ± 7.3	77.6 ± 5.1	45.6 ± 2.5	37.2 ± 2.8
-0.04 - -0.02	1162.1 ± 32.	452.5 ± 10.1	210.4 ± 5.	110. ± 5.	70. ± 5.	37.2 ± 2.8
-0.02 - 0.0	1787.1 ± 20.8	602.5 ± 10.3	255.3 ± 7.5	130. ± 5.	72.5 ± 5.1	47.1 ± 2.9
Λ (Carbon)						
x_F						
-0.12 - -0.1	110.1 ± 10.6	50.4 ± 2.6	32.8 ± 5.2	20.8 ± 2.6	10.4 ± 2.7	10.4 ± 2.5
-0.1 - -0.08	120.5 ± 7.8	75.3 ± 5.2	37.5 ± 2.6	17.5 ± 2.3	25.1 ± 5.2	12.5 ± 2.7
-0.08 - -0.06	120.8 ± 7.3	72.9 ± 5.4	42.7 ± 2.3	32.8 ± 5.2	20.1 ± 2.6	15.6 ± 2.1
-0.06 - -0.04	157.3 ± 7.9	80.2 ± 5.6	65.2 ± 5.2	35.1 ± 2.5	17.7 ± 2.1	20.8 ± 5.2
-0.04 - -0.02	195.7 ± 10.4	117.4 ± 4.2	70.8 ± 6.2	40.1 ± 3.	32.8 ± 5.3	23.4 ± 6.2
-0.02 - 0.0	282.5 ± 22.9	130.2 ± 5.4	80.3 ± 5.4	50.2 ± 5.3	37.6 ± 5.1	25.1 ± 5.1
$\bar{\Lambda}$ (Carbon)						
x_F						
-0.12 - -0.1	47.3 ± 6.1	28.7 ± 4.1	11.9 ± 2.6	6.5 ± 1.7	5.3 ± 1.4	5.4 ± 1.9
-0.1 - -0.08	55.6 ± 4.8	29. ± 3.1	12.3 ± 2.	10.9 ± 2.4	8.7 ± 2.4	5.8 ± 1.8
-0.08 - -0.06	87.7 ± 5.8	40.7 ± 3.5	24.4 ± 2.9	12.7 ± 1.9	7.4 ± 1.6	6.7 ± 1.7
-0.06 - -0.04	75.8 ± 5.2	50.5 ± 3.6	42.5 ± 4.	20.8 ± 2.6	23.4 ± 4.8	7.3 ± 1.8
-0.04 - -0.02	106.8 ± 7.5	66.4 ± 4.	31.9 ± 2.5	28.5 ± 3.2	15.6 ± 2.5	11.4 ± 2.4
-0.02 - 0.0	139.3 ± 15.6	76.1 ± 5.2	46.4 ± 3.6	26.8 ± 3.1	14.5 ± 2.5	7.8 ± 1.9
$\triangle p_t^2$	0. - 0.2	0.2 - 0.4	0.4 - 0.6	0.6 - 0.8	0.8 - 1.0	1.0 -1.2

Table 6.8: The differential production cross section $\mathrm{d}\sigma_{pA}/\mathrm{d}p_t^2\mathrm{d}x_F$ in $mb/(GeV/c)^2$ for K^0_S, Λ and $\bar{\Lambda}$ particles measured on carbon target. The p_t^2 bins ($\triangle p_t^2$) are in $(GeV/c)^2$.

K^0_S (Titan)						
$\triangle x_F$						
-0.12 - -0.1	-	-	-	-	-	-
-0.1 - -0.08	-	-	-	-	311.3 ± 116.1	101.3 ± 28.3
-0.08 - -0.06	-	-	341.8 ± 70.	323.7 ± 35.7	206.3 ± 27.1	155.1 ± 25.3
-0.06 - -0.04	-	1736.7 ± 157.4	708.6 ± 36.1	399.6 ± 24.5	248.3 ± 20.7	204.2 ± 24.2
-0.04 - -0.02	5536.5 ± 164.3	1970.6 ± 46.1	1074.2 ± 36.9	481.3 ± 22.8	340.9 ± 24.	256.8 ± 26.7
-0.02 - 0.0	8060.6 ± 96.1	3524.4 ± 67.3	1217.7 ± 37.	570.4 ± 25.1	369.3 ± 23.7	241.7 ± 22.5
Λ (Titan)						
x_F						
-0.12 - -0.1	462.6 ± 42.	221.8 ± 19.4	186.3 ± 27.1	77.3 ± 13.8	84.7 ± 21.5	-
-0.1 - -0.08	537.4 ± 32.8	354.1 ± 27.6	210.5 ± 23.6	179.6 ± 29.9	96.5 ± 22.3	59.8 ± 17.3
-0.08 - -0.06	605.7 ± 35.	418.4 ± 28.7	262.2 ± 25.3	174.4 ± 23.6	133.3 ± 26.	49.4 ± 10.1
-0.06 - -0.04	821. ± 43.7	416.6 ± 25.1	284.7 ± 24.4	254.2 ± 32.8	181.7 ± 33.6	67.2 ± 13.4
-0.04 - -0.02	948.5 ± 56.	483.7 ± 28.3	287.1 ± 22.6	204.9 ± 22.4	239.3 ± 39.9	129.8 ± 29.5
-0.02 - 0.0	1224.2 ± 111.6	610.9 ± 41.9	396.1 ± 33.1	235.3 ± 26.5	149. ± 25.6	109.1 ± 28.4
$\bar{\Lambda}$ (Titan)						
x_F						
-0.12 - -0.1	80.1 ± 10.5	147.9 ± 21.	40.5 ± 8.2	23.5 ± 6.3	-	-
-0.1 - -0.08	120.9 ± 11.4	147.8 ± 16.6	75.5 ± 12.	48.4 ± 9.7	33.2 ± 9.3	11.5 ± 4.1
-0.08 - -0.06	285.7 ± 22.2	131.2 ± 12.1	85.9 ± 11.	77.2 ± 13.5	50.4 ± 11.6	35.1 ± 10.8
-0.06 - -0.04	296.9 ± 20.4	221.5 ± 17.2	143.7 ± 14.8	84.5 ± 12.2	42.7 ± 7.6	56.1 ± 18.5
-0.04 - -0.02	512.1 ± 38.3	352.6 ± 25.9	233.5 ± 24.3	136.5 ± 18.1	102.9 ± 19.1	56.6 ± 13.1
-0.02 - 0.0	674.6 ± 84.1	320.1 ± 25.7	255.6 ± 25.6	141.4 ± 19.3	109.1 ± 22.1	59.1 ± 18.9
$\triangle p_t^2$	0. - 0.2	0.2 - 0.4	0.4 - 0.6	0.6 - 0.8	0.8 - 1.0	1.0 -1.2

Table 6.9: The differential production cross section $\mathrm{d}\sigma_{pA}/\mathrm{d}p_t^2\mathrm{d}x_F$ in $mb/(GeV/c)^2$ for K^0_S, Λ and $\bar{\Lambda}$ particles measured on titan target. The p_t^2 bins ($\triangle p_t^2$) are in $(GeV/c)^2$.

K^0_S (Tungsten)						
$\triangle x_F$						
-0.12 - -0.1	-	-	-	-	-	-
-0.1 - -0.08	-	-	-	-	329.9 ± 47.4	292.1 ± 43.2
-0.08 - -0.06	-	-	946.1 ± 157.4	685.2 ± 47.4	441.0 ± 32.6	365.1 ± 33.4
-0.06 - -0.04	-	3639.5 ± 200.1	1858.8 ± 62.2	1143.2 ± 46.2	659.9 ± 35.	477.7 ± 30.8
-0.04 - -0.02	13966.4 ± 292.9	5362.3 ± 86.2	2616.8 ± 58.5	1357.1 ± 42.3	895.3 ± 38.1	582.2 ± 34.1
-0.02 - 0.0	19801.5 ± 161.1	6978.4 ± 91.8	3158.2 ± 63.3	1747.6 ± 50.5	1008.3 ± 41.1	632.9 ± 35.3
Λ (Tungsten)						
x_F						
-0.12 - -0.1	1191.1 ± 73.4	629.7 ± 37.8	424.6 ± 35.1	316.7 ± 37.3	185.5 ± 29.1	126.3 ± 25.1
-0.1 - -0.08	1216.5 ± 50.3	784.7 ± 38.3	568. ± 40.1	411.7 ± 39.	353.9 ± 47.2	306.6 ± 61.6
-0.08 - -0.06	1623.1 ± 58.7	878.4 ± 38.2	622.9 ± 37.3	433.1 ± 33.3	439.4 ± 48.6	259.3 ± 38.
-0.06 - -0.04	1829.8 ± 64.5	1009.1 ± 39.2	842.6 ± 45.8	450.2 ± 31.5	457.2 ± 44.7	251.6 ± 31.1
-0.04 - -0.02	2759.3 ± 110.1	1376.5 ± 50.2	811.4 ± 39.8	559. ± 36.8	493.5 ± 47.2	342.1 ± 42.2
-0.02 - 0.0	3261.2 ± 204.9	1713.6 ± 76.8	1069.5 ± 57.2	613. ± 43.3	472.5 ± 49.	342.4 ± 54.4
$\bar{\Lambda}$ (Tungsten)						
x_F						
-0.12 - -0.1	237.7 ± 27.4	236. ± 24.	177.9 ± 23.1	122.6 ± 22.7	63.8 ± 14.5	58. ± 13.6
-0.1 - -0.08	260.8 ± 20.6	428.6 ± 34.3	293.5 ± 29.5	151.7 ± 21.1	109.1 ± 19.5	67.3 ± 15.7
-0.08 - -0.06	888. ± 45.9	468.8 ± 28.2	280.6 ± 24.	183.1 ± 20.7	137.2 ± 19.3	114.6 ± 22.5
-0.06 - -0.04	978.8 ± 46.2	567.3 ± 29.9	345.7 ± 22.5	329.8 ± 32.2	189.1 ± 23.7	134. ± 22.
-0.04 - -0.02	1369.8 ± 71.7	818.5 ± 37.6	474.1 ± 28.7	347.7 ± 27.8	277.3 ± 30.8	138.8 ± 18.2
-0.02 - 0.0	1385.8 ± 124.2	939.8 ± 50.9	543.8 ± 35.1	370.2 ± 30.1	247.3 ± 29.9	247.6 ± 47.6
$\triangle p_t^2$	0. - 0.2	0.2 - 0.4	0.4 - 0.6	0.6 - 0.8	0.8 - 1.0	1.0 -1.2

Table 6.10: The differential production cross section $\mathrm{d}\sigma_{pA}/\mathrm{d}p_t^2\mathrm{d}x_F$ in $mb/(GeV/c)^2$ for K^0_S, Λ and $\bar{\Lambda}$ particles measured on tungsten target. The p_t^2 bins ($\triangle p_t^2$) are in $(GeV/c)^2$.

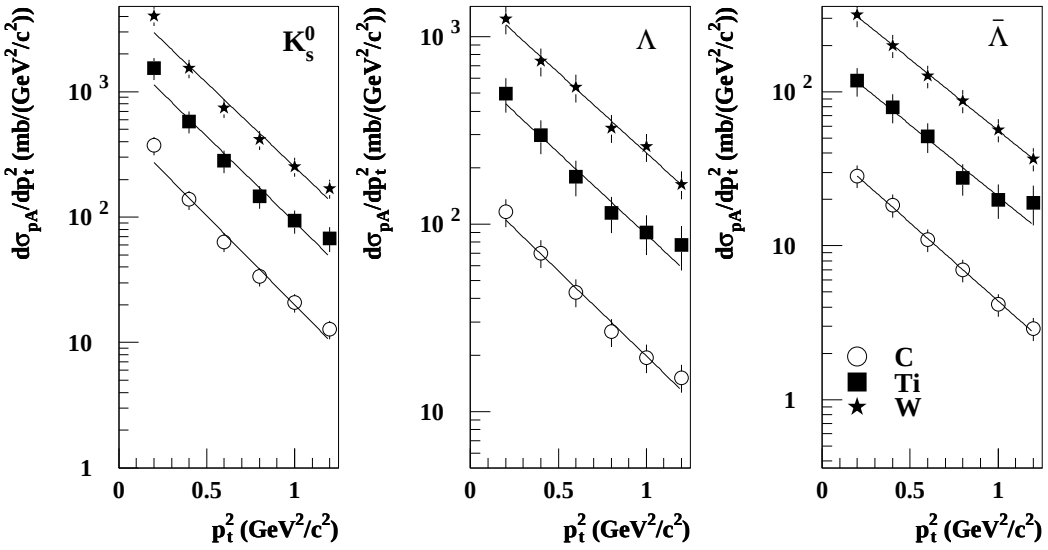

Figure 6.18: The differential production cross sections $\mathrm{d}\sigma_{pA}/\mathrm{d}p_t^2$ for V_0 for three target materials (Carbon, Titanium and Tungsten).

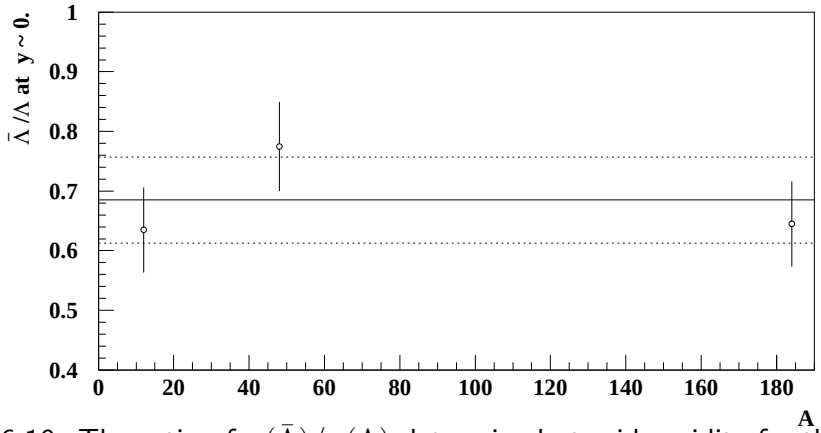

Figure 6.19: The ratio of $\sigma(\bar{\Lambda})/\sigma(\Lambda)$ determined at mid-rapidity for the used targets.

- In order to extract $\mathrm{d}\sigma/\mathrm{d}p_t^2$ the differential cross section is extrapolated to the full x_F range with the equation

$$\frac{\mathrm{d}^2\sigma}{\mathrm{d}p_t^2\mathrm{d}x_F} = C\,(1-|x_F|)^n\,exp(-B\,p_t^2) \tag{6.21}$$

  where the parameter n is determined experimentally [61]. By varying the parameter n the induced systematic error of the extrapolation σ_{extrap} is estimated to be in the

	K^0_S	Λ	$\bar{\Lambda}$
σ_{pN} (mb)	$13.2 \pm 0.91 \pm 2.3$	$6.5 \pm 0.57 \pm 0.94$	$1.6 \pm 0.17 \pm 0.28$
α	0.961 ± 0.026	0.927 ± 0.021	0.93378 ± 0.026

Table 6.11: Production cross section per nucleon for V_0 and results of the dependences of production cross sections on the atomic number.

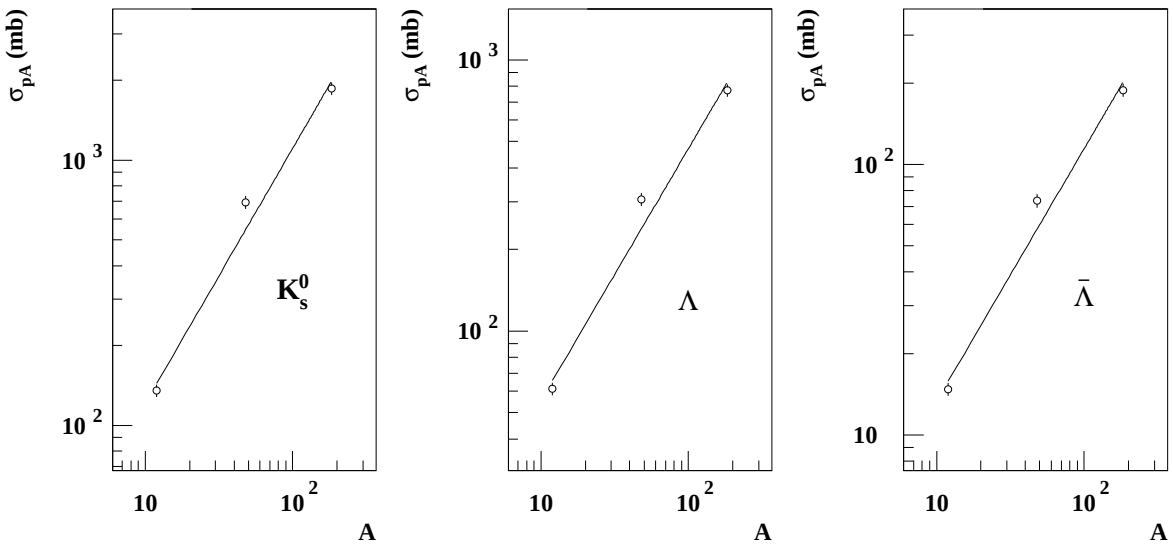

Figure 6.20: The V_0 total production cross section as a function of atomic mass A of the target material. The solid lines show fits by the $\sigma_{pA} \propto A_\alpha$ function.

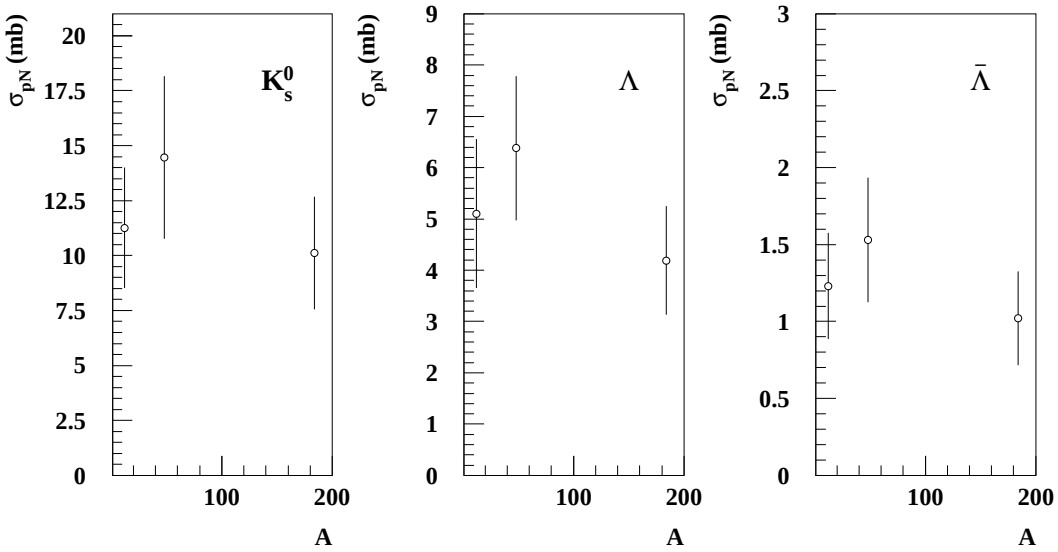

Figure 6.21: The V_0 total production cross section per nucleon as a function of atomic mass A of the target material.

order of 15% for K^0_S, Λ and $\bar{\Lambda}$.

To obtain the total systematic error, the errors are combined in the following way

$$\sigma^{sys}_{tot} = \sqrt{\sigma^2_{eff} + \sigma^2_{stat} + \sigma^2_{mc} + \sigma^2_{fit} + \sigma^2_{Lumi} + \sigma^2_{extrap}} \tag{6.22}$$

The presented analysis is clearly dominated by systematic errors. A systematic error due to the deviations in the p_t^2 and x_F can be reduced by improving the kinematical model used for V_0 generation, for example by introducing two slopes into the p_t^2 distribution, as was mentioned above. A further improvement of the detector description in simulated events is needed. All sources of the systematic errors are listed in the Table 6.12.

Source of systematic error	error, %
Selection criteria	5.
Limited MC statistic	2.
Not proper described behaviour of p_t^2 and x_F	10.
Bin size and fit function	3.
Luminosity determination	10.
Extrapolation to the full x_F range	15.

Table 6.12: Sources of the systematic errors contributed to the final systematic error.

6.9 Summary

The results of the inclusive production cross section of V_0 strange particle measurements using the HERA-B detector were presented. The V_0 cross sections were determined using the information from the tracking stations of VDS and Main tracker for three types of target material, carbon , titanium and tungsten, in the squared transverse momentum range of $0. < p_t^2 < 1.5$ $(\mathrm{GeV/c})^2$ and in the Feynman scaling variable (x_F) range $-0.12 < x_F < 0.$.

The cross section analysis consist of the following main steps:

- A detailed quality check was performed for the ITR data for all runs considered in the analysis.
- The geometrical acceptance and reconstruction efficiency were estimated by using Monte Carlo simulation. The overall efficiency to reconstruct the V_0 was found to be about 10% for K_S^0 and 5% for $\Lambda(\bar{\Lambda})$.
- The backgrounds to the V_0 mass peaks were subtracted by a polynomial fit of the background spectrum.

Various sources of systematic uncertainties, such as luminosity determination, V_0 background subtraction and MC description of data especially p_t^2 and x_F kinematical variables were estimated.

The V_0 cross sections per nucleon were fitted for the three target materials using a functional dependence $\sigma \propto A^{\alpha}$. The exponent α was measured to be 0.932 ± 0.081. The value for the K_S^0 inclusive production cross section provided by the Annecy(LAPP) [64] experiment for $\sqrt{s} = 52.5$ GeV is in agreement with the measurements presented in this work. The cross section for Λ is in agreement with the numbers provided by ISR at $\sqrt{s} = 53$ GeV and $\sqrt{s} = 62$ GeV [65]. Comparisons of the V_0 inclusive production cross section and the ratio of production cross sections $\sigma(\bar{\Lambda})/\sigma(\Lambda)$ determined at mid-rapidity, with other experiments is shown in Fig.6.22 and in Fig.6.23

The presented analysis illustrates a good understanding of the HERA-B detector performance during data taking 2002/2003. It also demonstrates that results of HERA-B can significantly contribute to the V_0 inclusive cross section measurements and help to better understand the strange particle production mechanism.

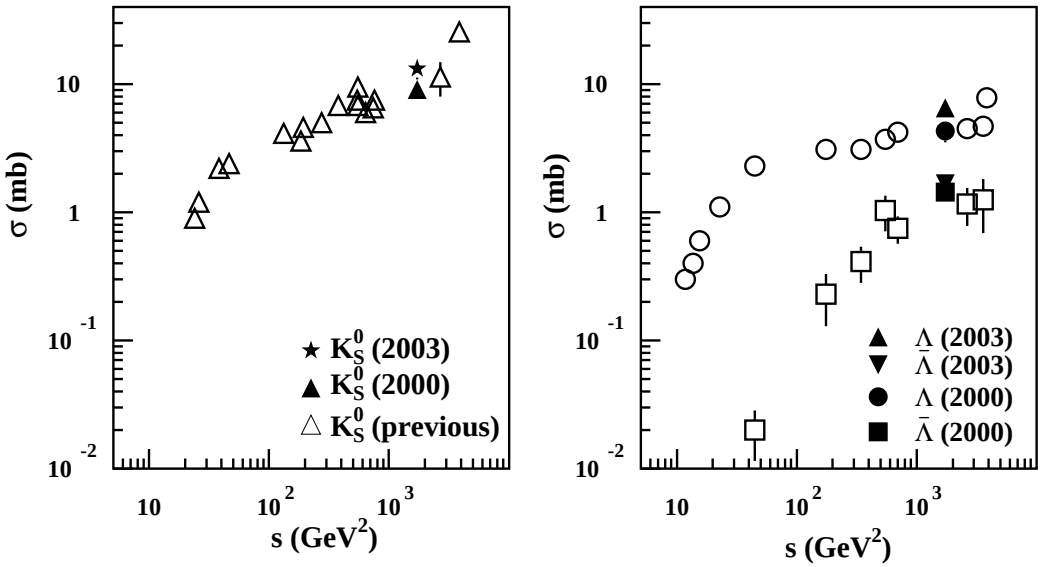

Figure 6.22: Production cross section of V_0 as a function of s (the square of center of mass energy). Measurements obtained with the 2000 and 2002 Minimum bias data are shown with black symbols, open symbols represent measurements done by another experiments.

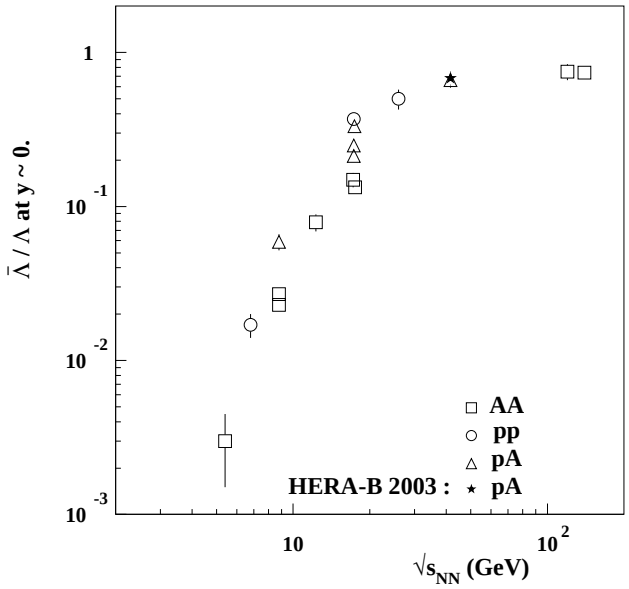

Figure 6.23: Ratio of production cross sections $\sigma(\bar{\Lambda})/\sigma(\Lambda)$ determined at mid-rapidity as a function of $\sqrt{s}$. Measurements obtained with the 2002 Minimum bias data are shown with black symbol, open symbols represent measurements done by another experiments.

Chapter 7

Conclusion

The HERA-B experiment located at the HERA collider at DESY, was designed and built to measure CP violation in the system of neutral B mesons. HERA-B has the typical setup of a forward magnet spectrometer with a fixed multi-wire target. The experiment is designed to cope with large particle fluxes up to $10^7 s^{-1} cm^{-2}$.

Based on the data taken in the running period 2000 it was concluded that the performance of the default pattern recognition package RANGER is not at the sufficient level, especially for the Inner Tracker system. This motivated the development of an alternative track reconstruction package OTR/ITR-CATS for the Pattern Tracker of the HERA-B experiment. This package employs a combined approach for track reconstruction based on the use of a cellular automaton for track searching and the Kalman filter technique for track fitting. Comprehensive tests of the package have shown high reconstruction efficiency, good accuracy of track parameter estimates, a reasonable behavior of CPU time consumption. Based on the demonstrated performance CATS has been chosen as the new default pattern recognition package. The algorithm was successfully used during online data taking and offline reprocessing of the collected data in the years 2002 and 2003.

During the running period 2002/03 the performance of the Inner Tracking system was estimated. A method was developed to measure the hit efficiency for the Inner Tracker system. The applied procedure was based on the developed pattern recognition algorithm. During running in 2002-2003 several chambers of the Inner Tracker system demonstrated rather low efficiency, due to a low resistance between neighboring strips on the Kapton FanIn. For chambers which were not affected by the above mentioned problem, the efficiency varies between 90% and 95%. Affected chambers showed efficiencies between 50% and 90%.

In the second part of this thesis, the results of a measurement of the inclusive production cross section of K^0_S, Λ and $\bar{\Lambda}$ particles using the HERA-B detector were presented. The geometrical acceptance and reconstruction efficiency were estimated by using Monte Carlo simulation. The overall efficiency to reconstruct the V_0 was found to be about 10% for K^0_S and 5% for $\Lambda(\bar{\Lambda})$. Various sources of systematic uncertainties, such as luminosity determination, MC description of data especially p_t^2 and x_F kinematical variables were estimated. The V_0 cross sections were measured for three types of target material, carbon , titanium and tungsten. Dependence of the total cross section σ_{pA} on the target atomic mass is measured. Obtained inclusive production cross sections were compared with results of other experiments.

The obtained measurements in the negative x_F region will provide important input to the theories which are needed for the study of fragmentation processes.

List of Tables

List of Figures

Appendix A

Runs used in the analysis

Run	Wire	Trigger type	N(events)	luminosity, mb^{-1}
20668	below I	RE	2.288.926	9715.
20677	below I	RE	4.568.646	20392.
20678	below I	RE	5.121.506	22795.
20768	below I	RE	2.435.408	10697.
20682	below II	RE	5.497.551	8884.
20695	below II	RE	4.724.521	7562.
20747	inner I	RE	6.219.769	3751.
20749	inner I	RE	3.898.581	2342.
20474	inner II	R	4.034.174	18572.
20478	inner II	R	8.209.809	37887.
20507	inner II	R	5.270.486	23407.

Table A.1: Integrated luminosity of runs used in the analysis.

Bibliography

[1] The HERA-B Collaboration, HERA-B An Experiment To Study CP Violation in the B System Using an Internal Target at the HERA Proton Ring, Proposal, DESY-PRC 94/02, May 1994.

[2] K. Ehret, Nucl. Instr. Methods **A446** (2000) 190.

[3] C. Bauer *et al.*, Nucl. Instr. Methods **A453** (2000) 103.

[4] M. Hohlmann, *The Outer Tracker of HERA-B*, Nucl. Instr. Meth. A461 (2001) 21–24.

[5] I. Arino et al., *The HERA-B ring imaging Cerenkov counter*, hep-ex/0303012.

[6] G. Avoni et al., *The electromagnetic calorimeter of the HERA-B experiment*, Nucl. Instr. Meth. A461 (2001) 332–336.

[7] V. Eiges et al., *The muon detector at the HERA-B experiment*, Nucl. Instr. Meth. A461 (2001) 104–106.

[8] V. Balagura et al., *The first-level trigger of the HERA-B experiment: Performance and expectation*, Nucl. Instr. Meth. A494 (2002) 526–534.

[9] A. Oed, *Position Sensitive Detectors with Microstrip Anode for Elec tron Multiplication with Gases*, NIM A 263, 351-359,1988.

[10] Bernhard Schmidt, *Micro Strip Gas Chambers: Recent Developments, Radiation Damage and Longterm Behavior*, NIM A 419, 230-238, 1998.

[11] F. Sauli, Nuclear Instruments and Methods A386, 531, 1997.

[12] Fraunhofer Institut für Schicht und Oberflächentechnik IST, D 3 8108 Braunschweig.

[13] *AF45 from DESAG*, http://www.schott.com/displayglass/english/products/af45.

[14] Bagaturia et. al (HERA-B ITR collaboration), *Studies of Aging and HV Break down Problems during Development of MSGC and GEM Detectors for the Inner Tracking System of HERA-B*, submitted to Nuclear Instuments and Methods, Feb. 2002.

[15] Online Calibration and Alignment, http://www-hera-b.desy.de/subgroup/daq/cna.

[16] HERA-B ITR group, *Signal loss in the Inner Tracker system*, HERA-B Internal Note (2003).

[17] M. Villa, *The ECAL reconstruction package for the online enviroment*, http://www-hera-b.desy.de/subgroup/detector/ecal/care/care-online.html

[18] The HERA-B collaboration, *HERA-B physics in 2001/2002*, HERA-B Internal Note (2000).

[19] The HERA-B collaboration, *Update of status and plans*, HERA-B Internal Note 01-064 (2001).

[20] see, e.g., *Proc. 15th Int. Conf. on Ultra-Relativistic Nucleus-Nucleus Collisions* (QM2001), Nucl. Phys. A698 (2002) Issue 1-4.

[21] A. Lamont, *Neutral Strange Particle Production in Ultra-Relativistic Heavy Ion Collissions at* $\sqrt{S_{NN}} = 130GeV$, PhD thesis, The University of Birmingham, 2002.

[22] O. Igonkina, *A manual on MARPLE package for HERA-B reconstruction package*, HERA-B Internal Note 98-129 (1998).

[23] D. Emelyanov et al., *Primary Vertex Reconstruction by ROVER*, HERA-B Internal Note 00-139 (2000).

[24] I. Abt, D. Emeliyanov, I. Kisel and S. Masciocchi, *CATS: a Cellular Automaton for Tracking in Silicon for the HERA-B Vertex Detector*, submitted to Nucl. Instr. Meth. Section A.

[25] R. Mankel, *A Concurrent Track Evolution Algorithm for Pattern Recognition in the HERA-B Main Tracking System*, Nucl. Instr. Meth. A395 (1997) 169–184.

[26] M. Starič, private communication.

[27] T. Lohse et al. (HERA-B Collaboration), *An Experiment to Study CP Violation in the B System Using an Internal Target at the HERA Proton Ring*, HERA-B Proposal, DESY-PRC 94/02 (1994) 1–289.

[28] E. Hartouni et al. (HERA-B Collaboration), *HERA-B Technical Design Report*, DESY-PRC 95/01, 1995.

[29] The BaBar Collaboration, *The BaBar Detector*, Submitted to Nucl. Instrum. Meth. hep-ex/0105044, Apr 2001.

[30] The Belle Collaboration, *Technical Design Report*, KEK-Report 94-2, April 1995.

[31] Lincoln Wolfenstein, *Parametrization of the Kobayashi-Moskawa Matrix*, Phys. Rev. Lett. 51 (1983), 1945.

[32] T. Lohse, *HERA-B: Overview and Engineering Runs*, Nucl. Instr. Meth. A408 (1998) 154–164.

[33] U. Uwer, *Status and Commissioning Results from HERA-B*, Nucl. Instr. Meth. A462 (2001) 202–211.

[34] M. Medinnis, *HERA-B Status*, Nucl. Instr. Meth. A473 (2001) 174–177.

[35] A. Zoccoli, *Status of the HERA-B Experiment*, Nucl. Phys. B (Proc. Suppl.) 99B (2001) 267–275.

[36] W. Gradl, *The Inner Tracker of HERA-B*, Nucl. Instr. Meth. A461 (2001) 80–81.

[37] T. Schober, *Untersuchung der Hough-Transformation als Beispiel eines globalen Algorithmus zur Mustererkennung im HERA-B Spurkammersystem*, Diploma Thesis, Humboldt-Universität zu Berlin, 1996.

[38] C. Borgmeier, *Globale Mustererkennung in den HERA-B Spurkammern*, Diploma Thesis, Humboldt-Universität zu Berlin, 1997.

[39] A. Paus, *Mustererkennung im Spurkammer-System des HERA-B-Detektors mit einem Elastic-Arms-Algorithmus*, Diploma Thesis, Humboldt-Universität zu Berlin, 1997.

[40] R. Durbin and D. Willshaw, *An Analogue Approach to the Travelling Salesman Problem Using an Elastic Net Method*, Nature 326 (1987) 689.

[41] C. Peterson and T. Rognvaldsson, *Introduction to Artificial Neural Networks*, 1991 CERN School of Computing, Ystad, Sweden, 23 August – 2 September 1991, CERN 92-02, 1992, p. 113.

[42] I. Kisel and V. Kovalenko, *Elastic Net for Broken Multiple Scattered Tracks*, Comp. Phys. Commun., 98 (1996) 45.

[43] I. Kisel, V. Kovalenko, F. Laplanche et al. (NEMO Collaboration), *Cellular Automaton and Elastic Net for Event Reconstruction in the NEMO-2 Experiment*, Nucl. Instr. and Meth. A387 (1997) 433.

[44] R.K. Bock et al., *Data Analysis Techniques for High-Energy Physics Experiments,* Cambridge Univ. Press (1990).

[45] K. Brammer and G. Siffling, *Kalman-Bucy Filter*, Oldenburg (1974).

[46] R. Mankel, *Recomendation for Evaluating the Performance of the HERA-B Reconstruction Modules.*, Hera-B 99-063, Software 99-007.

[47] M.-A. Pleier, *Cloneremove v1.0*, Hera-B Internal Note 01-062, (2001).

[48] H.Pi, *An event generator for interactions between hadrons and nuclei - FRITIOF version 7.0*, Comput. Phys. Commun. 71, 173-192 (1992).

[49] *GEANT 3.21 Detector Description and Simulation Tool*, CERN
Program Library Long Writeup W5103, CERN, Geneva (1994), available at:
http://wwwinfo.cern.ch/asdoc/Welcome.html (status: June 2003).

[50] J. Ivarsson et al., *PYTHIA and FRITIOF: Event Generators for HERA-B*, HERA-B Internal Note 99-067 (1999).

[51] T. Sjöstrand, *PYTHIA 5.7 and JETSET 7.4 -Physics and Manual*, Computer Physics Commun. 82, 74 (1994), hep-ph/9508391.

[52] S. Nowak, *A Description of HERA-B GEANT*, HERA-B Internal Note 94-123 (1994); new on-line version can be found on http://www-hera-b.desy.de/subgroup/software/arte/gean/hbgean.html.

[53] The HERA-B software group, *ARTE - HERA-B's Analysis and Reconstruction Tool*, http://www-hera-b.desy.de/subgroup/software

[54] M. Agari, *Search for the decay of charmed mesons with the HERA-B detector in proton nucleon collisions at* $\sqrt{s}$*=42 GeV*, Diploma thesis, Universität Heidelberg, October 2001.

[55] M.-A. Pleier, *Measurement of inclusive* $\Lambda/\bar{\Lambda}$ *hyperon polarisation in proton nucleus collisions at 920 Gev proton beam energy*, Ph.D. Thesis, Universität Heidelberg, 2002.

[56] The HERA-B collaboration, *Luminosity measurement in HERA-B*, publication in preparation (2003).

[57] A. Somov, *Hard proton nucleus interactions production of heavy flavours at HERA-B*, Ph.D. Thesis, Humboldt-Universität zu Berlin, 2000.

[58] A. Somov, Private Communication, 2003.

[59] J. Bastos,*A statistical method for monitoring the luminosity of HERA-B data*, http://www-hera-b.desy.de/subgroup/physics/herab/luminosity.

[60] *Particle Data Group*, The European Physical Journal, C15 (2000)

[61] M. Adamovich et al.,*Eur. J. Phys.*, in print, http://dx.doi.org/10.1140/epjc/s2002-01073-6.

[62] S. Brodsky et al., Phys. Rev. D17 (1978) 848.

[63] I. Abt et al., *Inclusive* V_0 *Production Cross Sections from 920 GeV Fixed Target Proton-Nucleus Collisions*, hep-ex/0212040.

[64] D. Drijard et al.,*Production of vector and tensor mesons in proton proton collisions at* $s = \sqrt{52.5}$ *GeV*, Zeit. Phys. C9:293, 1981.

[65] S. Erhan et al., Phys. Lett., 85B (1979) 447.

Acknowledgments

I am very thankful to my supervisor Prof. Günter Zech for the opportunity to work with the Inner Tracker group at HERA-B and for the productive discussions, his advice and for all the help he gave me during my stay in the University of Siegen. I would like to thank Prof. Peter Buchholz for his willingness to take the duties of the second referee.

I am also thankful to Dr. Torsten Zeuner for his enormous help during my stay in Hamburg and Siegen.

I wish to thank Dr. Dmitriy Emelianov for his support and readiness to help and Dr. Ivan Kisel who was always very cooperative.

Special thanks to all present and former colleagues from the Inner Tracker group which worked with me during this time. Special thanks to Ulrich Husemann for his help with Monte Carlo production and Dr. Mikhail Zavertiaev for the fruitful discussions.

Many thanks to all who helped me to go through with this manuscript: Torsten, Carsten and Hartmut, especially to find all missing articles.

I would like to thank my parents and relatives, they always give me the needed support.

I am gratefull to all my colleges from HERA-B experiment for their help in various aspects of work and life at Hamburg.

Hiermit erkläre ich, daß ich diese Arbeit selbständig verfaßt und alle Daten und Ergebnisse anderer Autoren als solche kenntlich gemacht habe.

Siegen, den 26.10.2003 (Iouri Gorbounov)